UNIVERSITY OF CALIFORNIA SAN DIEGO

Materials for High-Energy Laser Gain Media and Studying Laser Material Interactions

A Dissertation submitted in partial satisfaction of the requirements
for the degree Doctor of Philosophy

in

Materials Science and Engineering

by

Ross Elliott Turner

Committee in charge:

Professor Javier E. Garay, Chair
Professor Prabhakar R. Bandaru
Professor Farhat N. Beg
Professor Vlado A. Lubarda
Professor Lisa V. Poulikakos

2023

The Dissertation of Ross Elliott Turner is approved, and it is acceptable in quality and form for publication on microfilm and electronically.

University of California San Diego

2023

DEDICATION

There are two people I would like to dedicate this dissertation to, one academic, and one personal.

I dedicate this dissertation and the work shared to my father David Turner. I would not be there today if it were not for him raising me through a challenging path, and I cannot express how much I did this for him and our extended family. I went on this journey for so much more than myself, and I am grateful for the commitment to service that my father instilled in me at a young age. I hope that my contributions to the UCSD community are long-lived, and I thank my farther for showing me how what it means to give back to others.

I dedicate this dissertation to the late Professor Joanna McKittrick. Professor McKittrick provided me an opportunity to conduct research during my undergraduate studies at UCSD which sparked my intellectual curiosity with respect to research, and led me on the path to my MS at UCLA. After working professionally for a period of time, I found myself wanting to dig deeper and discover more about materials sciences, and I thank Professor McKittrick for instilling that curiosity into me. I know we did not spend as much time together upon my return to UCSD as I would have liked, but I appreciate every interaction I have ever had with you, and I know I would not be where I am today if it were not for you opening your doors to a naive student eager to learn and contribute to the field. Thank you.

TABLE OF CONTENTS

LIST OF FIGURES

LIST OF TABLES

LIST OF ABBREVIATIONS

CAPAD	Current Activated Pressure Assisted Densification
HEBM	High-Energy Ball Mill
HEL	High-Energy Laser
LEBM	Low-Energy Ball Mill
LMI	Laser Material Interaction
LLNL	Lawrence Livermore National Laboratory
LuAG	Lutetium Aluminum Garnet
OSL	Optical Sciences Laser
RE	Rare-Earth
RGD	Rayleigh-Gans-Debeye
SEM	Scanning Electron Microscope
UHP	Ultra-High Purity
XRD	X-Ray Diffraction
YAG	Yttrium Aluminum Garnet

ACKNOWLEDGEMENTS

There are many people I would like to acknowledge for their support and patience throughout this PhD journey.

I would like to thank my advisor, Professor Javier E. Garay for providing this opportunity for me to jump into research and think about technical and scientific problems in ways that I had previously not been afforded the time or the guidance to do so.

I would like to thank Dr. Yasuhiro Kodera for his hands on teaching, and his willingness to share his decades of processing lessons with the lab. So many of the little talks, and small suggestions became large impacts on my success over these last few years.

I would like to thank my other committee members Professor Farhat N. Beg, Professor Lisa V. Poulikakos, Professor Prabhakar R. Bandaru, and Professor Vlado A. Lubarda for their guidance and support of my dissertation research. Their input during my senate exam was invaluable, and allowed me to achieve more than I expected.

I would like to thank Dr. Harry B. Radousky, Dr. Michael R. Armstrong, Sophie E. Parsons, and Alison K. Ackerman for opening their doors and providing me an opportunity to study materials science at Lawrence Livermore National Laboratory.

Thank you to the old guard, the lab members that were there when I joined, and are now doing bigger and better things. I would not have achieved so much without the support of Dr. Xingzhong Wu and Dr. Darren M. Dewitt. The lessons learned, and the attention to detail that was shared early and often I really appreciated. I never took your time for granted and am so thankful for all of your support.

Thank you to the new guard, the lab members that joined since I returned to UCSD. You are doing great work, and have so many new research opportunities than the lab had

when I joined. You have a bright future ahead, and the lab will continue to be successful as long as you just keep doing what you are doing.

Thank you to my oldest group of friends, Evan, Christopher, and Kyle. Friends for 25 years, and still going strong. This PhD journey would not have been possible without the discussions, game nights, and catch up events over the last few years. Evan, I finished the PhD first, and I will never let you forget it.

Thank you to my siblings David and Natalie. With the world shutting down, and life changes having us more apart than ever, I know we were not able to spend as much time together in San Diego as we had hoped. I look forward to being able to travel again soon, and visiting the families you both are building.

Thank you to my father David. I would not be here if it were not for you instilling such a strong drive and work ethic into me from a young age. I know my path is not the one we initially thought I would be on, but I am excited to share this achievement with you.

Thank you to my partner Kimi. You have dealt with so much in this transition of both of our careers, and I do not take that for granted. There is no way I would have completed this journey without you, and I am excited to see our careers grow together now that it is complete.

To the entire Turner Family, I do not take lightly what the first PhD in the family means, and I will always find ways to support the extended family and guide those that wish to pursue a graduate education.

Funding of this work by the Office of Naval Research (ONR) and the Directed Energy Joint Technology Office (DE-JTO) is most gratefully acknowledged.

Funding of this work by the Defense Threat Reduction Agency (DTRA) and support from the Materials Science in Extreme Environments (MSEE) administered by Johns Hopkins University is most gratefully acknowledged.

Funding of this work by the School of Global Policy and Strategy (GPS) at UC San Diego as part of the Science Policy Fellowship is most gratefully acknowledged.

The project or effort depicted was or is sponsored by the Department of the Defense, Defense Threat Reduction Agency under award HDTRA1-20-2-0001. The content of the information does not necessarily reflect the position or the policy of the federal government, and no official endorsement should be inferred.

This work was performed in part at the San Diego Nanotechnology Infrastructure (SDNI) of UCSD, a member of the National Nanotechnology Coordinated Infrastructure (NNCI), which is supported by the National Science Foundation (Grant EECS-2025752).

Chapter 2, in part is currently being prepared for submission for publication of the material. Xingzhong Wu, Yasuhiro Kodera, and Javier E. Garay are co-authors for this work. The dissertation author was the primary researcher and author of this material.

Chapter 3, in part is currently being prepared for submission for publication of the material. Sophie E. Parsons, Alison K. Ackerman, Michael R. Armstrong, Harry B. Radousky, Farhat N. Beg, and Javier E. Garay are co-authors for this work. The dissertation author was the primary researcher and author of this material.

Chapter 4, in part is currently being prepared for submission for publication of the material. Gabriel R. Castillo, Colin G. Meisner, and Javier E. Garay are co-authors for this work. The dissertation author was the primary researcher and author of this material.

VITA

2012 Bachelor of Science in Aerospace Engineering, University of California San Diego

2013 Master of Science in Aerospace Engineering, University of California Los Angeles

2023 Doctor of Philosophy in Materials Science and Engineering, University of California San Diego

ABSTRACT OF THE DISSERTATION

Materials for High-Energy Laser Gain Media and Studying Laser Material Interactions

by

Ross Elliott Turner

Doctor of Philosophy in Materials Science and Engineering

University of California San Diego, 2023

Professor Javier E. Garay, Chair

Lasers are fundamental to our society and are used in an ever-increasing range of fields including manufacturing, communications, defense and medical industries. One of the main drivers in laser development is increasing laser power. This work presents the development of a new polycrystalline transparent ceramic material that shows promise as a high-power laser gain media. In addition, the development of materials specifically designed for fundamental laser-material interaction studies on lab scale as well as high energy, facility scale lasers is presented.

The power deliverable by a laser scales directly with the thermal conductivity of the laser gain material. Aluminum oxide (hexagonal, Al_2O_3) has a higher thermal conductivity

than any rare-earth host media available today thus synthesis/processing methods for obtaining high quality rare-earth doped alumina ceramics are of high interest. This work explores the impact of powder processing and densification conditions on the optical properties of ytterbium doped Al_2O_3 ceramics. Dopant incorporation methods and processing temperatures are explored to find the highest density ceramics possible. The first reported transparent ytterbium doped nanocrystalline alumina is characterized and discussed. The absorption and emission cross sections as well as upper state lifetime show promise for Yb:Al_2O_3 as a laser gain material.

This work also presents target fabrication methods for high intensity laser-material interaction studies. The target materials are metals (aluminum) and semiconductors (silicon). The targets have been used in collaborative campaigns at lab and facility scale lasers at intensities up to 10^{14} W/cm^2. In addition a study of silicon material damage as a function of intensity is presented. These experiments show that laser irradiation primarily results in melting at intensities up to 10^{13} W/cm^2.

CHAPTER 1. MOTIVATIONS AND INTRODUCTION TO TOPICS

1.1. Motivation

Ever since the development of the first working ruby laser by Maiman [1], the world has been chasing higher powered lasers for various applications. Lasers in their relatively short technological life have become a staple in our society, and the developments in laser technologies are vast and far reaching. There is not an industry that does not use lasers in some way, ranging from communication, to medical, to industrial, and scientific.

The fundamental limitation to scaling laser power, or laser energy, is the thermal conductivity of the laser host material. Laser power scales directly with the thermal conductivity of the material and development of new materials with higher thermal conductivities has been a topic of study for many years. For solid state lasers, the host material is the structural component the laser gain media, while the transition metal or rare-earth dopant is what is excited and produces the coherent beam of photons or laser.

Figure 1.1 is a plot of the thermal conductivity of laser host materials as a function of the Young's Modulus, or stiffness of the materials [2]. This figure highlights many materials that will be discussed in this work, including fused silica (or glass), sesquioxides, CaF_2, Yttrium Aluminum Garnet (YAG), and Al_2O_3 (Alumina, synthetic sapphire). Note that most of these materials have a cubic crystal structure, meaning that the index of refraction is the same in all orientations. For Alumina, because it has a hexagonal cubic structure, it has different indices of refraction based on orientation, and experiences birefringence as a result. YAG is the most ubiquitous laser host material, when doped with Neodymium (Nd), and can be found in many lasers that we use on a daily basis.

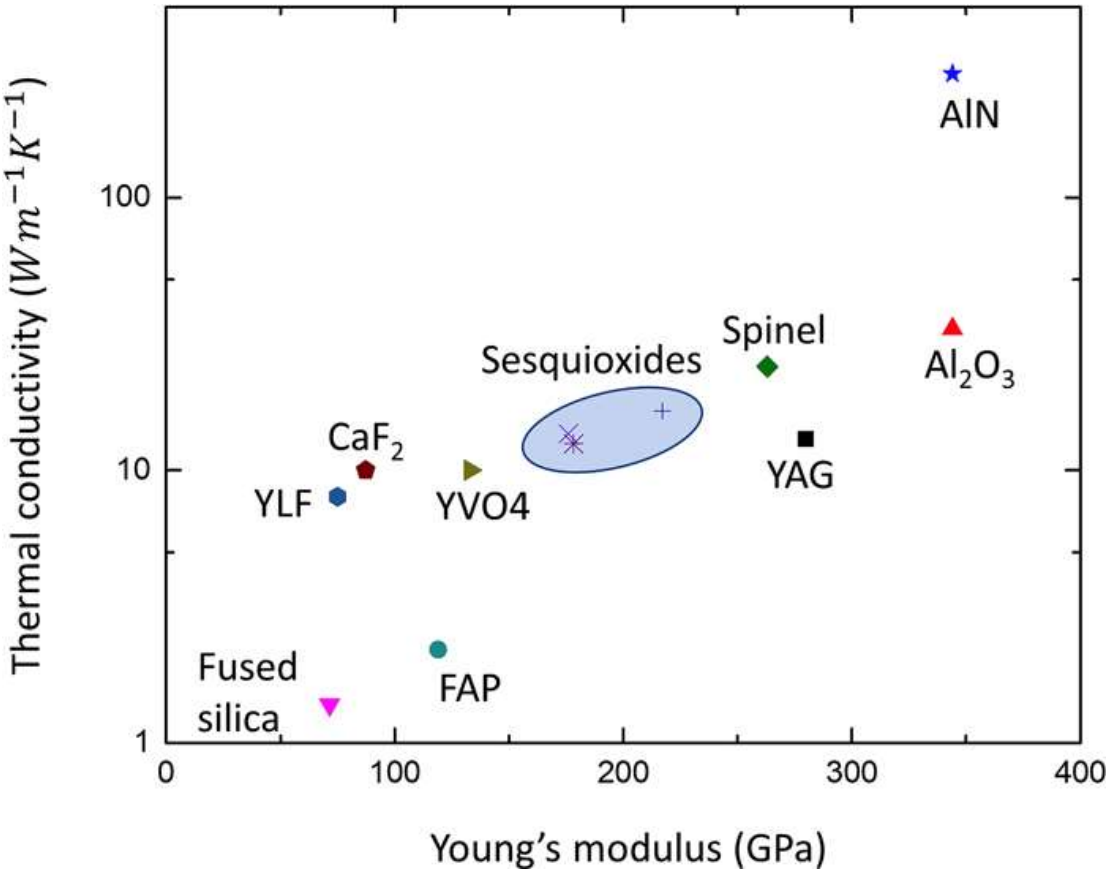

Figure 1.1: Room Temperature Thermal Conductivity of Ceramic Materials vs. Young's Modulus of Common and Candidate Laser Host Materials [2], Reproduced with Permission of AIP Publishing

One of the common failures of laser gain materials is a thermal shock failure where the material is heated volumetrically, but cooled only at the surfaces. This leads to mechanical failure that is related to the material's fracture toughness, and the thermal conductivity of the material. Higher thermal conductivity materials are capably of dissipating heat faster and more efficiently, highlighting another benefit of selecting a higher thermal conductivity laser host material for study. An example of one of these failures can be seen in **Figure 1.2** where the alumina sample survived, but the YAG sample suffered a thermal shock failure.

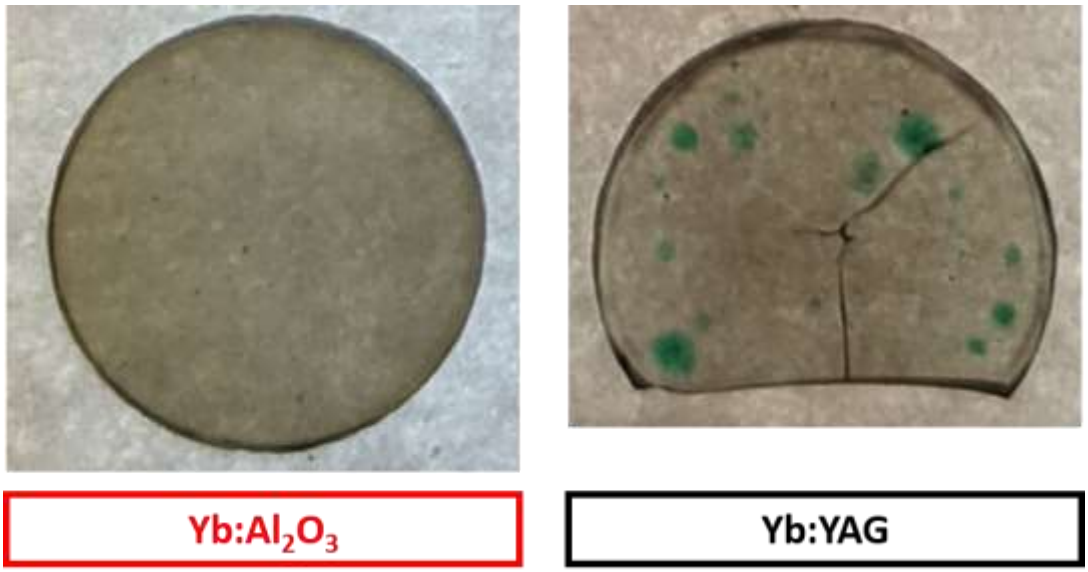

Figure 1.2: Backlit Photograph on Paper of Two Ytterbium Doped Laser Host Materials Pumped with 976 nm Laser Diode, (Left) Yb:Al_2O_3 Unharmed, (Right) Yb:YAG Suffered Thermal Shock Failure

Once a more powerful or higher energy laser is developed, the following question is what does it enable? For some it may allow more efficient operation with respect to current technologies, and others it may open the doors to studying new physics and laser material interaction (LMI). As lasers technologies have developed, not only has the everyday person been impacted, but the scientific community has come up with new and exciting ways to use lasers to better characterize materials. Atomic force microscopy (AFM) was enabled by the development of the laser, while Rahman Spectroscopy, which measures the vibration modes of atoms, has benefitted from improved wavelength availability of various lasers to provide monochromatic light as a measurement source. Laser induced breakdown spectroscopy (LIBS) is a more recent technique developed that utilizes HELs to measure spectra emitted from a material when interacting with a plasma at the material surface. More recently ceramics were welded using femtosecond pulses in zirconia [3]. None of these techniques would be possible without the continued development toward higher power laser systems.

The motivation for this work is to study two specific topics. 1. The development of high thermal conductivity materials for use as amplification materials, and 2. Study material behavior when exposed to high-energy lasers (HEL). The remaining sections of this chapter will walk through the background and rationale for the studies conducted and shared in the following chapters.

1.2. Introduction to Solid State Laser Gain Media

Solid state laser gain media, further referred to as gain media, is a category of materials used for the amplification of light in a coherent way. These materials are formed of a laser host material and a dopant. Some common and developing laser host materials were described in **Figure 1.1**. Fundamentally, a solid state laser is a system made up of this laser gain material, mirrors, and a pump or excitation source. **Figure 1.3** is a simplified schematic of a solid state laser where the excitation is a flash lamp, pumping or exciting the dopant electrons within the laser gain media. The photons oscillate between the two mirrors until a lasing threshold is reached, at which point the group of emitted photons are released through the partially reflective mirror.

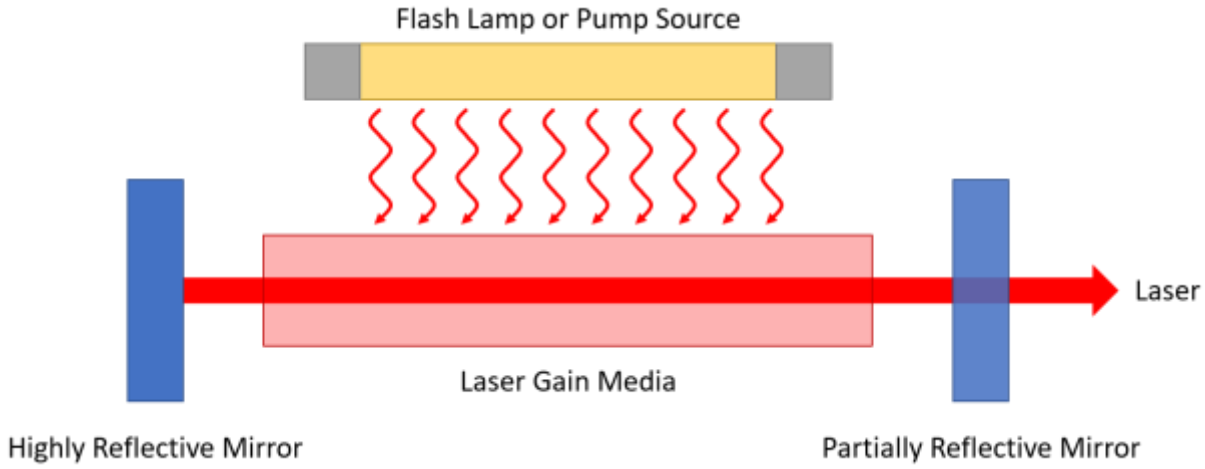

Figure 1.3: Schematic of a Pumped Solid State Laser

Emission from laser gain media can be broken up into a few different types of emission. Spontaneous emission is when an excited electron decays back to the ground state and emits a photon with a wavelength proportional to the energy differences of the excited state, and ground state. Spontaneous Emission is illustrated in **Figure 1.4**.

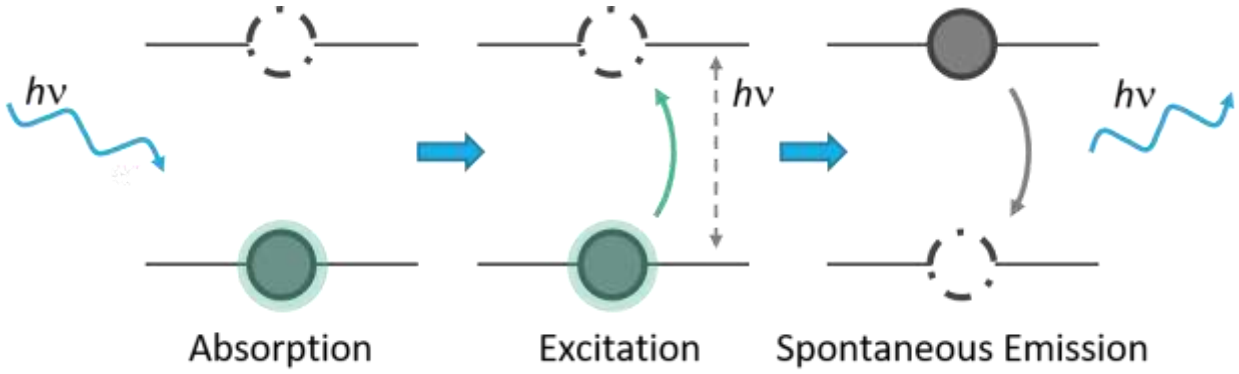

Figure 1.4: Schematic of Spontaneous Emission

Another form of emission is stimulated emission, or where the laser acronym "se" comes from. Stimulation emission occurs when an electron in the excited state decays and interacts with an additional photon that is pumped into the system. The result is multiple photons, of the same wavelength (energy) emitted from the decay to the ground state. This is the fundamental behavior used in lasing, where gain media is pumped to threshold, and the emitted photons are coherent and monochromatic. Stimulated emission is illustrated in **Figure 1.5**.

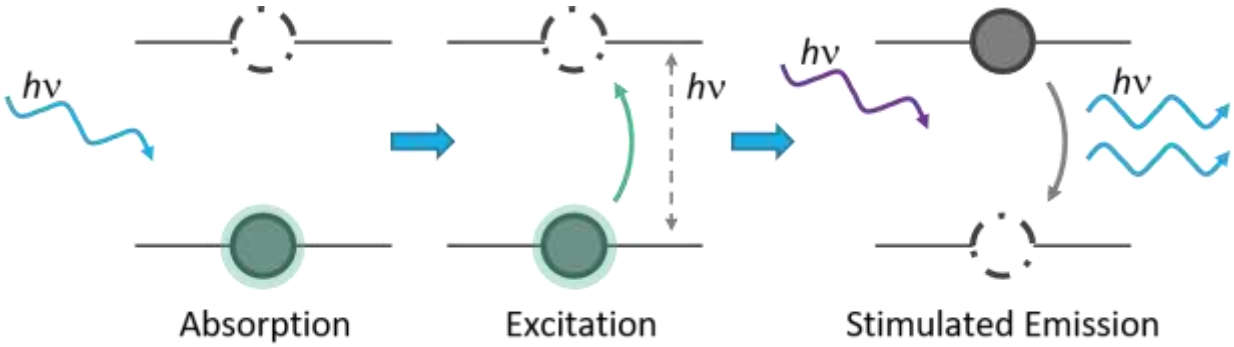

Figure 1.5: Schematic of Stimulated Emission

For a given active ion, or dopant, there is a characterized excitation and emission wavelength, and many of them have been categorized over the years and can be found in laser crystal textbooks [4]. Lasers are typically split into the three-level laser and a four-level laser, as shown in **Figure 1.6**. The difference between the three-level and four-level laser is how many non-radiative decay process occur (pictured with black arrows). Note that the non-radiative decay processes are fast process, while the radiative decay is treated as a slow process in comparison. Most common laser materials are four-level laser systems, like Nd:YAG, but for fiber optic cables, they treated as a three-level laser when co-doped with Erbium and Ytterbium. Four-level lasers are more commonly used because they do not need to regularly invert the entire population, but instead can invert the electron population at the state above the ground state. Three-level laser systems typically require significant pumping because of the need to regularly pump the ground state electrons after emission occurs. The ability to pump more efficiently and at higher power was a challenge early in the development of laser technologies, but with advancements in HEL technologies, pump sources are much more available than before.

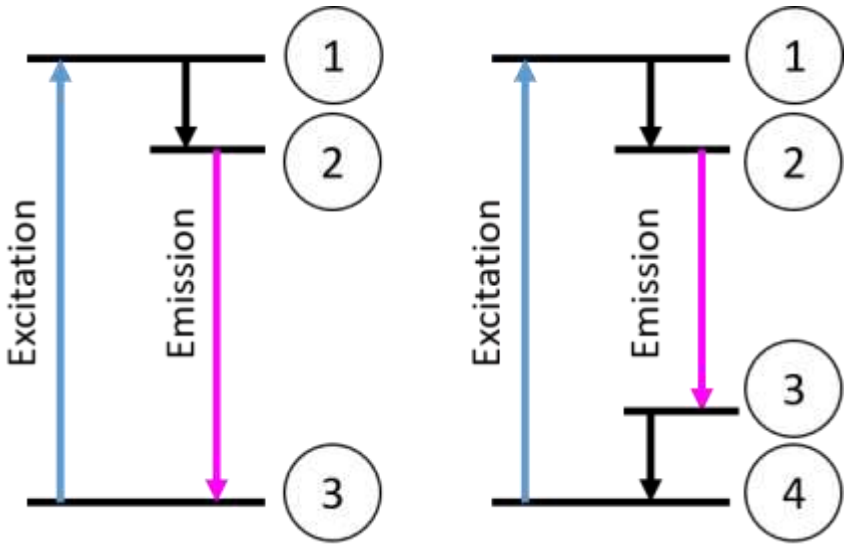

Figure 1.6: (Left) Simplified Energy Diagram for a Three-Level Laser, (Right) Simplified Energy Diagram for a Four-Level Laser, Black Arrows Represent Non-Radiative-Decay Transitions

For the three-level laser, there is a unique situation that is referred to as a quasi-three-level laser, where the lower non-radiative decay level is close to the ground state. Erbium and Ytterbium based gain media are typically treated as quasi-three-level laser systems. This situation is illustrated in **Figure 1.7**, where the lowest black arrow is used to describe this behavior. For these types of lasers, the lowest energy state can remain partially populated with excited electrons either from the pump source, or thermally from the host material heating up in the process. The quasi-three-level laser is still difficult to pump to emission, but it is doable with the developments in high-energy pump sources.

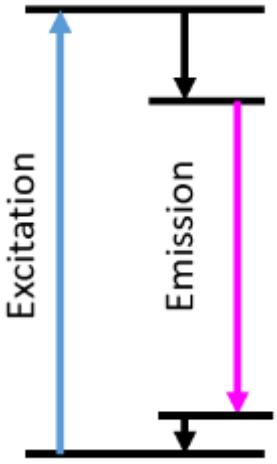

Figure 1.7: Simplified Energy Diagram for a Quasi-Three-Level Laser, Black Arrows Represent Non-Radiative-Decay Transitions

The gain media must be transparent to both the excitation and emission wavelength in order to successfully lase. In order to be transparent in the wavelength of interest, there cannot be significant losses from reflection, absorption, or scattering. The three loss mechanisms are briefly described as follows.

For a simple surface reflection model, where the light is perpendicular to the sample, the reflection of at each surface can be estimated using **Equation 1.1,** where n_1 is the index of refraction of the surrounding material, and n_2 is the index of refraction of the sample.

$$R_{\perp} = \left|\frac{n_1 - n_2}{n_1 + n_2}\right|^2 \qquad \text{(Eq. 1.1)}$$

Figure 1.8 is a simplified diagram of the reflection losses at each surface, assuming there are no contribution reflections within the material. This states that at each interface, for the index of refraction listed, there is an inherent loss of approximately 7% in-line transmission just from the index mismatch.

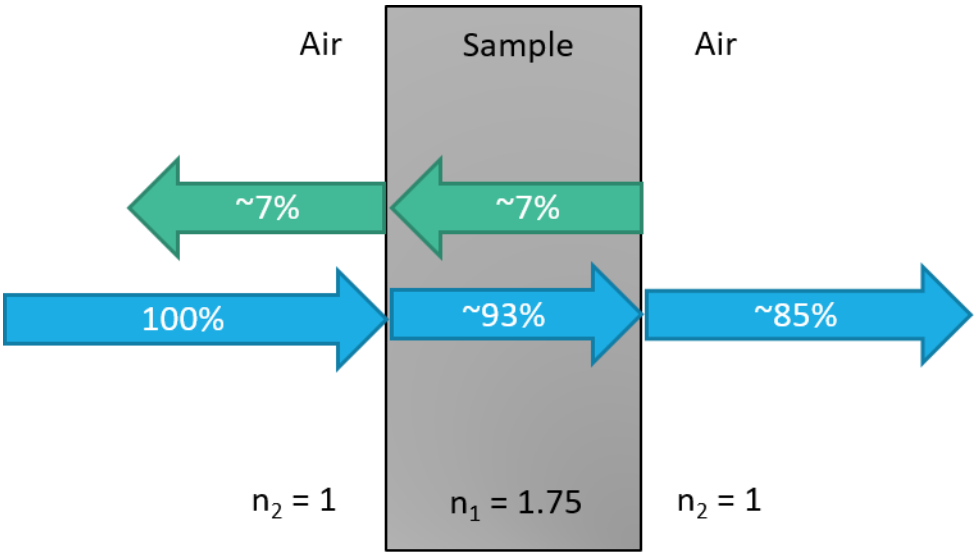

Figure 1.8: Schematic of Two Surface Reflection of Sample in Air

Absorption and scattering are typically tightly coupled and difficult to decouple loss mechanisms within a material. There are techniques to estimate the absorption contributions to an in-line transmission measurement, but it is difficult to fully quantify the scattering contribution with typical measurements. Instead, scattering is typically modeled as Rayleigh or Rayleigh-Gans-Debye (RGD) scattering. Rayleigh scattering follows a λ^{-4} behavior, while RGD scattering follows a λ^{-2} behavior, as described in **Equation 1.2** and **Equation 1.3**, where *l* is the thickness of a sample, and *K* is a coefficient related to the index of refraction of the material [5].

$$T_{Rayleigh} = e^{-K_{Ray}^4 \lambda^{-4} l} \quad \text{(Eq. 1.2)}$$

$$T_{RGD} = e^{-K_{RGD}^2 \lambda^{-2} l} \quad \text{(Eq. 1.3)}$$

Figure 1.9 is a plot of the two transmission equations using $l = 1$ and $K_{Ray} = K_{RGD} = 800$. This figure clearly demonstrates a difference in wavelength depending scattering behavior where Rayleigh scattering is fairly square shaped, and fairly flat a higher wavelengths, and RGD scattering has a more consistent shape that has an increase in transmission at higher wavelengths.

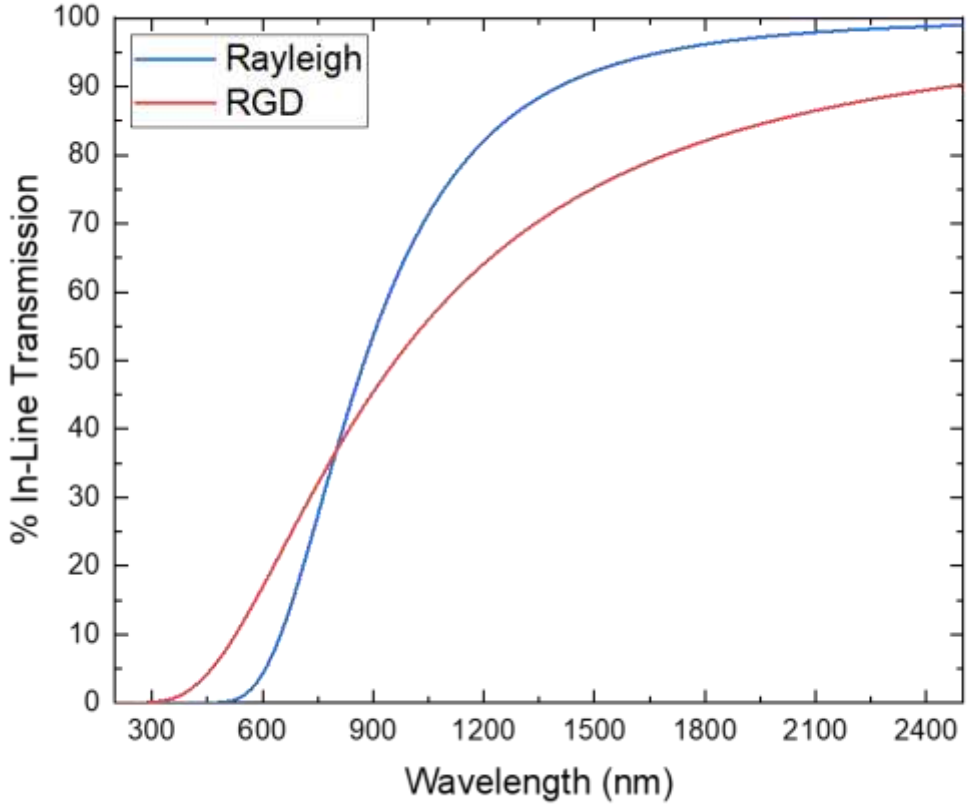

Figure 1.9: % In-Line Transmission vs. Wavelength for Rayleigh Scattering and RGD Scattering

Scattering in polycrystalline materials can be due to pores, as well as index mismatches. Pores, and similar vacancy defects are typically attributed with Rayleigh scattering, while index mismatches from secondary phases, or from anisotropic grain impacts, is typically attributed to

RGD scattering [5]. That said, previous work has shown that by decreasing the pores and birefringence index mismatches to much smaller than the wavelengths of light in interests, can improve transparence in many materials [6].

1.2.1. Alumina as a Host Material

Aluminum oxide, Al2O3, also known as synthetic sapphire has been studied as a higher thermal conductivity material, with the potential of being very transparent in the wavelengths of interests. Ever since Lucalox was developed and demonstrated that alumina could be made translucent when reducing porosity [7], transparent alumina has been a topic of study.

At UCSD in the AMPS lab, alumina has been studied as a laser host material with various dopants. Note that these samples begin with a nanocrystalline feed stock of alumina, and are rapidly densified through a process known as **C**urrent **A**ctivated **P**ressure **A**ssisted **D**ensification (CAPAD) [8]. Chromium was studied early as a polycrystalline equivalent of ruby, or the first laser [9]. From there work was conducted in developing Neodymium doped alumina and ultimately resulted in producing rare-earth doped alumina that showed laser gain [10]. Following successes with powder processing and densification techniques of alumina with various rare-earths, Thulium was used and the most transparent polycrystalline alumina ceramics ever fabricated was reported [11]. Building on the successes of all of the previous work with alumina as a host material, Ytterbium was selected as the next rare-earth to dope for use in laser applications.

1.2.2. Ytterbium as a Dopant

Ytterbium was selected to study for this work for multiple reasons. One, is that it has a high quantum defect efficiency, or the ratio of the excitation wavelength and emission wavelength, and because it has been noted to have long upper state lifetimes, between ~750 μs [12] and ~1100 μs [13]. Ytterbium is also interesting in that is rarely shows concentration quenching effects, where the dopant ions interact with each other instead of the pump light. There have been studies of doping Ytteribium into host materials up to 30 at. % [13]. Ytterbium also has one of the simplest electron structures of common laser gain media dopants, in that it only has one excited state manifold. A simplified laser energy diagram of Ytterbium can be seen in **Figure 1.10**.

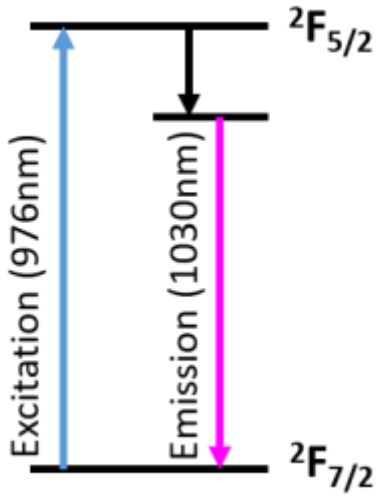

Figure 1.10: Laser Energy Diagram of Ytterbium

Ytterbium doped gain media was historically pumped at 940 nm, but with the continued development of Ytterbium and Erbium co-doped glass fibers, pumping near 980 has become more popular for the commercial communications industry.

1.2.3. Ytterbium Doped Ceramics

Many have studied ytterbium doped ceramics over the years, with an increase in studying these materials as gain media in recent years. Many garnets have been studied in addition to sesquioxides due to their increased thermal conductivity as an undoped crystalline materials as shown in **Figure 1.1**. Note that many Yb doped ceramics are reported as being blue or green in color after initial densification due to the conversion of Yb^{3+} to $Yb2^{+}$ in the reducing densification environments. This is typically remedied with annealing in air or an oxygen rich environment.

Single crystal Yb:YAG in multiple doping concentrations was reported to be grown using the czochralski method [13]. The concentrations studied were 2.5, 5, 10, 20, and 30 at. % [13]. These doping concentrations are not typically seen with other rare-earths in YAG or other host materials, reiterating the unique characteristics of Ytterbium and the lack of concentration quenching effects.

Polycrystalline Yb:YAG was vacuum sintered at 1730°C 10 hours [14]. These samples were doped at 1 at. %, and utilized a sintering additive tetraethyl oirthosilicate (TEOS) in the mixing process [14]. The powders were dried, sieved, pressed to 100MPa prior to Cold Isostatic Pressing (CIP) 250MPa. Thee green body was then calcined at 1000°C, prior to vacuum sintering [14]. Last, the densified ceramic was annealed at 1450°C for 20 hours in air to improve transparency [14].

Polycrystalline Yb:Lutetium Aluminum Garnate (LuAG) was vacuum sintered at 1790°C for 12 hours, annealed 1450C for 15 hours [15]. The doping concentrations for samples was 5, 10, and 15 at. % doped [15]. The feedstock was 250nm powder, processed with a planetary ball mill for 15 hours, and used TEOS as a sintering aid [15]. The powder was dried, sieved with a 100 mesh, and calcined at 800°C for 3 hours prior to being pressed at 15 MPa, then CIP'd at 200MPa before final densification [15].

3.6 at. % doped Yb:LuAG was reported to be fabricated with vacuum furnace (10^{-3} Pa) at 1800°C for 5 hours, [16]. These samples also used TEOS as a sintering aid, and annealed the samples at 1300°C for 5 hours [16].

Additionally samples of 5 at. % doped Yb:Lu_2O_3 was vacuum sintered between 1500°C and 1750°C for 2 hours [17]. The powders were calcined 1100°C, and the bulk sintered samples were subjected to Hot Isostatic Press (HIP) at 1700C for 8 hours [17].

Many of these Yb doped ceramics utilize multiple processes, introduce impurities in the form of sintering aids, and require hot processing techniques to fully densify the materials.

It is also interesting to note that the lasing threshold of Ytterbium doped ceramics was shown to decrease significantly with the decrease in temperature of the gain media [18]. This is a technique that can be used to improve the lasing performance of Ytterbium doped ceramics due to them being quasi-three-level laser. Improved emission of samples has been shown near 70 K or -200°C [13].

1.2.4. Ytterbium Doped Glasses

Ytterbium has been used as dopant in glasses for years, but not as the sole active ion. Ytterbium is typically co-doped with Erbium to enhance the absorption characteristics of the glass fibers, and has been an enabling technology for the commercial communications industry.

Yb doped glass and Yb-Al doped glasses have been reported to be sintered 1150°C for 2 hours [12]. To introduce the dopant ions, the glass was etched, soaked in a doping solution, and then sintered [12].

YbF and Yb doped glass fibers were reported to be fabricated using a molten core method [19]. These fibers with various compositions were fabricated by pulling a molten glass tube filled with powder materials that is integrated into the glass fiber when cooled [19]. The study presented long lifetimes for many of the glass fibers, with absorption cross section near $1.8x10^{-20}$ cm^2 near 976 nm and emission cross section near $4x10^{-21}$ cm^2 near 1010 nm [19].

1.3. Introduction to Laser Material Interaction

As previously mentioned, having access to higher-energy laser systems has opened new fields of study and new techniques for understanding materials. In those areas of study, a major focus has been in understanding the fundamentals of laser material interaction (LMI) as a function of various parameters. At the most fundamental levels, LMI aims to study how energy deposited in the form of light behaves within a material. When photons impact a material, they can reflect, absorb, or scatter as stated previously. At a slightly larger scale, the light can heat, melt, damage/crack, ablate, and/or vaporize the material depending on how the photons energy is coupled into the material.

In many LMI experiments, one of the key goals is to generate a pressure in a material, and understand the material response to that pressure. To generate pressures in materials there are a few techniques employed. The most basic ablation where a laser is focused at the surface of a material, further referred to as untamped ablation, is described in **Figure 1.11**. In this schematic, the material is irradiated by the laser pulse, and there is a localized deformation or melt from the heat and pressures generated by the laser near the surface of the material. During this process, a pressure wave is launched into the substrate. Depending on the intensities used, this can have different material responses, but the schematic highlights many of the behaviors that typically occur. If the material is raised to high enough temperatures, it can be ejected as a vapor or a plasma, back in the direction of the laser pulse, and can generate a shock wave when experiments are conducted in air or gaseous atmospheres.

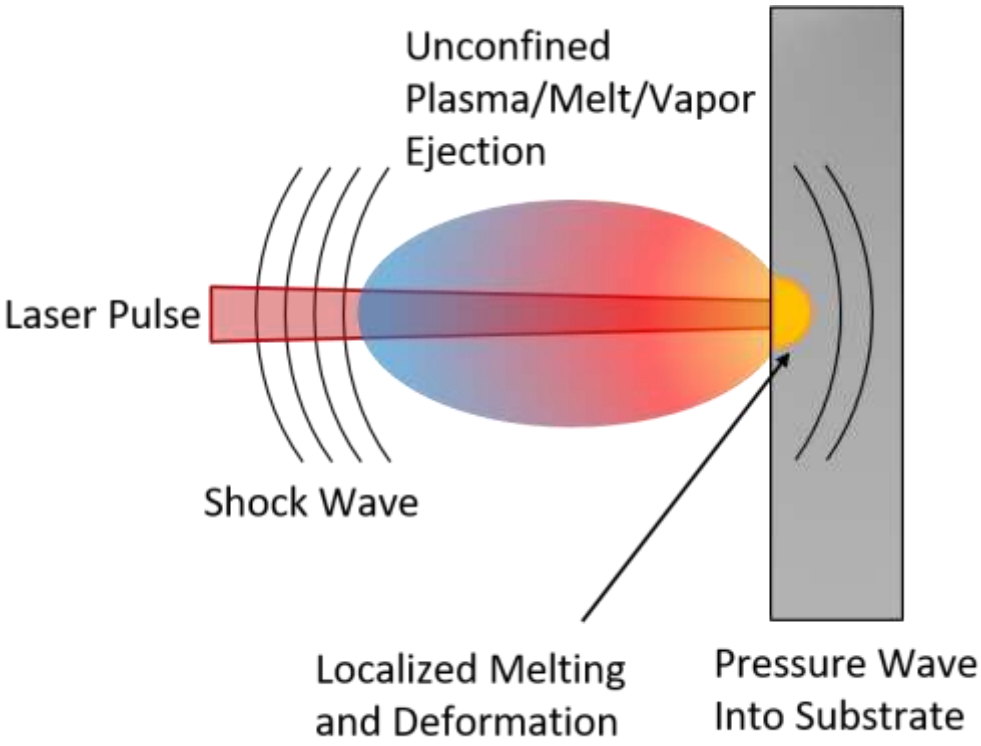

Figure 1.11: Schematic of Untamped Ablation

For untamped ablation, the energy input in to the material is split into generating both the pressure wave in the substrate, and the shock wave generated from the ablated material ejection. In order to improve the energy coupling into the material, tamped ablation is a technique employed and described in **Figure 1.12**. For this type of ablation, a tamper material that is transparent to the wavelength of the laser pulse is bonded to or deposited on the substrate. The laser is focused at the interface of the tamper material and the substrate, in an attempt to confine the material interacting with the laser pulse. This confinement allows for more of the energy to be transferred into the substrate, since there is no ejected material and shock wave generated, and can be used to reach higher pressures in substrates.

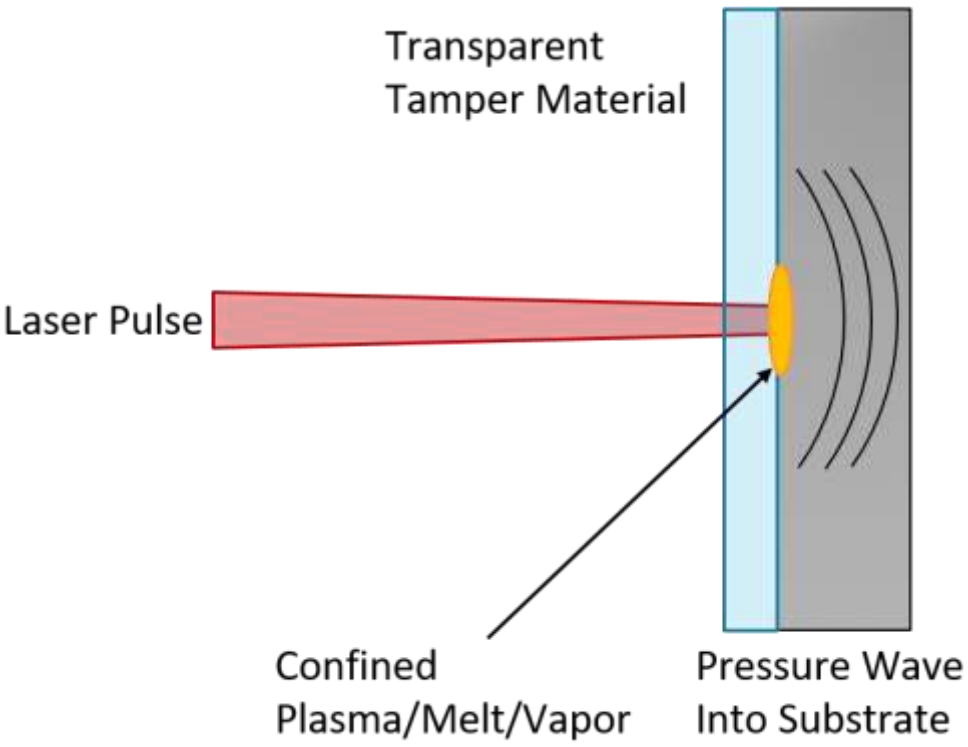

Figure 1.12: Schematic of Tamped Ablation

A third type of ablation is similar to a combination of the previous two ablation ideas, but utilizes a non-transparent material instead of a transparent tamping material to generate a pressure. This material is referred to as the ablator typically a metal or plastic layer, deposited on or bonded to material of interest. The ablator is driven with the laser, ablating some or all of the layer, and drives a shock into the material of interest. This type of ablation study has been described with plastic ablator layers for driving shocks into metals [20] and metal ablator layers for driving shocks into graphite [21], as examples of this using these techniques to generate pressures in materials.

The mechanical impedance of a material can be compared to that of the speed of sound of a material, in that how a mechanical shock moves through a material is very similar to how a sound wave travels through media. The speed of sound in a solid material, c, is calculated using **Equation 1.4**, where B is the bulk modulus of the material, and ρ is the density of the material.

$$c = \sqrt{\frac{B}{\rho}} \qquad \text{(Eq. 1.4)}$$

The bulk modulus can be calculated through a relationship of the Young's Modulus, E, and the Poisson's Ratio, ν, using **Equation 1.5**.

$$B = \frac{E}{3(1-2\nu)} \qquad \text{(Eq. 1.5)}$$

The speeds of sounds of some common materials that will be discussed throughout Chapter 3 are listed in **Table 1.1**.

Table 1.1: Material Properties of Common Materials

Material	Density, ρ [g/cm^2]	Poisson's Ratio, ν	Young's Modulus, E [GPa]	Bulk Modulus, B [GPa]	Sound Speed in material, c [km/s]
Aluminum	2.71 [22]	0.33 [22]	69 [22]	67	4.9
Sapphire	3.98 [22]	0.22 [22]	380 [22]	225	7.5
Silicon (100)	2.33 [22]	0.28 [22]	129 [22]	98	6.5
Soda-Lime Glass	2.50 [22]	0.23 [22]	69 [22]	43	4.1

In both the tamped ablation, and the ablator driven ablation situations, the mechanical impedance of the materials is a critical factor when measuring mechanical shocks across interfaces. If there is a significant mismatch in the impedance, the shock may reflect or dissipate when meeting a dissimilar material. For example, aluminum on sapphire is a significant mismatch with sapphire having 1.5 times the material sound speed as aluminum. This is in stark contrast to aluminum on soda-lime glass, where they have very similar speeds of sound as shown in **Table 1.1**.

1.3.1. Metals

Many LMI studies have been focused on the behavior of different metals, to better understand the material response to high pressures and validate the equations of state. A non-exhaustive list of these metals includes iron [23], aluminum [24], tantalum [25], and zirconium [26]. In these metals, some undergo phase transitions at high enough temperatures and pressures, while others are expected to maintain their phase across the laser ablation driven shock pressures.

A tabletop Ti:sapphire laser system was used to compress untamped iron targets deposited on glass substrates to support velocimetry data acquisition [23]. The pulse length was ~270 ps and the wavelength was centered near 800 nm [23]. Iron phase changes were observed from α to ε approximately 100 ps after being compressed with 10-25 GPa pressures [23].

Stepped aluminum targets, meaning multiple thicknesses on a single substrate, were sputtered on glass and compressed using ~270 ps pulse duration centered at 800 nm on a Ti:sapphire laser [24]. This set of experiments was configured for tamped ablation, where the pump beam was focused at the glass and aluminum interface, and a pair of time delayed probe pulses were reflected off of the aluminum surface to measure surface velocity [24]. The peak pressures measured in the aluminum was 43 GPa [24].

Similarly, a Ti:sapphire laser with 350 ps pulse duration, centered at 800nm, was used to ablate tantalum targets deposited on single crystal sapphire substrates [25]. This set of experiments was also configured for tamped ablation, with the pump beam focused at the sapphire and tantalum interface [25]. Measured pressures within the tantalum were between 4 GPa and 22 GPa [25].

The Linear Coherent Light Source (LCLS) was utilized to study phase transitions in zirconium with in-situ x-ray diffraction (XRD) using an arrayed target to allow many shots to be analyzed per target [26]. Zirconium was deposited onto a silicon nitride coated silicon wafer [26]. An aluminum ablator layer was deposited on the zirconium to generate higher pressures in the zirconium [26]. Pressures of 100 GPa 130 GPa was observed in the aluminum and zirconium layers respectively [26]. At these pressures it was observed that both metals rapidly melted and the zirconium recrystallized into the β phase [26].

1.3.2. Semiconductors

Silicon is the model semi-conductor material, and used in almost every piece of technology that we use today. In reviewing different LMI studies of silicon, there was significant breadth to the topics of study, and many of the published work was focused on optimizing laser damage parameters for use in replacing chemical etching. Silicon ablation studies are primarily focused on processing of the material, and typically the laser ablation of silicon is untamped. Putting together a literature comparison of silicon LMI studies over the last two decades, **Figure 1.13** was created to aid in identifying trends of previous work, and identify areas for further study. Note that for work that stated undoped or intrinsic silicon and did not provide a free carrier density, the free carrier density was assumed to be $1x10^{10}$ cm^{-3} at room temperature [27].

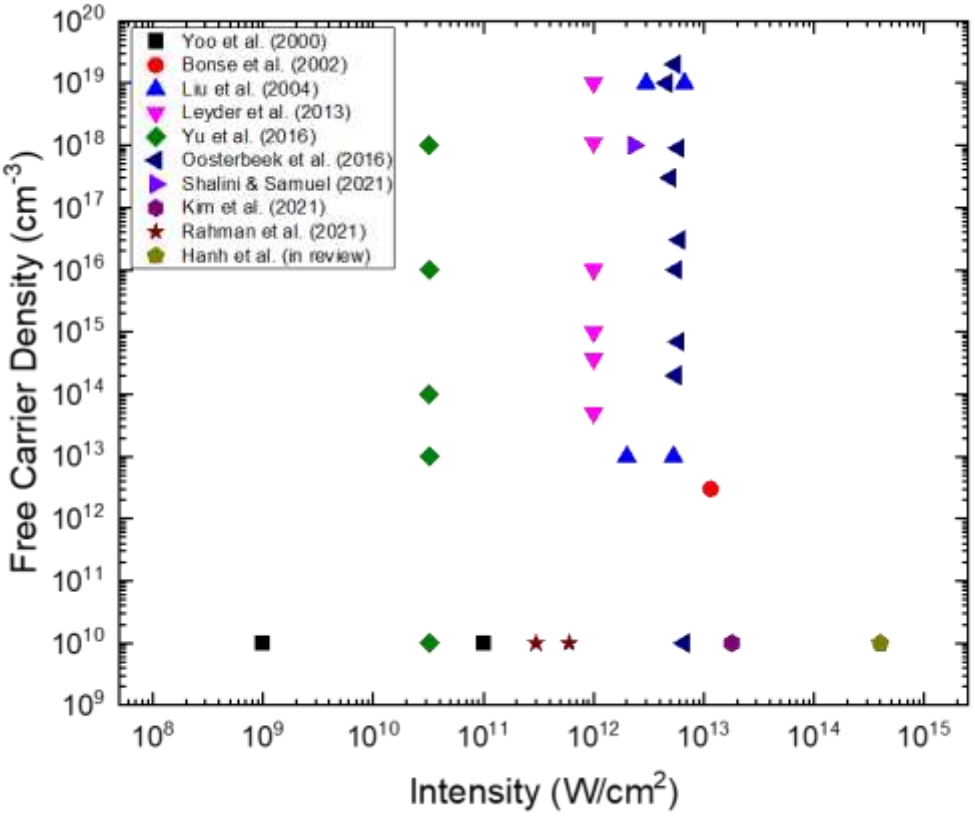

Figure 1.13: Literature Comparison of Silicon Free Carrier Density (Doping Concentration) vs. Intensity, Log Scale [28-37]

It is interesting to note that there is a steep drop off of work at intensities above $1x10^{12}$ W/cm^2 and $1x10^{13}$ W/cm^2. It is also interesting to see how others have looked at free carrier effects in the past, and learn from their studies to inform new contributions to the boy of work. Lower intensities appear to be the primary area of study, and the range of free carrier densities spans nine orders of magnitude. This range in free carrier density, and the lack of work available at higher intensities provides a unique opportunity for further study that will be discuss in **Chapter 4**.

1.4. References

[1] Maiman, T. H. “Stimulated Optical Radiation in Ruby.” *Nature* 187 (1960): 493–494.

[2] Wu, X., Tang, L., Hardin, C. L., Dames, C., Kodera, Y., and Garay, J. E. "Thermal conductivity and management in laser gain materials: A nano/microstructural perspective." *Journal of Applied Physics* 131.2 (2022).

[3] Penilla, E. H., Devia-Cruz, L. F., Wieg, A. T., Martinez-Torres, P., Cuando-Espitia, N., Sellappan, P., Kodera, Y., Aguilar, G., and Garay, J. E. "Ultrafast laser welding of ceramics." *Science* 365.6455 (2019): 803-808.

[4] Kaminskii, Alexander A. "Laser Crystals Their Physics and Properties." *Springer Series in Optical Sciences* (1990): 214.

[5] Shachar, M. H., Uahengo, G., Penilla, E. H., Kodera, Y., and Garay, J. E. "Modeling the effects of scattering and absorption on the transmission of light in polycrystalline materials." *Journal of Applied Physics* 128.8 (2020).

[6] Kodera, Y., C. L. Hardin, and J. E. Garay. "Transmitting, emitting and controlling light: Processing of transparent ceramics using current-activated pressure-assisted densification." *Scripta Materialia* 69.2 (2013): 149-154.

[7] Burke, Joseph E. "Lucalox alumina: the ceramic that revolutionized outdoor lighting." *MRS Bulletin* 21.6 (1996): 61-68.

[8] Garay, J. E. "Current-activated, pressure-assisted densification of materials." *Annual review of materials research* 40 (2010): 445-468.

[9] Penilla, E. H., Hardin, C. L., Kodera, Y., Basun, S. A., Evans, D. R., and Garay, J. E. "The role of scattering and absorption on the optical properties of birefringent polycrystalline ceramics: modeling and experiments on ruby (Cr: Al2O3)." *Journal of Applied Physics* 119.2 (2016).

[10] Penilla, E. H., Devia-Cruz, L. F., Duarte, M. A., Hardin, C. L., Kodera, Y., and Garay, J. E. "Gain in polycrystalline Nd-doped alumina: leveraging length scales to create a new class of high-energy, short pulse, tunable laser materials." *Light: Science & Applications* 7.1 (2018): 1-12.

[11] Wu, Xingzhong, Yasuhiro Kodera, and Javier E. Garay. "Fabrication of highly transparent thulium-doped Al2O3 nanocrystalline ceramics with broadband emission at 1.8 μm." *Optical Materials* 133 (2022): 113082.

[12] Qiao, Y., Wen, L., Wu, B., Ren, J., Chen, D. and Qiu, J. "Preparation and spectroscopic properties of Yb-doped and Yb–Al-codoped high silica glasses." *Materials Chemistry and Physics* 107.2-3 (2008): 488-491.

[13] Dong, J., Bass, M., Mao, Y., Deng, P. and Gan, F. "Dependence of the Yb 3+ emission cross section and lifetime on temperature and concentration in yttrium aluminum garnet." *JOSA B* 20.9 (2003): 1975-1979.

[14] Wu, Y., Li, J., Pan, Y., Guo, J., Jiang, B., Xu, Y. and Xu, J. "Diode-pumped Yb: YAG ceramic laser." *Journal of the American Ceramic Society* 90.10 (2007): 3334-3337.

[15] Luo, D., Zhang, J., Xu, C., Yang, H., Lin, H., Zhu, H. and Tang, D. "Yb: LuAG laser ceramics: a promising high power laser gain medium." *Optical Materials Express* 2.10 (2012): 1425-1431.

[16] Basyrova, L., Loiko, P., Maksimov, R., Shitov, V., Serres, J.M., Aguiló, M., Díaz, F., Griebner, U., Petrov, V. and Mateos, X. "Efficient laser operation of Yb: Lu3Al5O12 transparent ceramics fabricated from laser ablated nanopowders." *Solid State Lasers XXIX: Technology and Devices*. Vol. 11259. SPIE, 2020.

[17] Liu, Q., Li, J., Dai, J., Hu, Z., Chen, C., Chen, X., Feng, Y. and Li, J. "Fabrication, microstructure and spectroscopic properties of Yb: Lu2O3 transparent ceramics from co-precipitated nanopowders." *Ceramics International* 44.10 (2018): 11635-11643.

[18] Casagrande, O., Deguil-Robin, N., Le Garrec, B. and Bourdet, G.L. "Cryogenically cooled ytterbium doped sesquioxide ceramic lasers." *LEOS 2006-19th Annual Meeting of the IEEE Lasers and Electro-Optics Society*. IEEE, 2006.

[19] Cavillon, M., Kucera, C., Hawkins, T.W., Yu, N., Dragic, P. and Ballato, J. "Ytterbium-doped multicomponent fluorosilicate optical fibers with intrinsically low optical nonlinearities." *Optical Materials Express* 8.4 (2018): 744-760.

[20] Swift, Damian C., and Kraus, Richard G. "Properties of plastic ablators in laser-driven material dynamics experiments." *Physical Review E* 77.6 (2008): 066402.

[21] Armstrong, M.R., Radousky, H.B., Austin, R.A., Tschauner, O., Brown, S., Gleason, A.E., Goldman, N., Granados, E., Grivickas, P., Holtgrewe, N. and Kroonblawd, M.P. "Highly ordered graphite (HOPG) to hexagonal diamond (lonsdaleite) phase transition observed on picosecond time scales using ultrafast x-ray diffraction." *Journal of Applied Physics* 132.5 (2022).

[22] Callister Jr, William D., and Rethwisch, David G. “Materials science and engineering an introduction.” *Wiley* 2014.

[23] Crowhurst, J.C., Reed, B.W., Armstrong, M.R., Radousky, H.B., Carter, J.A., Swift, D.C., Zaug, J.M., Minich, R.W., Teslich, N.E. and Kumar, M. "The $\alpha \rightarrow \epsilon$ phase transition in iron at strain rates up to$\sim 10^9$ s^{-1}." *Journal of Applied Physics* 115.11 (2014).

[24] Crowhurst, J.C., Armstrong, M.R., Knight, K.B., Zaug, J.M. and Behymer, E.M. "Invariance of the dissipative action at ultrahigh strain rates above the strong shock threshold." *Physical review letters* 107.14 (2011): 144302.

[25] Crowhurst, J.C., Armstrong, M.R., Gates, S.D., Zaug, J.M., Radousky, H.B. and Teslich, N.E. "Yielding of tantalum at strain rates up to 109 s− 1." *Applied Physics Letters* 109.9 (2016).

[26] Radousky, H.B., Armstrong, M.R., Austin, R.A., Stavrou, E., Brown, S., Chernov, A.A., Gleason, A.E., Granados, E., Grivickas, P., Holtgrewe, N. and Lee, H.J. "Melting and refreezing of zirconium observed using ultrafast x-ray diffraction." *Physical Review Research* 2.1 (2020): 013192.

[27] Sproul, A. B., and M. A. Green. "Improved value for the silicon intrinsic carrier concentration from 275 to 375 K." *Journal of applied physics* 70.2 (1991): 846-854.

[28] Yoo, J. H., Jeong, S. H., Greif, R., & Russo, R. E. "Explosive change in crater properties during high power nanosecond laser ablation of silicon." *Journal of Applied physics* 88.3 (2000): 1638-1649.

[29] Bonse, J., Baudach, S., Krüger, J., Kautek, W., & Lenzner, M. "Femtosecond laser ablation of silicon–modification thresholds and morphology." *Applied Physics A* 74 (2002): 19-25.

[30] Liu, H. H., Mourou, G., Picard, Y. N., Yalisove, S. M., & Juhasz, T. "Effects of wavelength and doping concentration on silicon damage threshold." *Conference on Lasers and Electro-Optics*. Optica Publishing Group, 2004.

[31] Leyder, S., Grojo, D., Delaporte, P., Marine, W., Sentis, M., & Utéza, O. "Non-linear absorption of focused femtosecond laser pulses at 1.3 μm inside silicon: Independence on doping concentration." *Applied Surface Science* 278 (2013): 13-18.

[32] Yu, X., Wang, X., Chanal, M., Trallero-Herrero, C. A., Grojo, D., & Lei, S. "Internal modification of intrinsic and doped silicon using infrared nanosecond laser." *Applied Physics A* 122 (2016): 1-7.

[33] Oosterbeek, R. N., Corazza, C., Ashforth, S., & Simpson, M. C. "Effects of dopant type and concentration on the femtosecond laser ablation threshold and incubation behaviour of silicon." *Applied Physics A* 122 (2016): 1-10.

[34] Shalini, S., and G. L. Samuel. "Ultrafast pulse laser inscription and surface quality characterization of micro-structured silicon wafer." *Journal of Manufacturing Processes* 62 (2021): 323-336.

[35] Kim, B., Nam, H. K., Ryu, J., Kim, Y. J., & Kim, S. W. "Non-periodic nanoscale structuring of crystalline silicon surface by using ultrashort laser pulses." *Applied Surface Science* 565 (2021): 150595.

[36] Rahman, T.U., Khan, R.A.A., Qayyum, H., Amin, U., Ullah, S., Dogar, A.H., Mahmood, A., Rafique, M. and Qayyum, A. "Characterization of microcraters fabricated on the silicon surface by single and multi-pulse laser ablation at various laser intensities." *Nuclear Instruments and Methods in Physics Research Section B: Beam Interactions with Materials and Atoms* 487 (2021): 45-51.

[37] Hanh, E. N., Bailly-Grandvaux, M., Cordova, T., Turner, R. E., Joshi, T.R., Spielman, R.B., Wicks, J. K., Garay, J. E., Beg, F. N. “Laser pulse-length dependent ablation and shock generation in silicon at $4x10^{14}$ W/cm^2 intensities.” *Physical Review Research* – in Review

CHAPTER 2. AMPLIFICATION MATERIALS

2.1. Introduction to Chapter 2

The following chapter highlights the experimental methods and techniques employed to study rare-earth doped ceramics. The results section walks through the data generated from this effort, and shares the success in the development of highly transparent Ytterbium doped alumina ceramics. Through detailed processing and characterization of these materials, we prove that this material is suitable for additional testing including laser gain experiments. We also highlight the unique possibility of using this material for amplification of nanosecond and femtosecond pulses in the future.

2.2. Experimental Methods

2.2.1. Powder Processing

High-purity TM-DAR α-alumina (Al_2O_3), (99.99% pure, Taimei Chemicals, Japan) was used as the host material for all powder processing techniques. Rare-earth oxides and rare-earth nitrates were mixed into the alumina powder via different methods. Ytterbium Oxide nanopowder (Yb_2O_3), (99.7% pure, Sigma-Aldrich, USA) and Ytterbium Nitrate ($Yb(NO_3)_3 \cdot 5H_2O$), (99.999% pure, Sigma-Aldrich, USA) were utilized as rare-earth dopant sources. Phase purity of TM-DAR and the Yb_2O_3 powders were verified using x-ray diffraction (XRD) measurements on a PANalytical X'Pert (Phillips, Japan) in ambient conditions. Measured diffraction peaks of the two powders compared to reference peaks from the Inorganic Crystal Structures Database (ICSD). The nitrate dopant source was a water stabilized crystal,

and extremely hygroscopic, so it was not able to be measured with the XRD in ambient conditions due to the immediate absorption of water from the air.

Careful attention to sources of contamination was taken throughout all powder processing steps. Handling of powders was conducted in an enclosed clean box environment with HEPA filtered laminar flow from above, and an exhaust system return from below the mesh working surface.

When using rare-earth oxide dopant, Yb_2O_3, three separate mixing processes were implemented prior to densification in to a bulk ceramic. **Figure 2.1** is a simplified flow diagram of the mixing processes used.

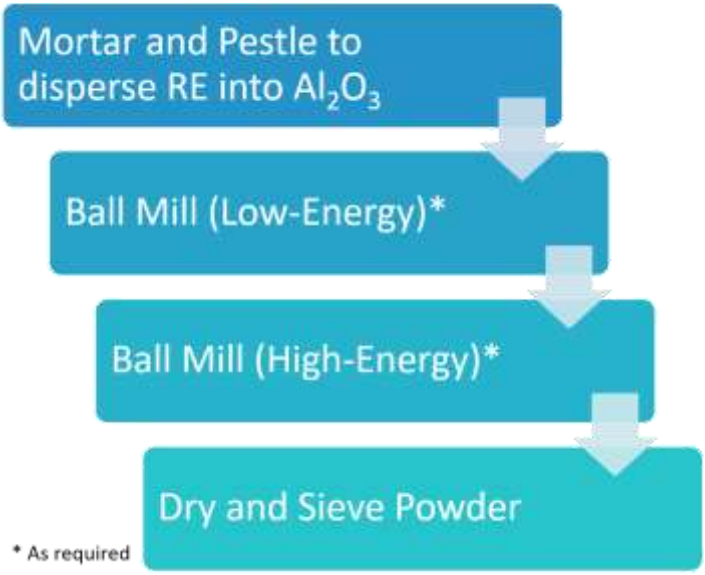

Figure 2.1: Powder Mixing Process Diagram

All powder processing methods began with an alumina mortar and pestle step to help disperse the dopant throughout the alumina powder. A small amount of TM-DAR was added into a Coorstek mortar and spread out with the pestle. The entire amount of rare-earth powder

was then added to the TM-DAR, and mixed for approximately 15 minutes to disperse the dopant into the small amount of TM-DAR. Then in two more successive steps, the TM-DAR was added to the mix to dilute the powder mixture into the desired amount of TM-DAR powder. The total mortar and pestle time was between 45 and 60 minutes in length.

Low-energy ball milling (LEBM) was performed using a 1:15 powder to grinding media mass ratio. The grinding media used was 3 mm diameter alumina media (MSE Supplies, USA). This means for a typical 3.5 grams of TM-DAR mixed with the rare-earth, there would be 53 grams of grinding media added to a glass jar with the powder. Ultra-high purity (UHP) water was added to the jar using a 1:20 powder to UHP water mass ratio, or 70 grams of UHP water for a typical processing step. The jar was sealed with a lid, and taped to ensure that the lid would not unscrew from rotation and vibration. The jar was then placed on rollers at running at approximately 100 rpm for 12 hours.

High-energy ball milling (HEBM) was performed using a Fritsch Pulverisette 7 (Fritsch, Germany) planetary ball mill. For all mixing processes, a 1:10 powder to grinding media mass ratio was used. The grinding media used was 3 mm diameter silicon nitride spherical media. For HEBM the typical powder amount used is 3 grams of TM-DAR mixed with rare-earth, so 30 grams of grinding media was added to a silicon nitride lined jar. For dry mixing, the jar is run at 350 PRM for 18, 10 minutes cycles. Between each dry cycle, the jar is opened, and the powder agglomerates on the base of the jar are dislodged with a thin metal spatula to provide more even mixing of the powders. For wet mixing processes a 1:13.33, or 3:40 powder to UHP water mass ratio was added to the jar prior to mixing. The wet process is run at 150 RPM for 36, 10 minute cycles, with 2 minute pauses between each cycle to allow the jar and system to cool. For the wet processes, there was no opening of the jar between steps.

For all wet processes, an AccuSpin 1 benchtop centrifuge (Fisher Scientific, USA) was used to separate the water from the powder. The powder and UHP water mixture was removed from the mixing jar using a pipette, and placed into a plastic centrifuge tube. A second centrifuge tube was filled with deionized water until the masses of the two tubes were within one gram of each other to ensure balance of the equipment. The centrifuge was run in 10 minute cycles at 3400 RPM to separate the water from the powder as much as possible. Contaminated water was disposed of per university hazardous waste guidelines. The centrifuge operating steps were repeated as necessary to get all of the powder and UHP mixture out of the jar and into one centrifuge tube to be dried, typically taking two to three 10 minute cycles.

To dry any wet processed powder, a vacuum oven model DP-31 (American Gold, USA) was used. The centrifuge tube with wet powder was covered with a thin sheet of perforated aluminum foil to allow water to escape, but to prevent any contamination from the oven from impacting the powder. The oven was preheated to prevent significant overshooting prior to placing the powder inside. The vacuum pump was then turned on and the powders were left at 50-55°C for 24 hours.

Processing TM-DAR with the rare-earth nitrate dopant $Yb(NO_3)_3 \cdot 5H_2O$, was similar to the rare-earth oxide processing conditions, but due to the dopant crystal being water soluble, all mixing steps were conducted as dry processes. Mortar and pestle steps were identical to the oxide doping, and HEBM was the only mixing step used prior to densification. The same 1:10 powder to grinding media ratio was used, and the same silicon nitride lined jar and grinding media were used for nitrate based doping. Due to the hygroscopic nature of the nitrate crystals, the nitrate mixed TM-DAR powders were vacuum sealed in storage containers when not being sieved or packed prior to densification.

For both the oxide and nitrate based processes, the processed powder was sieved prior to densification using a 325 (< 40 μm agglomerate size) mesh. The mortar and pestle were utilized again to break up agglomerates of the processed powder prior to sieving. This was an iterative process of using the mortar and pestle and sieving to have enough sieved powder to densify multiple samples per batch of powder.

2.2.2. Densification

Densification of both undoped and rare-earth doped ceramics was conducted using **C**urrent **A**ctivated **P**ressure **A**ssisted **D**ensification (CAPAD). CAPAD is a technique developed to rapidly densify many materials, and leverages high heating rates, and uniaxial pressure to achieve full density in minutes versus traditional free sintering that can take hours or days [1].

All rare-earth doped ceramic samples fabricated for this work were approximately 1 centimeter diameter, and 1 millimeter thick after polishing. These samples use a Miniature-Sized Graphite Die (mini die) inside of a Full-Sized Graphite Die (full die), see **Figure 2.2**, where the sample can be seen between the mini die's two plungers. The full die bore was approximately 19 mm (0.75") diameter while the mini die bore was approximately 10 mm (0.38") diameter. The smaller area, and resulting smaller volume of each sample fabricated allowed for more samples to be fabricated with a single batch of powder. A perpendicular hole was drilled half of the thickness into the full die at the center height to provide a surface closer to the sample for temperature measurements during the run using an IR-CZQW2N infrared pyrometer (CHINO, Japan), which had an operating range of 400°C - 2000°C.

The mini die was packed with graphite foil around the inner diameter, as well as two sheets of graphite foil at the powder-plunger interface on both sides of the powder. This graphite

foil accounted for some planar variation of the stacked flat surfaces by being a compliant material under the uniaxial loading conditions of CAPAD. The graphite foil on the top and bottom of the sample were polished off prior to any optical measurements of a sample.

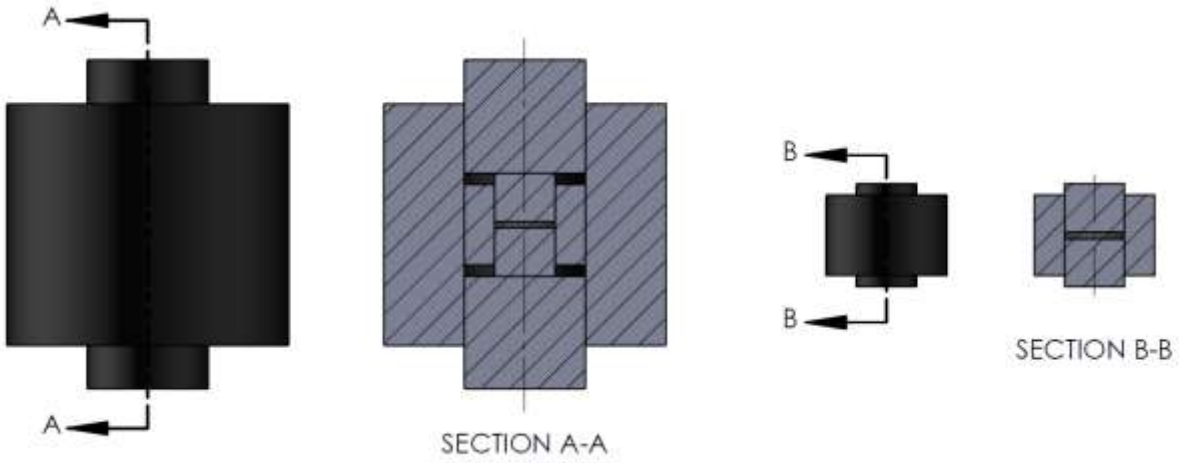

Figure 2.2: Schematic of Full-Sized Graphite Die (Left) and Miniature-Sized Graphite Die (Right)

Graphite felt jackets were employed to limit the radiative heat losses from the graphite in the chamber, and to have finer control of the heating and cooling rates of the full and mini die systems. Carbon fiber thread was used to sew the graphite felt pieces together. This jacket was composed of a tightly sewn graphite felt outer diameter cylinder and bottom flat surface that was sewn to the outer diameter cylinder. The top felt piece was not sewn to the outer diameter, but instead inset into the felt and secured with friction when packing the die. The bottom and top graphite felt pieces had a circle cut out of them to allow for the plungers to freely move. A small window was cut out at the midpoint to allow for the optical pyrometer to have a larger area to align to when setting up the run.

Nitrate processed powders were “baked” in CAPAD at 400°C to remove any excess water in the powder prior to pre-press. 10% of the typical uniaxial load, or 10 MPa, was used to hold the die in position during the “bake” process. This was a relatively quick process where the voltage was set to a constant value while the system ramped up in temperature. As soon as the system reached 400°C, the voltage was set back to 0 V and the system was allowed to cool prior to pre-press.

For both oxide and nitrate powder processing methods, the die setup was run through a pre-press process prior to densification. In this process, the full 100 MPa load was applied over 3 minutes, and the sample was held at load for 5 minutes prior to releasing the load. Pre-press allowed for more repeatable densification runs following the process due to more consistent packing pressures that can be applied with an instrument rather than a small manual press or even pressing the die assembly with one’s hands.

CAPAD runs for all samples in this work were run by applying 2.5 V at t=0 seconds and applying 100 MPa load over a 180 second period. Temperature was commanded to the system using a custom LabView VI program, and the voltage was increased by 0.125 V every 15 seconds until approaching the desired holding temperature. To prevent overshooting the desired hold temperature, the voltage applied was systematically decreased in increments of 0.05 V beginning 100°C before the desired temperature. This decreasing process occurred over three to four separate steps depending on the desired processing temperature, where higher hold temperatures typically required more decreasing steps. This systematic decrease in applied voltages prevented overshooting the processing temperatures, and allowed for consistent densification runs in CAPAD across many samples. The processing temperature was held by adjusting the supplied voltage in increments of 0.01 V to maintain a hold temperature within ±

3°C. Typical current values during runs were 1350-1450 Amps. Hold times were typically 600 seconds, with an occasional sample being held for 1200 seconds. At the end of the hold time, the voltage was decreased by 0.125 V every 1 second to prevent a rapid change in voltage to the power supply. The system was allowed to cool under full uniaxial load until the optical pyrometer value reached 900°C, at which point the 100 MPa load was released over the course of 180 seconds. This consistent process of ramping and cooling provided consistent results across the samples presented in this work.

2.2.3. Density Measurements

Densities of samples were calculated using the Archimedes method, or a difference in mass of a sample dry and wet, relative to the dry mass. A MT-104 (Mettler Toledo, USA) scale was used to measure both the dry and wet mass of the samples, while a thermometer was placed into the water to record the water temperature. For each sample, the water temperature was recorded to account for the temperature dependent density of the water. Densities of samples were calculated using five separate measurements of both the wet and dry masses of each sample, to have a more accurate estimate of the density. **Equation 2.1** was used to calculate the density of each sample, where ρ represents the density and m represents the mass. Relative densities were calculated with respect to the density of Al_2O_3.

$$\frac{\rho_{sample}}{\rho_{fluid}} = \frac{m_{sample_{dry}}}{m_{sample_{dry}} - m_{sample_{wet}}} \quad \text{(Eq. 2.1)}$$

2.2.4. Polishing

When a densified sample was removed from CAPAD, there were a few steps required to prepare them for material characterization. First, the majority of the graphite foil sheets were removed from the two circular planar surfaces using a sharp blade. The circumferential edge had proven too difficult to remove the graphite foil with just a blade, but was polished off as required. Typical samples left the small amount of graphite on the edge but it has no impact on characterization techniques used, i.e. in-line transmission, XRD, etc. There was a slight "crown" on the circumferential edges of the sample which were ground down with silicon carbide grinding disk at ~150 RPM.

Once the sample had the "crown" removed, it was placed flat on a 40 μm resin bonded diamond grinding disk (Allied High Tech Products Inc., USA) at ~200 RPM and used water as a lubricant. The 40 μm pad was used to even out the surfaces and get rid of the majority of the pits that arise from the graphite foil. Once relatively flat, graphite free, and pit-free, the sample was polished using successively smaller diamond polishing suspensions (Allied High Tech Products Inc. and PACE Technologies, USA) between 250-300 RPM and used PurpleLube (Allied High Tech Products Inc., USA) as a lubricant. The sizes of diamond suspension used continued through 30 μm, 15 μm, 9 μm, 6 μm, 3 μm, 1 μm, and 0.5 μm. The final polishing step used SIAMAT 2 Colloidal Silica (PACE Technologies, USA) with 20 nm silica suspension between 150-200 RPM. UHP water was used as a lubricant for colloidal silica polishing. All hazardous polishing waste was disposed of per university hazardous waste guidelines.

2.2.5. Microstructural and Optical Property Characterization

Microstructural characterization of both powders and bulk material surfaces were conducted using a Zeiss Sigma 500 Scanning Electron Microscope (Zeiss, Germany).

The primary optical method of measurement for all samples presented in this work was in-line transmission. An Agilent Cary 5000 (Agilent Technologies, USA) UV-Vis-NIR spectrophotometer was used to measure the transmission of samples. This system used multiple lamp sources to produce wavelengths of light from 175 nm to 3300 nm, and used a dual beam sample chamber to increase the accuracy and reproducibility of the measurement. The wavelength range measured for this work was 200 nm to 2500 nm. Prior to each measurement, the system was baselined using only the solid sample apertures to account for system and environmental variations, and then a single crystal sapphire reference was measured to ensure the system performance was within specifications per batch of measurements. For this work, only the small (ϕ1 mm) and medium (ϕ3 mm) solid sample holder apertures were used when measuring the bulk samples.

Photoluminescence and photoluminescent lifetime measurements were conducted using Horiba Fluorolog-QM with an InGaAs solid state detector (Horiba, Canada). The setup used a 980nm diode pumped solid state laser in continuous mode for measuring emission spectra, and in pulsed mode for lifetime measurements. Photoluminescence emission intensity was measured as a function of wavelength from 1000 nm to 1200 nm, and the lifetime was measured at a wavelength of 1030 nm.

2.3. Results and Discussion

2.3.1. Undoped Alumina

An initial study was conducted to determine the optimal densification conditions for the undoped TM-DAR powder. Multiple bulk samples were densified using CAPAD, polished, and measured to compare their in-line transmission as a function of wavelength. The densification temperatures ranged from 1165°C to 1265°C, and all samples were held for 600 seconds at 100 MPa. The in-line transmission measurements of these samples can be seen in **Figure 2.3**.

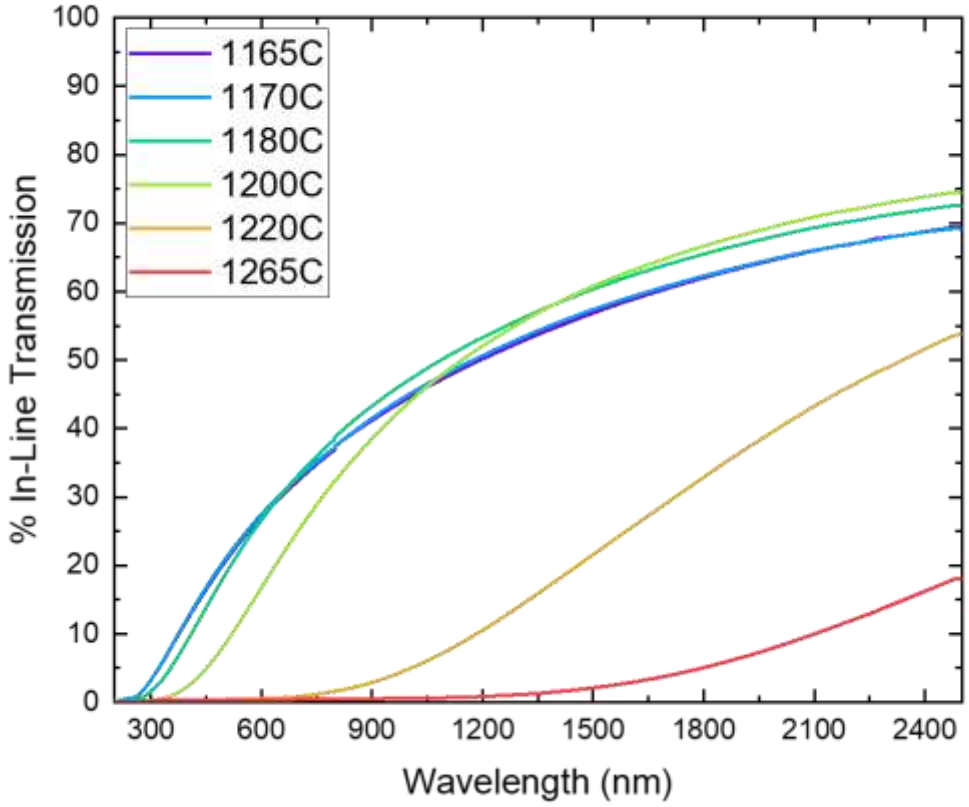

Figure 2.3: % In-Line Transmission vs. Wavelength of Undoped TM-DAR Samples

A stark contrast between samples densified under 1200°C and those above is clearly seen. To demonstrate this clearly, **Figure 2.4** shows three samples densified at 1165°C, 1220°C,

and 1265°C, or +55°C and +100°C from the lower temperature that produces relatively transparent samples. The ability to read through the samples is clearly described in the inset backlit photograph where an increase in densification temperature makes the sample move from transparency to translucency. This demonstrates that increasing densification temperature 50-100°C above an optimal condition will result in the loss of transparency and transmission in the wavelengths of interest for laser host materials.

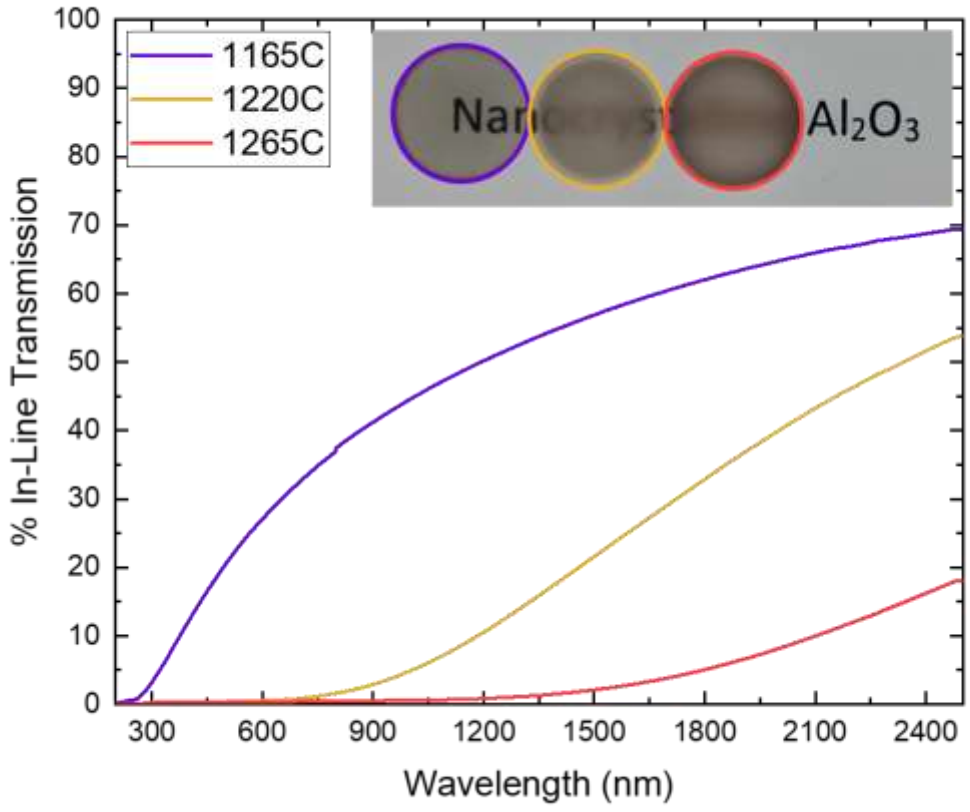

Figure 2.4: % In-Line Transmission of Undoped Samples, Temperature Sweep of 1165°C, 1220°C, and 1265°C, Inset of Backlit Photograph of Samples on a Transparency with Text Printed on It

What is a more difficult to make out is that below 1200°C there is a grouping of two samples that are lower in the higher wavelengths, higher in the lower wavelengths, and two that are the opposite. The in-line transmission of those four samples specifically are shown in **Figure 2.5** with an inset backlit photograph of the samples themselves.

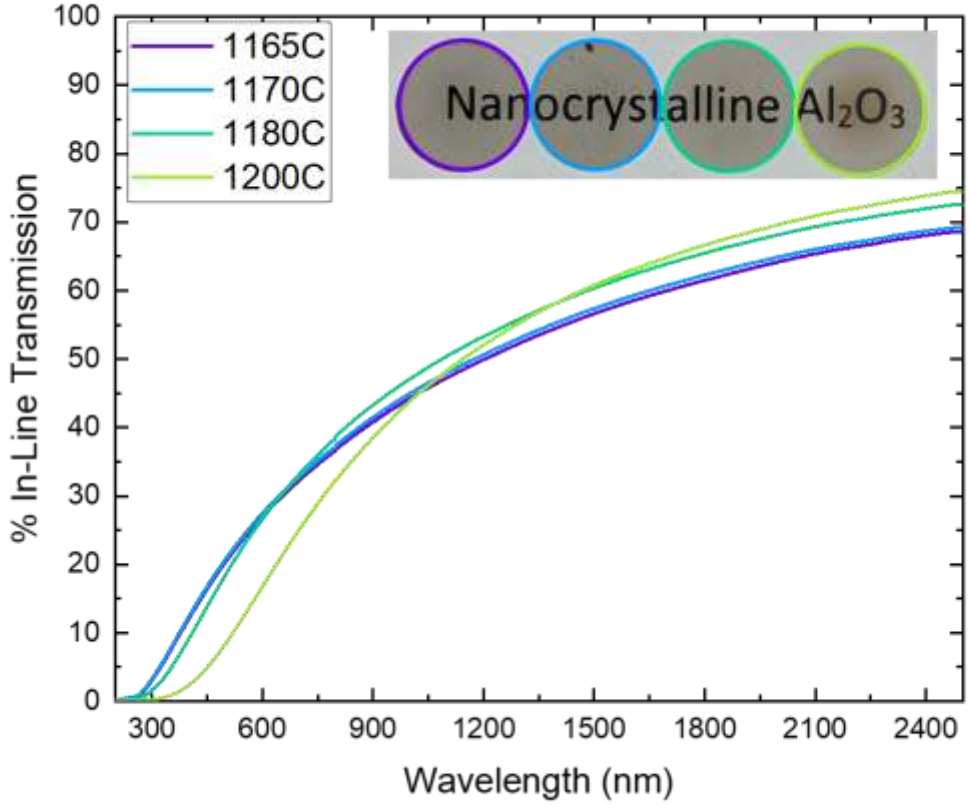

Figure 2.5: % In-Line Transmission of Undoped Samples, Temperature sweep of 1165°C, 1170°C 1180°C, and 1200°C, Inset of Backlit Photograph of Samples on a Transparency with Text Printed on It

Looking at these four samples, it is clear that there is a difference in optical behavior, and the inset photograph in **Figure 2.5** shows some discoloration in the center of the sample densified at 1200°C. Note that all four samples are still transparent enough to read through the ~1 mm thick bulk ceramic, while being densified at significantly lower temperatures than

traditional free sintering or HIP processes. This is attributed to grain growth in the center of the samples at higher densification temperatures causing more birefringent behavior. Because these samples appear to have consistently higher transmission at higher wavelengths, it can be closely tied to RGD scattering or a λ^{-2} behavior highlighting that birefringence scattering is the primary defect to address [2]. The opposite can be said about the lower temperature samples, in that they appear to be more consistent in the transmission behavior across all wavelengths, loosely connecting the scattering mechanism to Rayleigh scattering or a λ^{-4} behavior and highlighting that pores are the primary remaining defect to address [2]. Similar comparisons will be used for samples throughout this work, and be tied to this behavior that was observed in the undoped samples. **Figure 2.6** is two plots the logarithm of in-line transmission vs. wavelength raised to the -2 and -4 power respectively, to better illustrate this difference of behavior. Higher densification temperatures appear more linear in the λ^{-2} plot, while lower densification temperatures remain fairly linear in the λ^{-4} plot.

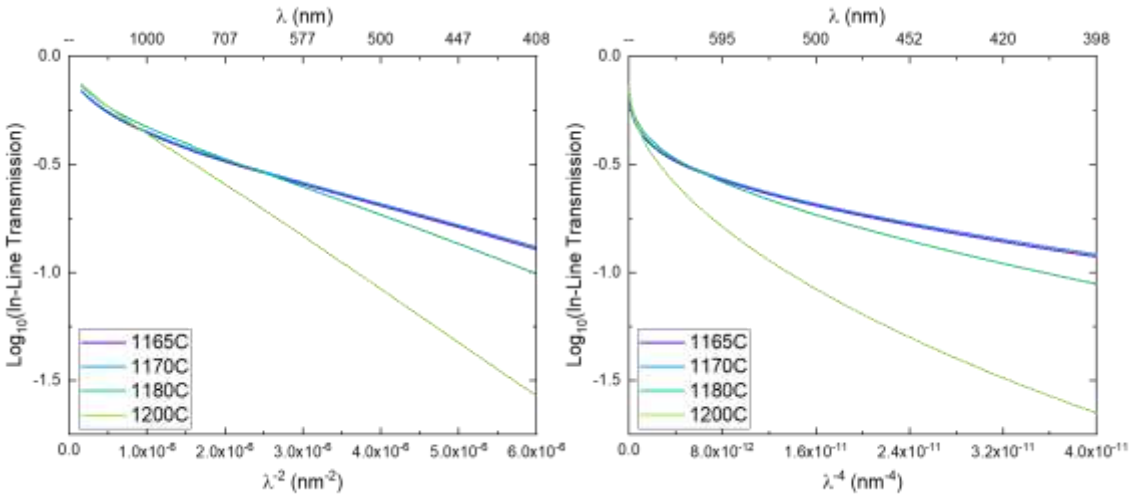

Figure 2.6: Undoped TM-DAR Samples, (Left) In-Line Transmission Plotted in Log Scale vs. λ^{-2}, (Right) In-Line Transmission Potted in Log Scale vs. λ^{-4}

Densities of these four lower temperature samples were measured using the Archimedes method described previously, and are plotted in **Figure 2.7**.

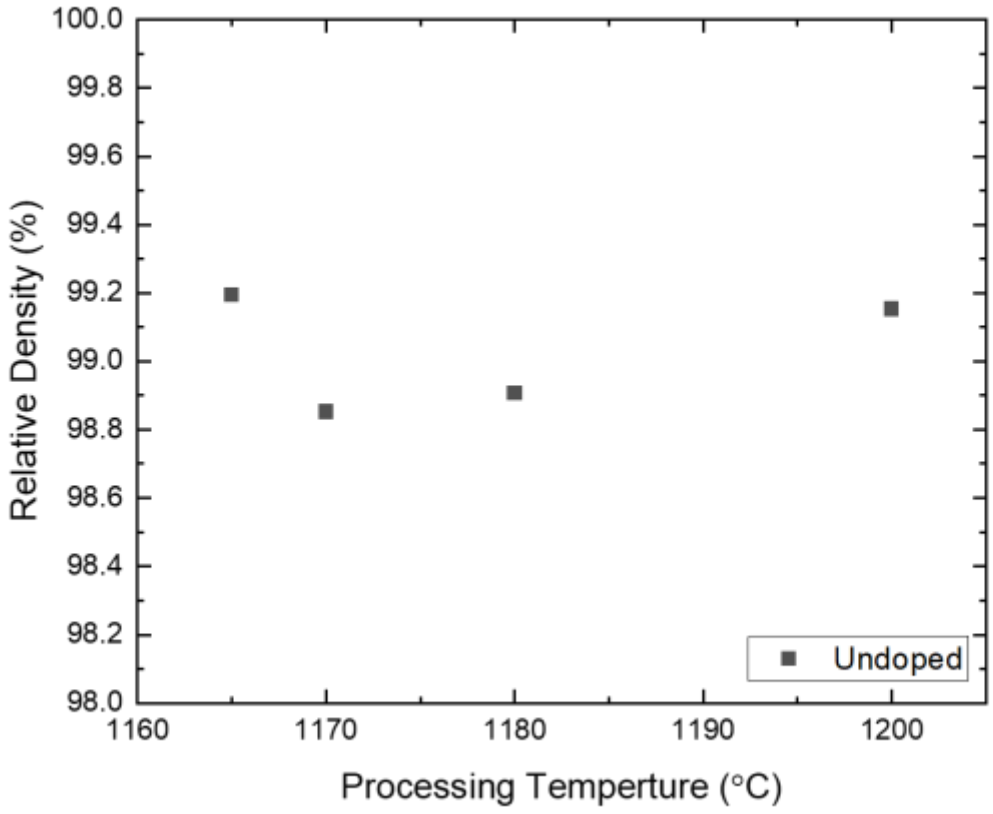

Figure 2.7: Relative Density vs. Processing Temperature of Undoped TM-DAR Samples

All four of these samples are above 98% relative density, with respect to a single crystal sapphire or alumina (Al_2O_3), which would be considered full density in many contexts (traditional metals, ceramics, etc.). Densifying at 1165°C and 1200°C the samples appear to have similar densities around 99.1%. Due to the apparent grain growth and loss of transparency when densifying at 1200°C, densification at a lower temperature is preferred to limit grain growth and have a small amount of residual closed porosity.

With all of these undoped samples densified and optically characterized, the ideal undoped densification conditions selected were a densification hold temperature of 1165°C, held for 600 seconds, with a 100 MPa load. These conditions produced a repeatable, transparent ceramic that was near 99% relative density when measured with the Archimedes method.

2.3.2. Rare-Earth Doped Alumina

Rare-earth doped TM-DAR was produced following the detailed procedures described in Section 2.2.1. The TM-DAR, Sigma-Aldrich Yb_2O_3 rare-earth oxide dopant powder, and the 0.25 at. % Yb:TM-DAR mixed powder were investigated using the Zeiss Sigma 500 Scanning Electron Microscope (SEM). Representative micrographs of the three powders are shown in **Figure 2.8**.

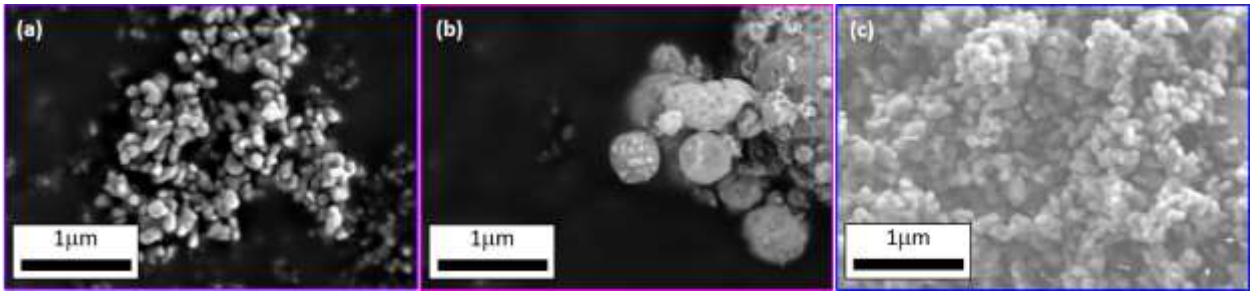

Figure 2.8: SEM Micrographs of Powders, (a) TM-DAR, (b) Sigma-Aldrich Yb_2O_3, (c) 0.25 at. % Yb:TM-DAR

Figure 2.8(a) shows a small agglomeration of unsieved TM-DAR powder. This powder is between 200-300 nm in crystallite size, and is similarly sized to the rare-earth oxide dopant powder. This nanopowder is what enables the fabrication of highly transparent and dense polycrystalline ceramics.

It is worth noting that the rare-earth oxide powder was listed as a nanopowder, but it is easy to see in **Figure 2.8**(b) that some agglomerates or particles are larger than 1μm in diameter. Processing of these larger particles and agglomerates was investigated, and it was determined that the powder can be broken down into smaller pieces with more time spent in the initial mortar and pestle mixing step of the process. The ~300 μm diameter spheres were not as easy to be broken up like the larger powders, but they were of the same order of magnitude as the TM-DAR powder they were mixed into.

Figure 2.8(c) shows that the morphology of the unsieved mixed 0.25 at. % Yb:TM-DAR powder. The TM-DAR powder remains unchanged through the mixing steps, and the crystallites remain extremely uniform in size.

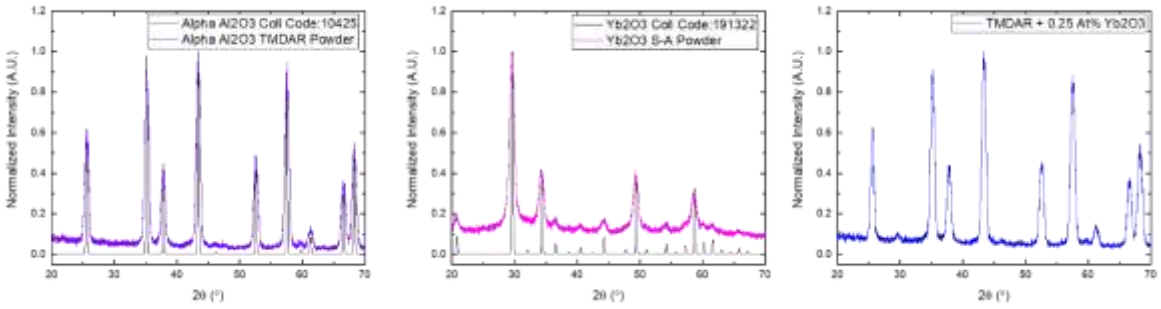

Figure 2.9: X-Ray Diffraction Measurements of Powders Compared with ICSD References, (Left) TM-DAR, (Middle) Yb_2O_3, (Right) 0.25 at. % Yb:TM-DAR Mixed Powder

To verify the phase purity of the powders, X-Ray Diffraction (XRD) measurements were taken from 20-70°, 2θ. The XRD measurements show good agreement with their ICSD references in **Figure 2.9**, and the 100% peak of the Yb_2O_3 can be seen in the mixed powder XRD at ~30°, 2θ. This makes sense because the amount of rare-earth oxide dopant mixed in is low, but has a smaller contribution to the reflections than that of the alumina.

The rare-earth oxide and TM-DAR powders were mixed following three processes. All three processes followed the mortar and pestle mixing, and were dried and sieved prior to densification. Powder Process 1 used low-energy ball milling (wet) and high-energy ball milling (wet) to mix the powder. Powder Process 2 used low-energy ball milling (wet) as the only mixing step. Powder Process 3 used high-energy ball milling (wet) as the only mixing step. **Table 2.** is provided to quickly break down the three processes and color code them for the following results.

Table 2.1: Rare-Earth Oxide Mixed Powder Processes

	Mortar & Pestle	Low-Energy Ball Mill	High-Energy Ball Mill	Dry	Sieve
Powder Process 1 (P1)	X	X	X	X	X
Powder Process 2 (P2)	X	X		X	X
Powder Process 3 (P3)	X		X	X	X

Each of these three powders were processed in CAPAD to fabricate bulk rare-earth doped ceramics. Once densified, the bulk samples were characterized to using XRD and compared with the powder XRD measurements. The left plot of **Figure 2.10** shows the Yb_2O_3 peak that was pointed out previously near 30°, 2θ. The right plot which is the XRD measurements of the bulk samples shows that the peak has been removed. This is clear evidence that the Yb^{3+} has been incorporated into the bulk ceramic, and we have successfully doped the material.

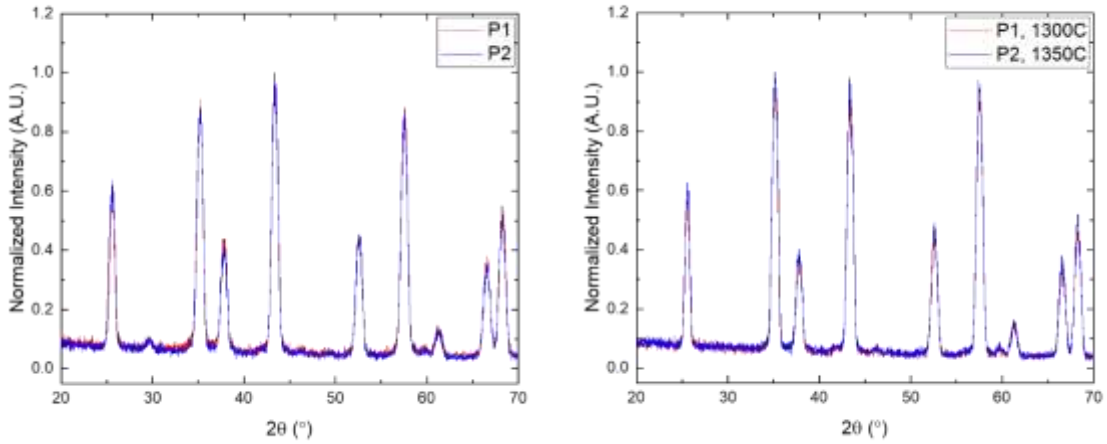

Figure 2.10: (Left) XRD Measurements of Powders mixed with Powder Process 1 and Powder Process 2, (Right) XRD Measurements of Bulk Samples Using Powder Processes 1 and Powder Process 2

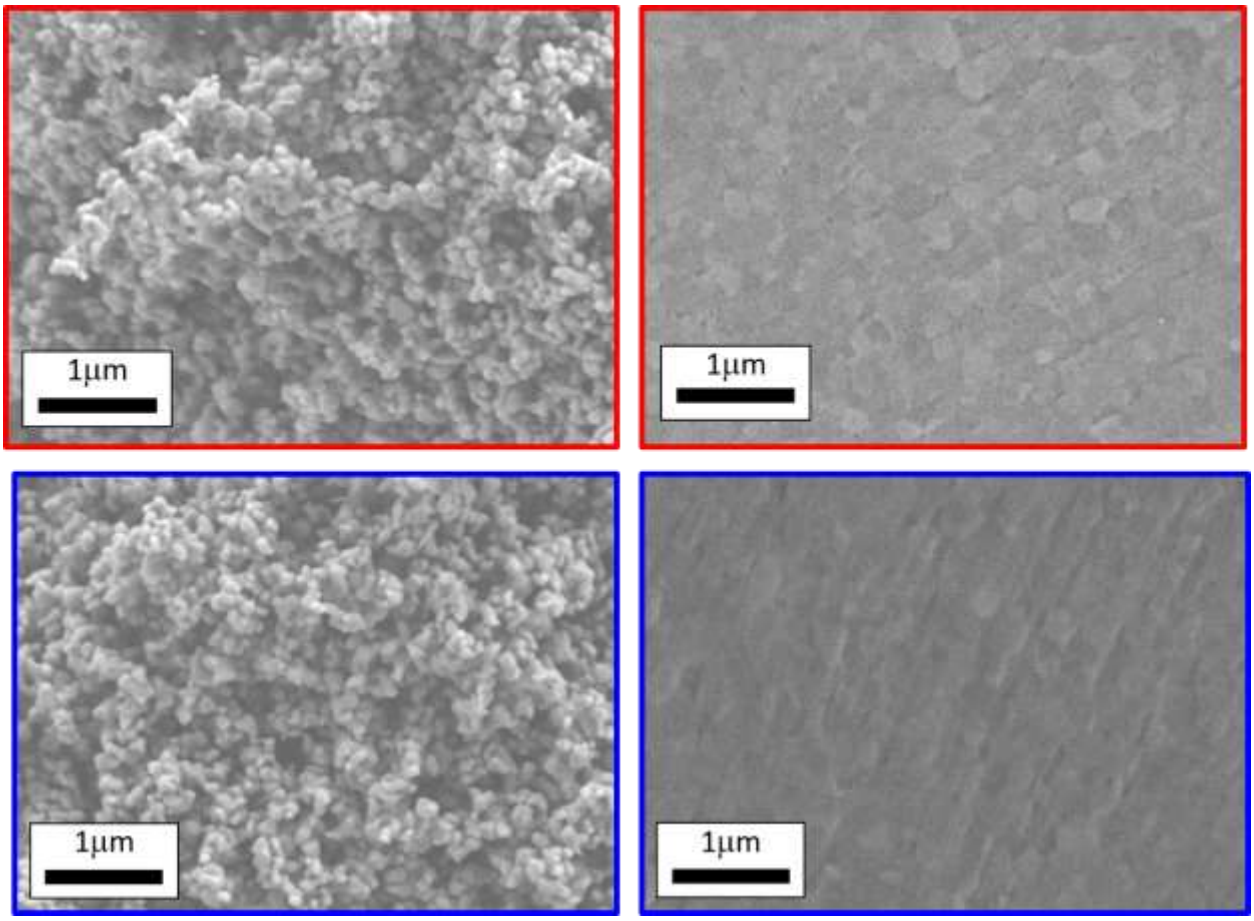

Figure 2.11: Powder and Bulk SEM Micrographs, (a) Powder Process 1 Powder, (b) Powder Process 1 Bulk, (c) Powder Process 2 Powder, (d) Powder Process 2 Bulk

In addition to XRD, the powders and bulk ceramics were compared with Scanning Electron Microscopy. Bulk samples were polished following the polishing procedures shared previously, and both powder and bulk samples were placed on SEM tabs using carbon tape. **Figure 2.11** shows powder and bulk SEM micrographs of Powder Process 1 and Powder Process 2. What is notable is that the grain size has not grown significantly, and is still near the 200-300 nm grain size. There was no sign of secondary phases or rare-earth segregation in these bulk samples when observed under SEM, which is another sign that there was successful incorporation of the Yb^{3+} into the bulk ceramic.

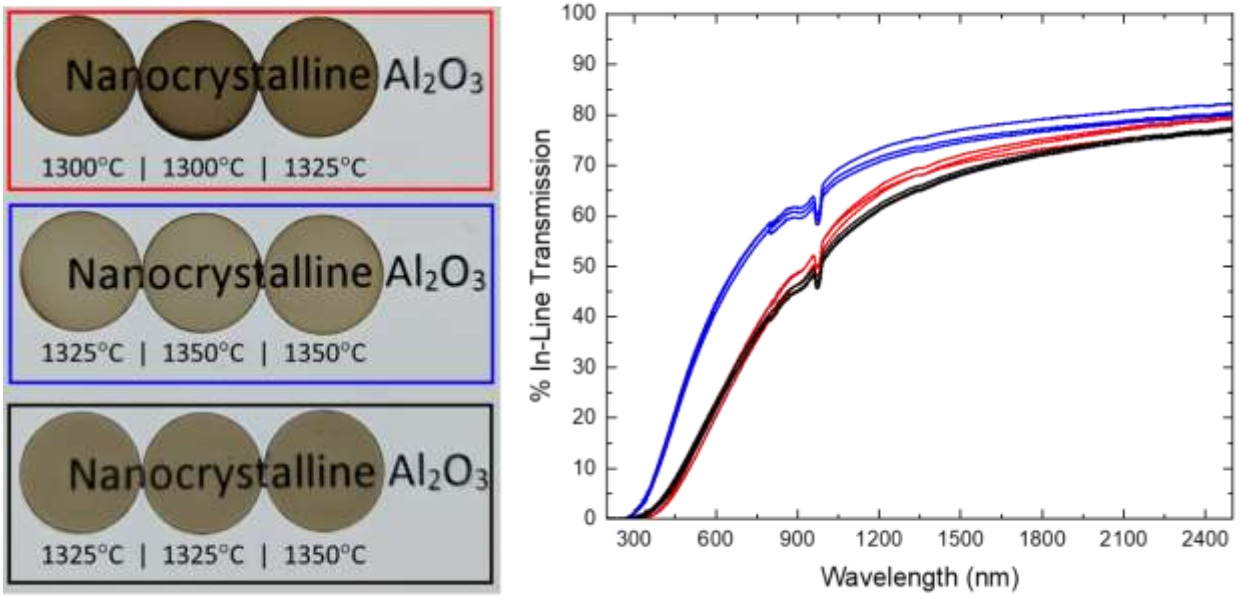

Figure 2.12: (Left) Backlit Photograph of Bulk 0.25 at. % Yb:TM-DAR Samples, (Right) % In-Line Transmission Measurements of All 9 Yb Doped Samples Shown on the Left

The left image in **Figure 2.12** shows a photograph of three samples densified for each powder process. Each set of 3 samples is densified within 25°C of the set, with the whole set of 9 samples being densified between 1300 and 1350°C. Similar to the undoped samples, these

densification processing temperatures are significantly lower than comparable Yb doped samples shared in Chapter 1 and processed either with free sintering, vacuum sintering, HIP, or a combination of the processes. The characteristic absorption of Yb^{3+} is seen in all samples at 940 nm (broad) and 976 nm (deep), further confirming that the rare-earth dopant ions were incorporated into the bulk material. It is clearly seen in both the photograph and the in-line transmission measurements that Powder Process 2 produces more transparent samples. For each of these processes, one sample was densified at a lower temperature in an attempt to have opaque samples for each. The densities for all of these samples were measured using the Archimedes method and their relative densities are plotted in **Figure 2.13**. Near full densities were achieved at processing temperatures significantly lower than more conventional densification processes.

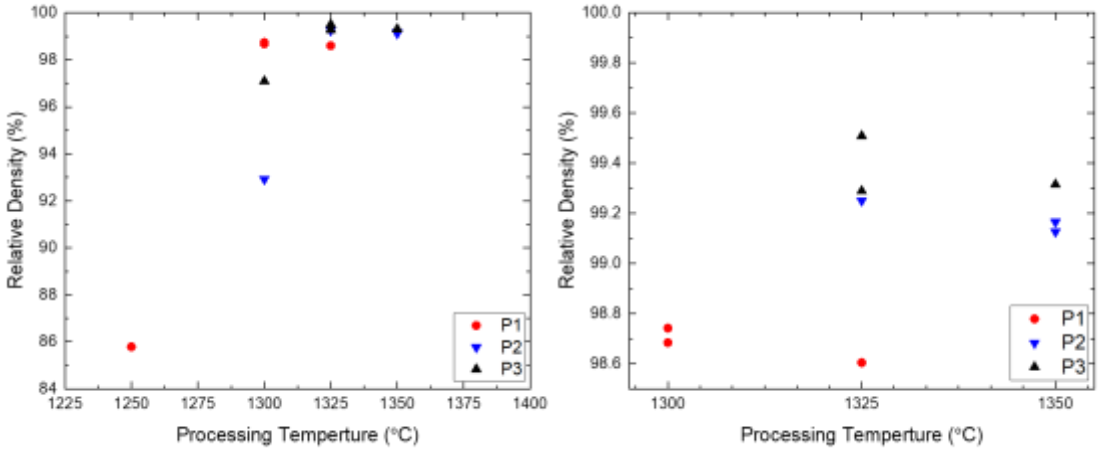

Figure 2.13: Relative Densities of Bulk 0.25 at. % Yb:TM-DAR Samples vs. Processing Temperature, (Left) Including Opaque Samples, (Right) Magnification of the Left Plot Showing the 9 Transparent Samples

Similarly to the undoped samples, there is difference in the wavelength dependent behavior of the in-line transmission measurement. Powder Process 1 and Powder Process 3 both have more of a RGD scattering behavior, or λ^{-4} dependence, while Powder Process 2 has more of

a Rayleigh scattering behavior, or λ^{-2} dependence. Note that in Powder Processes 1 and 3 they both have high-energy ball milling steps, which is believed to be the cause of the darkening of samples through contamination released by the dopant powder and captured in the powder agglomerates. Similar to the undoped samples, the transmission of the best samples for each powder process were plotted on a logarithmic scale for the in-line transmission vs. the wavelength raised to the -2 and -4 power in **Figure 2.14**.

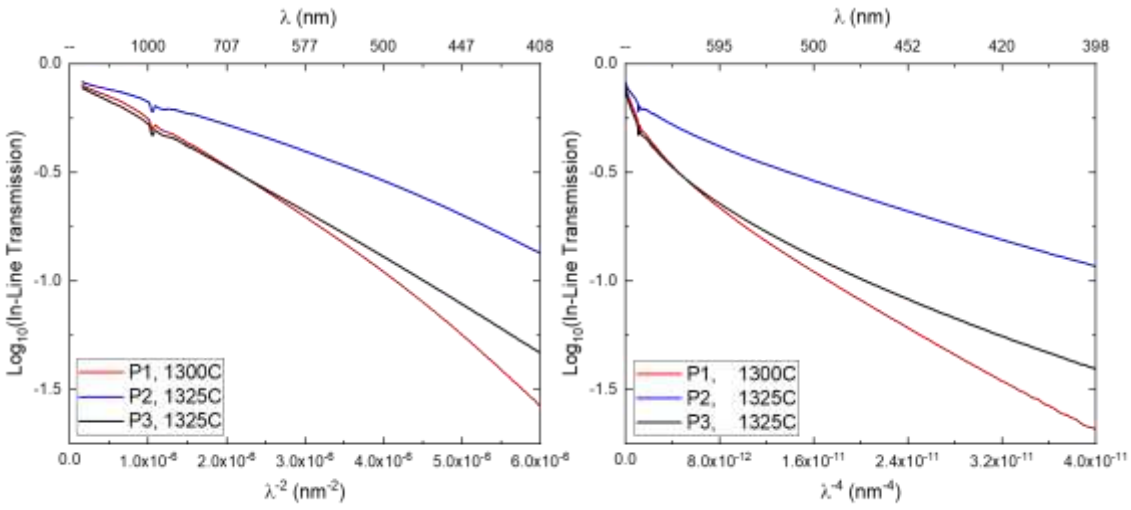

Figure 2.14: Best Samples of Each Powder Processing Condition, (Left) In-Line Transmission plotted in log scale vs. λ^{-2}, (Right) In-Line Transmission plotted in log scale vs. λ^{-4}

Building upon the work conducted with rare-earth oxide as a dopant source, parallel work with other dopants in the lab showed promise of using rare-earth nitrates as dopant sources. In exploring this new source, a few adjustments to the powder processing were made and are quickly shown in **Table 2.2** with color coordination again. Because the nitrate is a water stabilized crystal, all processing occurred dry, and special care was taken in keeping the powder from being exposed to open air longer than absolutely necessary. Mortar and pestle steps, as

well as sieving occurred in the clean box environment, and the high-energy ball milling step was when the powder was exposed to open air the most. Because all processes occurred dry, there was no need to vacuum dry any powders processed following the Powder Processes 4 methods. For this work, two batches of Powder Process 4 were produced, and are further referred to as P4.1 and P4.2 to identify which batch the samples originated from.

Table 2.2: Rare-Earth Nitrate Mixed Powder Process

	Mortar & Pestle	Low-Energy Ball Mill	High-Energy Ball Mill	Dry	Sieve
Powder Process 4 (P4)	X		X		X

Powder Process 4, batch 1 (P4.1) was densified with a temperature sweep in 25°C increments. This allowed for fast learning of the optimal conditions. Based off of initial in-line transmission measurements from those four samples, the densification temperature window as found to be between 1300°C and 1325°C. This is similar to the optimal conditions for rare-earth oxide doped bulk ceramics as well. It is worth noting that the Powder Process 4 bulk samples looked much more transparent, and had less darkening than their rare-earth oxide doped counterparts.

Powder Process 4, batch 2 (P4.2) was densified with a temperature sweep in 10°C increments. This showed that the optimal conditions for rare-earth nitrate doped samples was near 1300°C, similar to the best samples from P4.2 and the rare-earth oxide doped samples.

Figure 2.15 is a backlit photograph with text printed on it of all rare-earth nitrate doped samples. Batch one is on top, while batch 2 is on the bottom. The P4.1 sample densified at 1300°C may look dark around the edges, but that is just the impact of the edge not being as fully

dense as the center of the sample. This sample specifically had the highest in-line transmission out of all of the P4.1 samples. P4.2 being a repeat of P4.1 shows that there is a slight area that may not be fully dense on the edge of the sample densified at 1300°C, but also was the sample with the highest in-line transmission out of the batch. Between P4.1 and P4.2, 1310°C and 1325°C looked the best optically in a photograph, but that densification temperature proved to not be the most transparent when measured with the spectrophotometer.

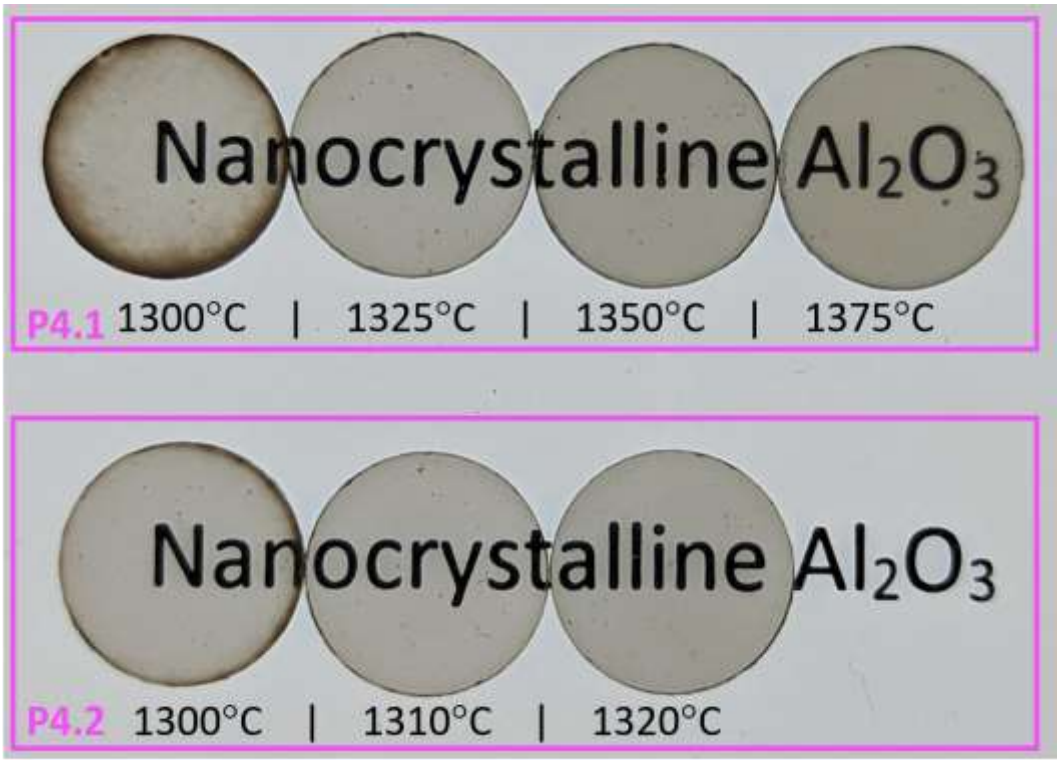

Figure 2.15: Backlit Photograph of Rare-Earth Nitrate Processed Samples on a Transparency with Text Printed on It, (Top) Powder Process 4.1 Samples, (Bottom) Powder Process 4.2 Samples

Densities for each of these rare-earth nitrate doped samples were measured and are plotted in **Figure 2.16**. Densities are slightly higher than the rare-earth oxide doped samples, but similarly near full density is achieved at relatively low processing temperatures.

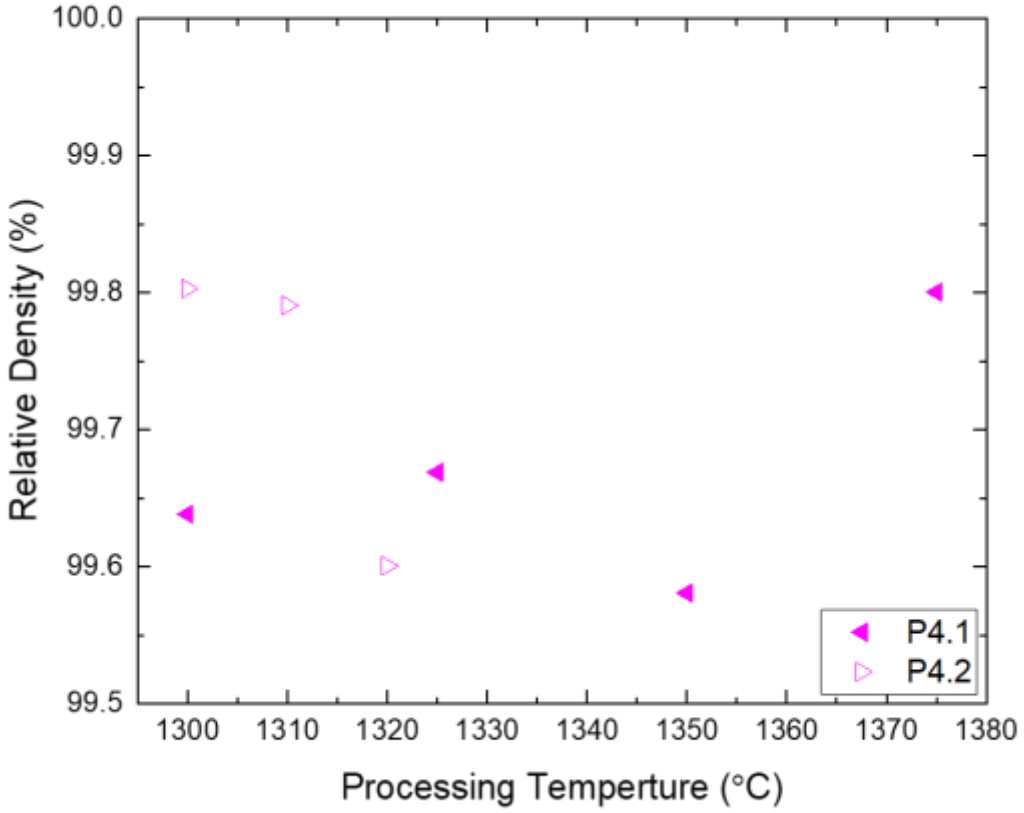

Figure 2.16: Relative Densities of Rare-Earth Nitrate Doped Samples vs. Processing Temperature

Comparing these improved samples to the best rare-earth oxide doped sample was the next step in the process. **Figure 2.17** shows on the left a backlit photograph on a transparency with text printed on it of a single crystal (SC) sapphire reference, the rare-earth nitrate doped samples (P4.1 and P4.2) and the best rare-earth oxide doped sample. On the right it has the measured in-line transmission of each sample for comparison. It is worth noting that the polycrystalline samples fabricated with CAPAD have lower transmission at lower wavelengths but are near the single crystal value at higher wavelengths. Again it is worth noting that all

doped samples show deep absorption at the wavelengths of interest, confirming that the Yb^{3+} is incorporated into the bulk ceramic material.

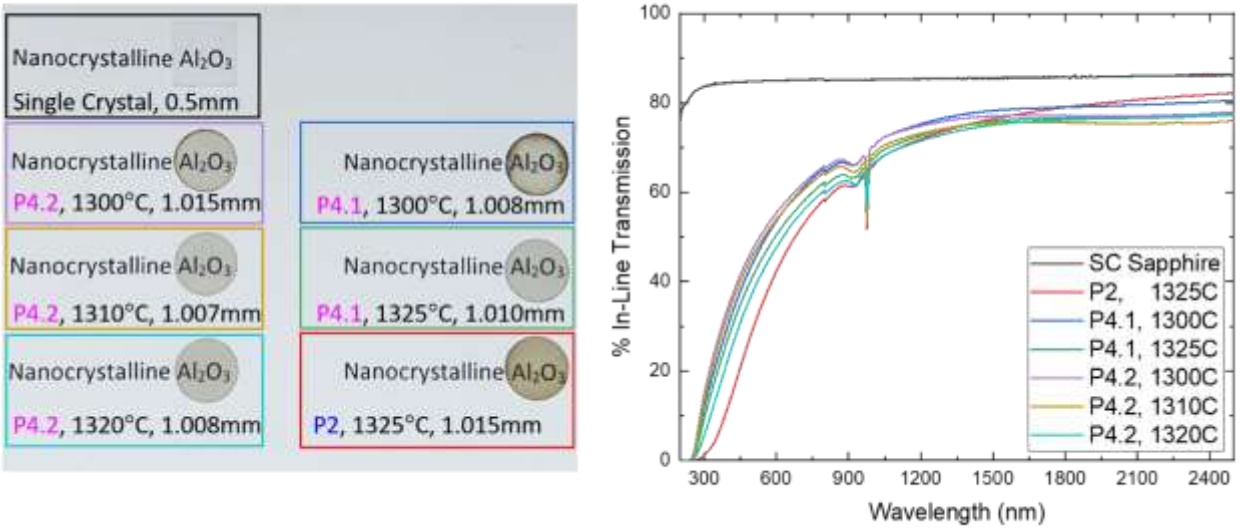

Figure 2.17: (Left) Backlit Photograph of Single Crystal Sapphire and Yb Doped Samples on a Transparency with Text Printed on It, (Right) % In-Line Transmission Measurements of Single Crystal Sapphire and Yb Doped Samples Shown on the Left

Note that the thickness for all samples is approximately 1 mm, with the exception of the single crystal sapphire reference being 0.5 mm thick. The nitrate samples show similar transmission behavior as a function of wavelength, and seem to only have decreasing in-line transmission as a function of densification temperature, the best samples overall were selected for further analysis, and are shown in **Figure 2.18**. This figure, on the right, shows the broad but shallow absorption centered near 940 nm and the sharp but deep absorption centered near 976 nm for all three samples. Note that the magnitude of the depth of all of the samples is similar, but for the rare-earth oxide doped samples the overall transmission is lower, causing the peak to look less deep.

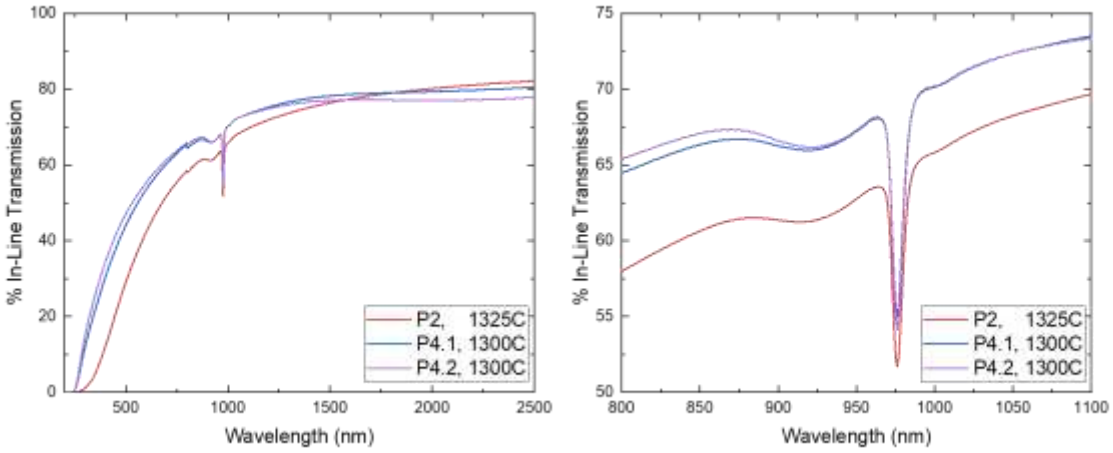

Figure 2.18: (Left) % In-Line Transmission Measurements of the Three Best Bulk Yb Doped Samples (Right) Magnification of the Left Plot around the Absorption Wavelengths of Interest

Looking at these three samples specifically, there is clearly a difference in the transmission behavior as a function of wavelength between the rare-earth oxide and rare-earth nitrate doped samples. To look deeper into this, **Figure 2.19** shows the logarithmic scaled transmission vs. the wavelength raised to the -2 and -4 power. Here it is clear that the rare-earth nitrate doped samples produced in Powder Process 4 (batch 1 and 2) are much more linear in the λ^{-2} plots, while the rare-earth oxide doped sample is near linear in the λ^{-4} plot. This means that the rare-earth nitrate doped samples are primarily impacted by pore, or Rayleigh scattering, while the rare-earth oxide doped sample is impacted more by birefringence, and RGD scattering. This is similar to what was shown previously with undoped and with the rare-earth oxide doped samples, where higher temperatures caused differences in the wavelength dependent behavior of the transmission.

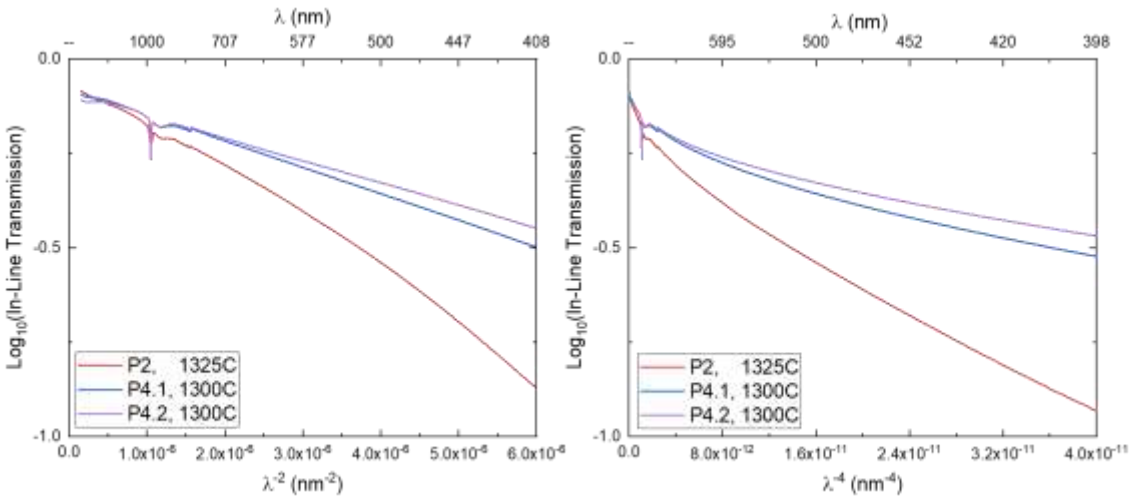

Figure 2.19: The Three Best Yb Doped Samples, (Left) In-Line Transmission plotted in log scale vs. λ^{-2}, (Right) In-Line Transmission plotted in log scale vs. λ^{-4}

A few steps are required to take the data from the in-line transmission measurements and present the absorption cross section for each sample. First the transmission data is converted from percentages to a decimal place for ease of subsequent calculations. The method employed for this work is to call all losses above a linear fit over the absorption peaks, the background. This assumption means that the background encompasses reflections and scattering losses. The reason for making this assumption is the difficulties in differentiating transmission losses due to absorption and scattering. By making this assumption, only the peaks below the background are considered for the absorption cross section, making it a fairly conservative method for determining the cross sections of these Ytterbium doped samples. **Figure 2.20** depicts the three best samples and also has the background line drawn for each. Note this background line is a liner fit between the measured data at 850nm and at 1050nm for each sample.

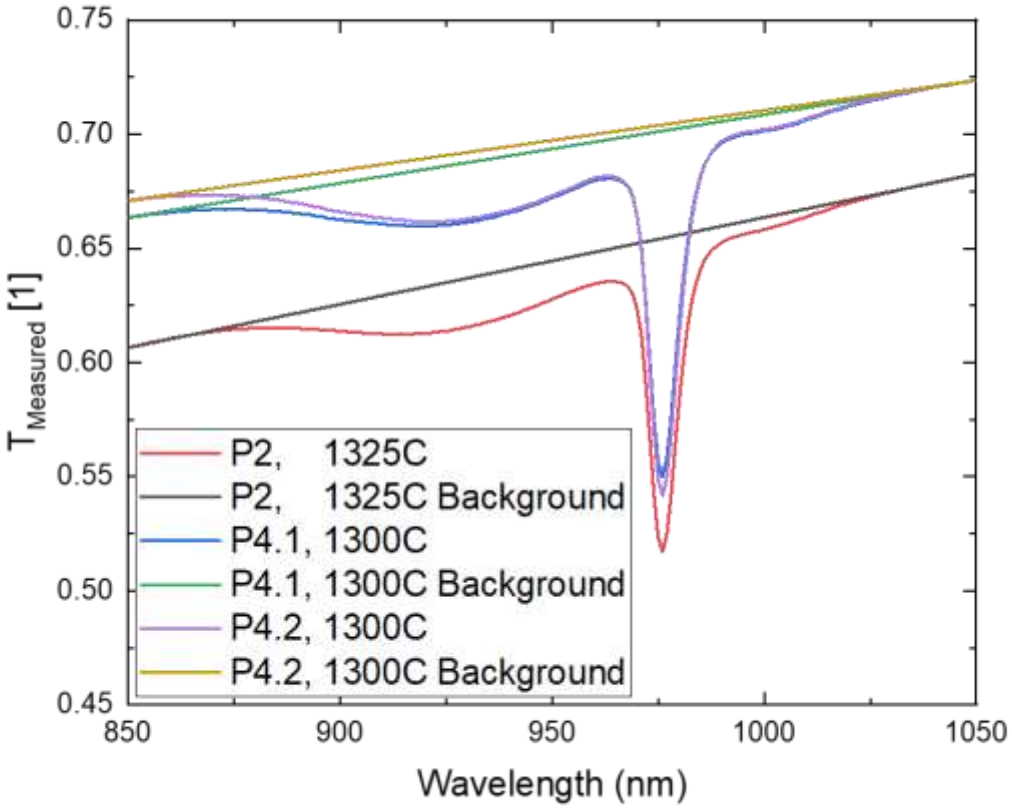

Figure 2.20: Transmission Measurements of the Three Best Yb Doped Samples with Background Loss Lines Drawn Across the Plotted Range

The measured transmission is then used to calculate the transmission losses due to absorption using **Equation 2.2**. This is a simple method of comparing the two, and produces an interpretable plot of the behavior of the samples that can be seen in **Figure 2.21**.

$$T_{Absorption} = \frac{Background}{T_{Measured}} \qquad \text{(Eq. 2.2)}$$

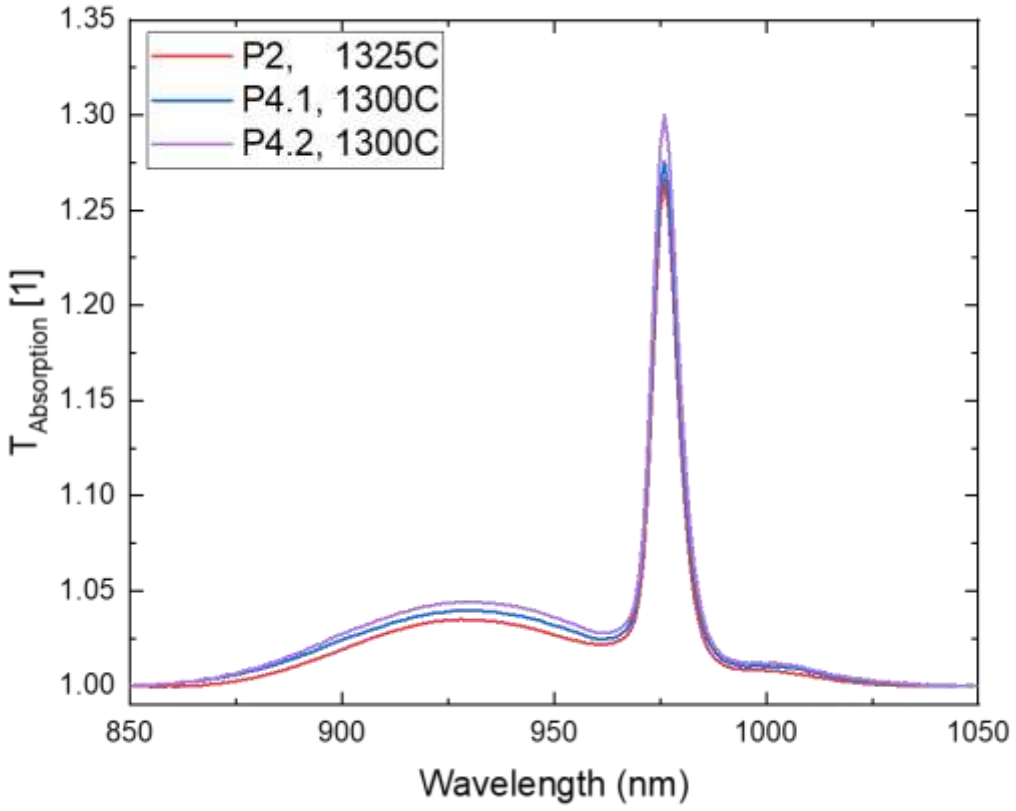

Figure 2.21: Absorption Transmission of the Three Best Yb Doped Samples

In order to extract the absorption coefficient, α from this transmission losses due to absorption, a simple Beer-Lambert relationship can be used and is written as **Equation 2.3**. Note that *l* is the thickness of the sample in this equation.

$$T_{Absorption} = e^{-\alpha l} \quad \text{(Eq. 2.3)}$$

Solving this equation for α, we get **Equation 2.4**.

$$\alpha = \frac{1}{l} ln[\frac{1}{T_{Absorption}}] \quad \text{(Eq. 2.4)}$$

Using the measured thicknesses of each sample, and the transmission loss due to absorption, the absorption coefficient is calculated and plotted in **Figure 2.22**. It is worth noting at this point that the rare-earth oxide doped sample from Powder Process 2 has a lower maximum coefficient than that of the rare-earth nitrate samples made with Powder Processes 4.1 and 4.2.

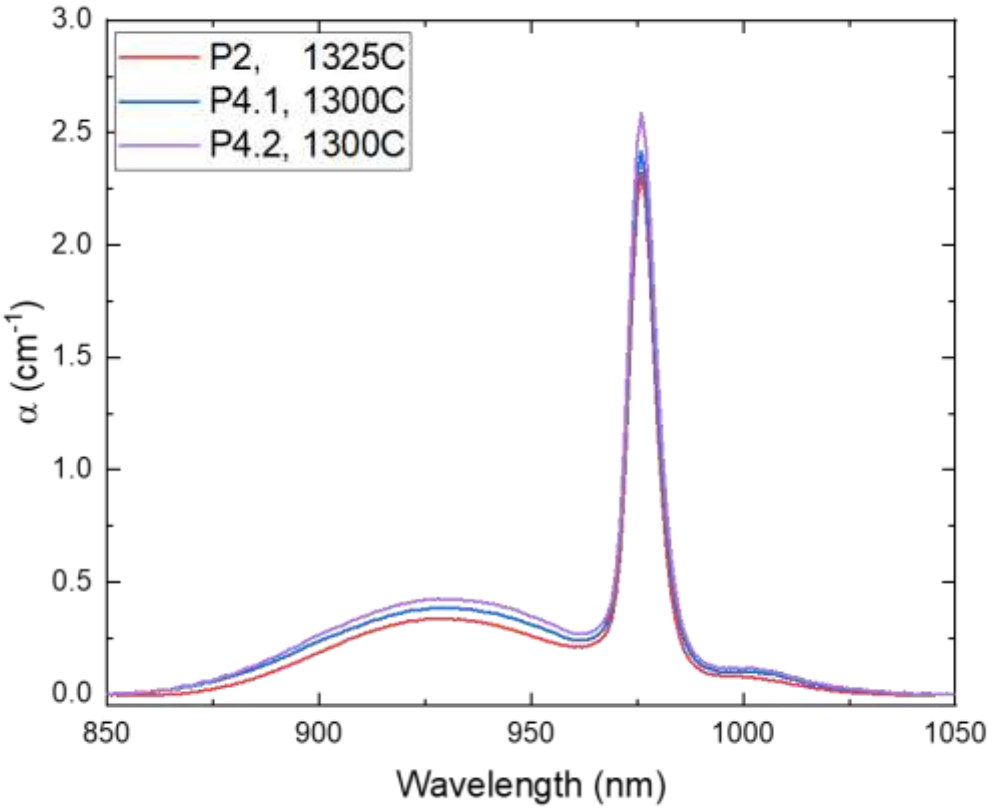

Figure 2.22: Absorption Coefficient of the Three Best Yb Doped Samples

The carrier concentration is calculated considering cation doping exclusively, and is shown in **Equation 2.5**.

$$N_{Yb:Al_2O_3,\ 0.25\%} = \frac{2 \cdot 3.987 g/cm^3}{\left(2 \cdot 26.9815 \ + \ 3 \cdot 15.999\right) \cdot 1.66 \times 10^{-24} g} \cdot 0.0025 \qquad \text{(Eq. 2.5)}$$

$$= 1.178 \times 10^{20}\ atoms/cm^3$$

The absorption cross section is then calculated by dividing the absorption coefficient by the dopant concentration shown in **Equation 2.6**.

$$\sigma_{Abs} = \frac{\alpha}{concentration} = \frac{\alpha}{1.178 \times 10^{20}\ atoms/cm^3} \qquad \text{(Eq. 2.6)}$$

Plotting the absorption cross sections for the three best Yb Doped samples in **Figure 2.23**, we can see that they are all quite similar in position, and in magnitude. Again noting the samples fabricated using rare-earth nitrate as the dopant source have a higher absorption cross section over the plotted range than that of the rare-earth oxide doped sample.

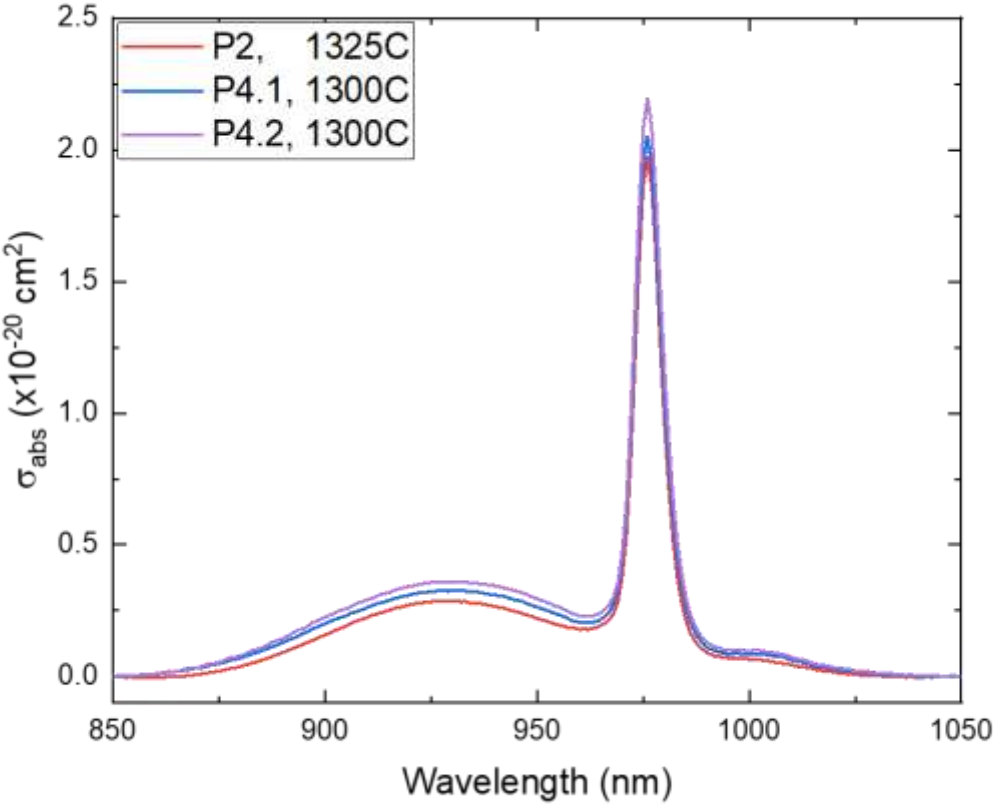

Figure 2.23: Absorption Cross Section of the Three Best Yb Doped Samples

To put these absorption cross sections into perspective, **Figure 2.24** was constructed using a few different Ytterbium doped laser host materials as comparisons. All three maximum values for absorption cross section from this work are higher than that of other host materials at 976 nm, including garnets and glasses. Having a large absorption cross section is great for pumping the material, but to have a successful laser gain material further investigation of the emission from the samples when excited near 976 nm is necessary.

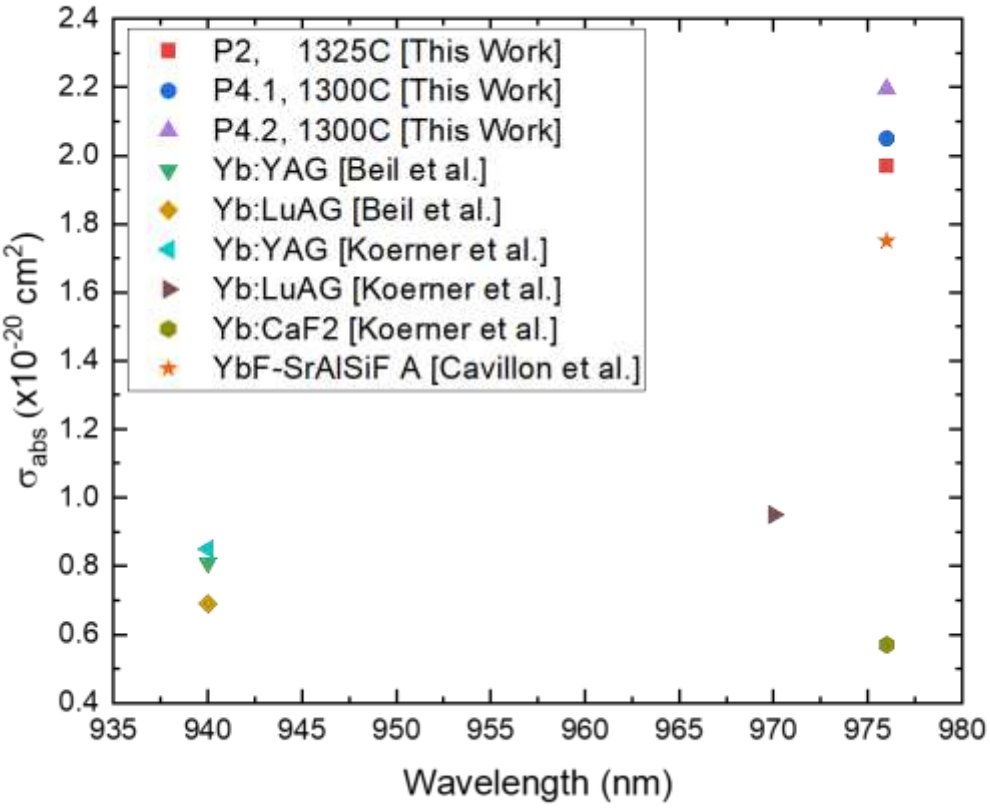

Figure 2.24: Absorption Cross Section Comparison of This Work with Literature Values of other Yb Doped Materials [3-5]

For the remaining results presented, only samples from P2 and P4.1 were able to be characterized enough to proceed, and P4.2 will not be further characterized in this work. For P2 and P4.1 samples, emission spectra was measured and the photoluminescent lifetime was fit to the measured data as described in Section 2.2.6. **Figure 2.25** shows the lifetime measurements of the two samples.

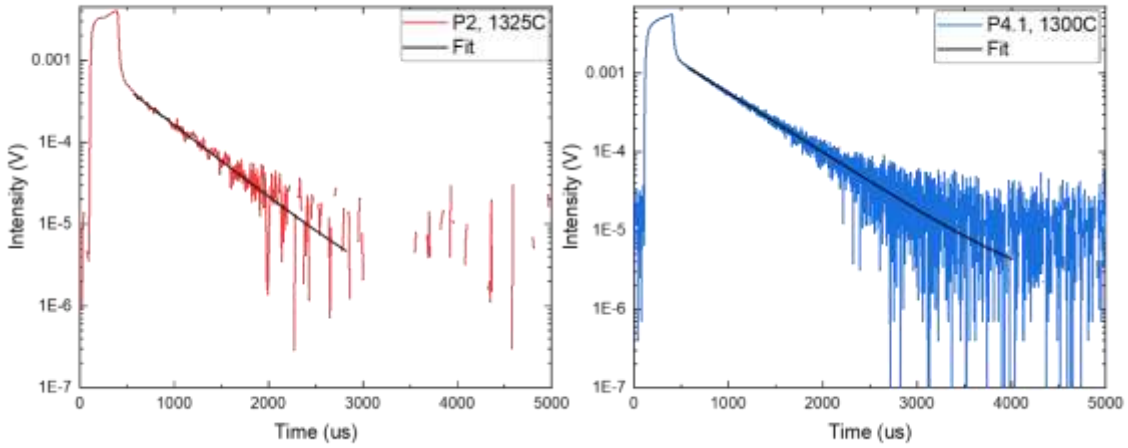

Figure 2.25: Intensity vs. Wavelength Measurements of Samples Excited with 980 nm and Measured Emission at 1030 nm with Fitted Curves to Determine Lifetime, (Left) Powder Process 2 Sample, (Right) Powder Process 4.1 Sample

Lifetime measurements of these samples are between 400-600 μs, which is in the middle of Nd:YAG (~200 μs [6]) and Yb:Glass (~1000 μs [5]), as reported in literature. Specifically or the Powder Process 2 Sample, the lifetime was measured to be 490.8 ± 7.30 μs, and for the Powder Process 4.1 sample, the lifetime was measured to be 573.21 ± 0.95 μs.

Emission intensity of each sample was measured at 1030 nm using a 980nm diode pumped laser in continuous mode as the excitation source. The emission was weaker in the rare-earth oxide doped sample, than in the rare-earth nitrate doped sample, but the emission peaks show good alignment between each sample when normalized. **Figure 2.26** shows the measured emission intensity vs. wavelength, raw on the left, and normalized on the right.

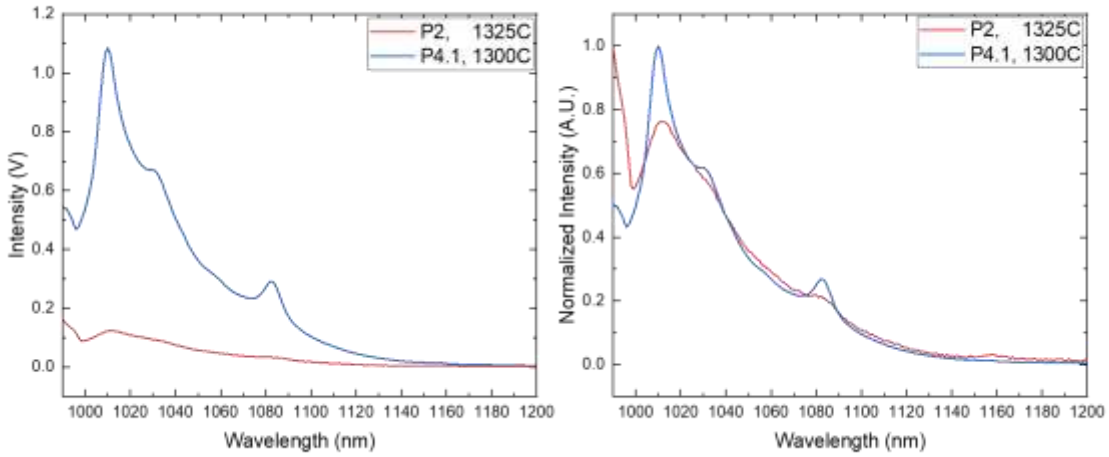

Figure 2.26: (Left) Emission Intensity vs Wavelength for Yb Doped Samples, (Right) Normalized Intensity vs. Wavelength for Yb Doped Samples

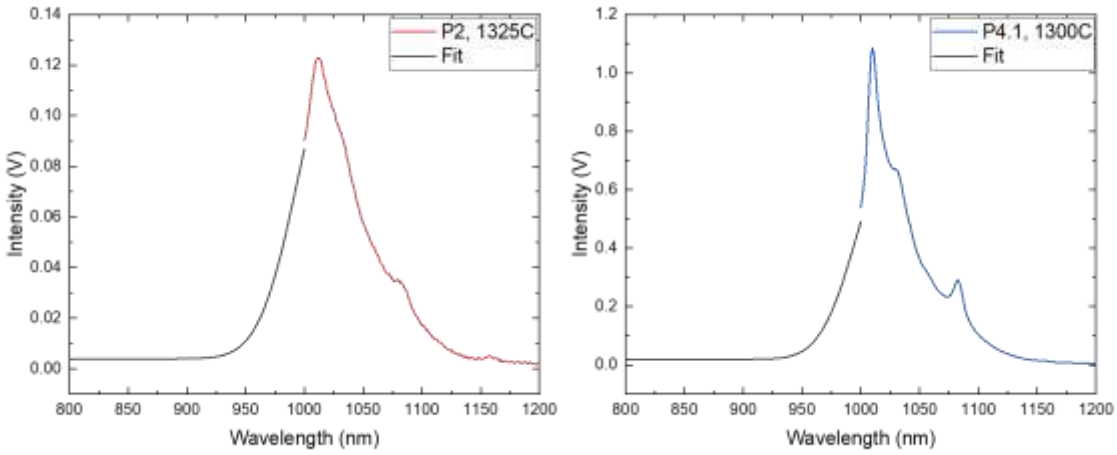

Figure 2.27: Gaussian Fitting of Truncated Plot of Emission Spectra of Yb Doped Samples, (Left) Powder Process 2 Sample, (Right) Powder Process 4.1 Sample

Note that due to the challenges measuring the emission so close to the excitation source (measuring 1030 nm emission near 980 nm excitation), a Gaussian fit to the measured data was used to fill data below 1000 nm, and increase the overall integral, so that we did not artificially

inflate the emission cross section by not incorporating a significant portion of the integral prior to the emission wavelength. The raw data was truncated from 1000 nm (only removing 10 data points) and then fit from 1010 nm to 1200 nm to match the breadth of the measured peak. This was then flipped across the 1010nm peak and plotted from 800 to 1000 nm. It is worth noting that some structure around 940 nm and/or around 980 nm would typically be expected in a measurement across the full range, but this Gaussian fit was used primarily to capture the breadth of the peak for further calculations. The fit curve can be seen in both plots of **Figure 2.27** in black, and these values were used when calculated the emission cross section for each sample.

Using the lifetime and emission measurements, in connection with the Füchtbauer-Landenberg method [7], the emission cross sections were calculated using **Equation 2.7**. In this equation η is the quantum efficiency, λ is the wavelength, $I(\lambda)$ is the measured intensity as a function of wavelength, τ_f is the measured lifetime, n is the index of refraction of the material, c is the speed of light. For Ytteribum, which does not generally see concentration quenching effects, especially at this low of a doping concentration, the quantum efficiency is assumed to be unity, which is a common assumption when using this method and used in Aull's paper [7].

$$\sigma_{em}(\lambda) = \frac{\eta\lambda^5}{\tau_f(\int \lambda I(\lambda)d\lambda)8\pi n^2 c} I(\lambda) \qquad \text{(Eq. 2.7)}$$

The emission of both samples can be seen in **Figure 2.28** and clearly shows that the rare-earth nitrate doped sample has higher emission than the rare-earth oxide doped sample. It is interesting to note that the maximum emission the peak for both samples is near 1010 nm when compared to the 1030 nm emission expected.

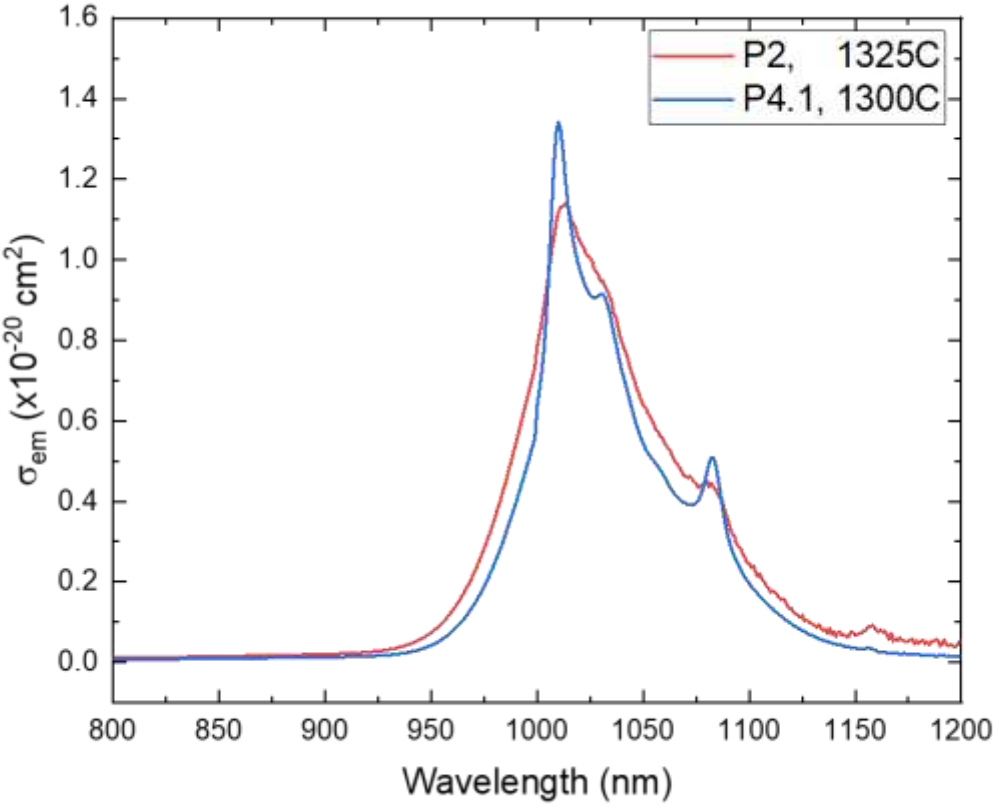

Figure 2.28: Emission Cross Sections of Yb Doped Samples

To put both the peak wavelength, and the maximum emission cross section values of this work in perspective, the following plot was constructed in a similar way to how the absorption cross section comparison was made. **Figure 2.29** describes multiple other laser host materials that are doped with Ytterbium. It is clear that the emission wavelength of samples fabricated in this work align more with Ytterbium doped glasses, than other garnets in literature. It is also notable that the emission cross sections magnitudes of this work are near the middle of the other work compared. This highlights that the doping and densification techniques used to fabricate these rare-earth doped polycrystalline samples behave more like doped glasses than doped single

crystals. The breadth of the emission is also similar to that of glasses, but the benefit of having a higher thermal conductivity host material is the ability to pump it significantly harder without failure of the material.

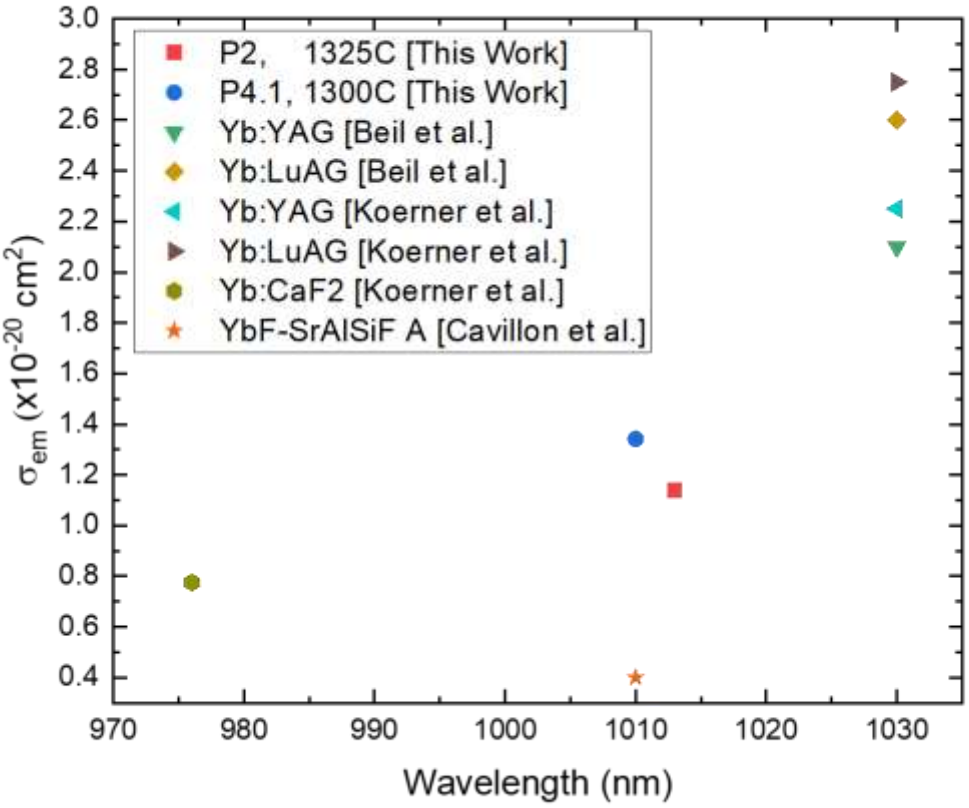

Figure 2.29: Emission Cross Section Comparison of This Work with Literature Values of other Yb Doped Materials [3-5]

Both the absorption and emission cross sections for the Powder Process 2 sample and the Powder Process 4.1 sample were plotted together in **Figure 2.30**. This figure shows how narrow but large the absorption is in the samples, while the emission is lower than expected but extremely broad as well for both samples.

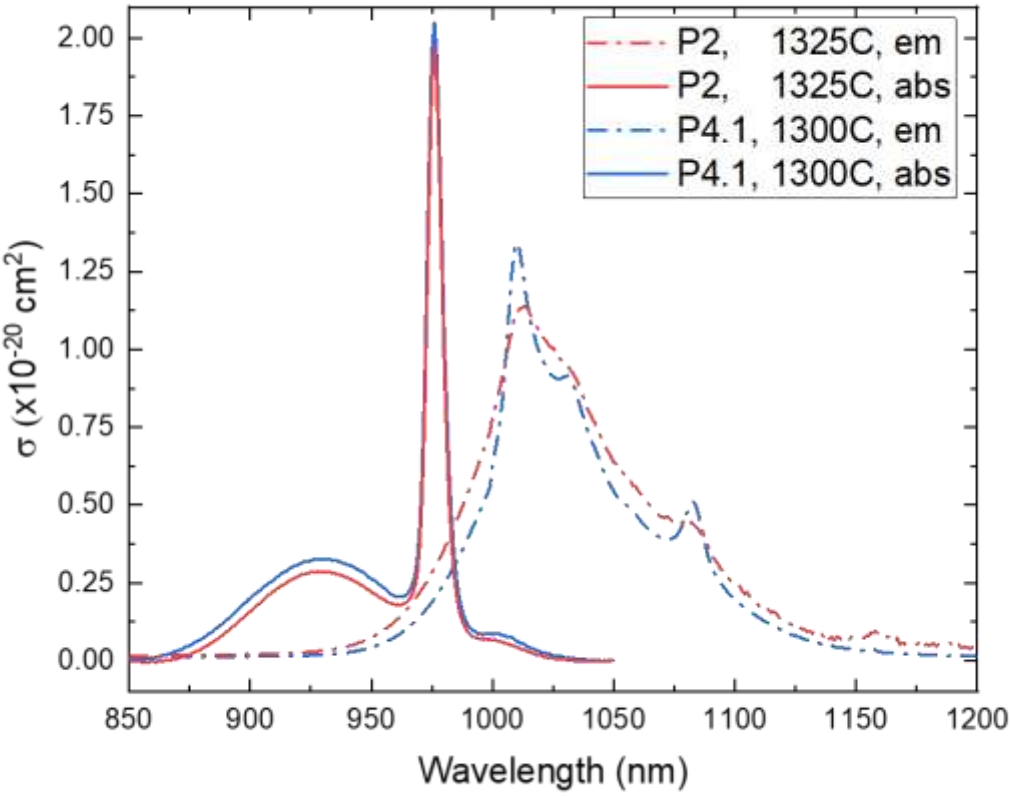

Figure 2.30: Absorption Cross Sections (Solid) and Emission Cross Sections (Dashed) vs. Wavelength for Oxide and Nitrate Doped Samples

2.4. Conclusions and Future Work

In this chapter we presented processes and techniques used to fabricate highly transparent, undoped polycrystalline alumina as a starting point. We highlighted the narrow processing temperature window that when exceeded, increases the scattering of the bulk ceramics. We shared our work on rare-earth doped, polycrystalline alumina ceramics, including powder processing impacts on the optical properties of the densified ceramics. Specifically, we shared the first reported transparent ytterbium doped, nanocrystalline alumina ceramics for use

as laser gain media. Processing steps, optimization, and characterization of the best samples were thoroughly discussed highlight the potential for this new material to move us to higher energy laser systems in the near future. The samples fabricated in this work have strong absorption in the pumping wavelength of 976 nm, and broad emission in the lasing wavelengths between 1010 nm and 1030 nm. Broad emission at the lasing wavelengths provides a unique opportunity to treat Yb:Al_2O_3 as a short-pulsed amplification material similar to Ti:Sapphire, or to use it as a typical laser gain media similar to Nd:YAG.

In order to test these fully characterized samples as functional gain media, a gain experiment is being designed similar to how work had been conducted previously on Neodymium doped TM-DAR [8]. In the near future the samples reported in this work will be tested in a single pass gain experiment as pictured in **Figure 2.31**.

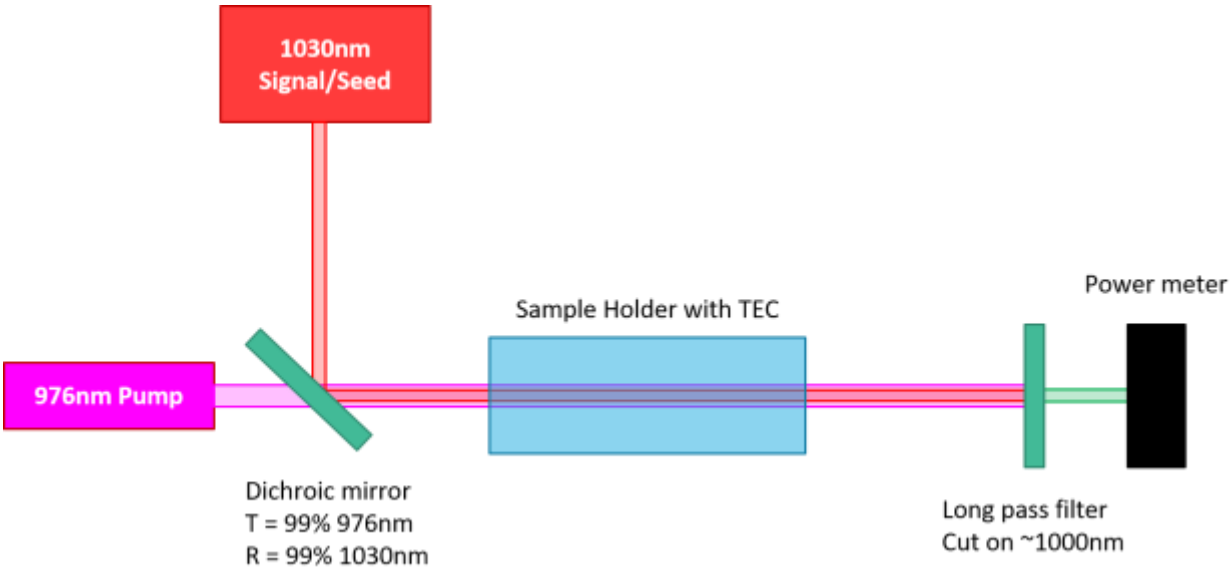

Figure 2.31: Schematic of Single Pass Gain Experiment for Yb Doped Alumina Samples

2.5. References

[1] Garay, J. E. "Current-activated, pressure-assisted densification of materials." *Annual review of materials research* 40 (2010): 445-468.

[2] Shachar, M. H., Uahengo, G., Penilla, E. H., Kodera, Y., and Garay, J. E. "Modeling the effects of scattering and absorption on the transmission of light in polycrystalline materials." *Journal of Applied Physics* 128.8 (2020).

[3] Beil, K., Fredrich-Thornton, S. T., Peters, R., Petermann, K., and Huber, G. "Yb-doped thin-disk laser materials: A comparison between Yb: LuAG and Yb: YAG." *Advanced Solid-State Photonics*. Optical Society of America, 2009.

[4] Koerner, J., Vorholt, C., Liebetrau, H., Kahle, M., Kloepfel, D., Seifert, R., Hein, J., and Kaluza, M. C. "Measurement of temperature-dependent absorption and emission spectra of Yb: YAG, Yb: LuAG, and Yb: CaF 2 between 20 C and 200 C and predictions on their influence on laser performance." *JOSA B* 29.9 (2012): 2493-2502.

[5] Cavillon, M., C. Kucera, T. W. Hawkins, N. Yu, P. Dragic, and J. Ballato. "Ytterbium-doped multicomponent fluorosilicate optical fibers with intrinsically low optical nonlinearities." *Optical Materials Express* 8.4 (2018): 744-760.

[6] Geusic, J. E., H. M. Marcos, and LeGrand Van Uitert. "Laser oscillations in Nd-doped yttrium aluminum, yttrium gallium and gadolinium garnets." *Applied Physics Letters* 4.10 (1964): 182-184.

[7] Aull, B., and H. Jenssen. "Vibronic interactions in Nd: YAG resulting in nonreciprocity of absorption and stimulated emission cross sections." *IEEE Journal of Quantum Electronics* 18.5 (1982): 925-930.

[8] Penilla, E. H., Devia-Cruz, L. F., Duarte, M. A., Hardin, C. L., Kodera, Y., and Garay, J. E. "Gain in polycrystalline Nd-doped alumina: leveraging length scales to create a new class of high-energy, short pulse, tunable laser materials." *Light: Science & Applications* 7.1 (2018): 1-12.

2.6. Acknowledgements

Funding of this work by the Office of Naval Research (ONR) and the Directed Energy Joint Technology Office (DE-JTO) is most gratefully acknowledged.

Chapter 2, in part is currently being prepared for submission for publication of the material. Xingzhong Wu, Yasuhiro Kodera, and Javier E. Garay are co-authors for this work. The dissertation author was the primary researcher and author of this material.

CHAPTER 3. LASER MATERIAL INTERACTION STUDIES

3.1. Introduction to Chapter 3

The following chapter describes work conducted to support studies of laser material interaction (LMI) of metals and semiconductors. Detailed processed and procedures for fabrication of targets used in these studies are shared, and summaries of results generated from these targets are provided.

3.2. Material Selection

For this work, aluminum and silicon were selected for study. Aluminum as the model metal material, and silicon as the model semiconductor material. The rationale for these two materials was to start with the fundamentals, understanding simple materials that do not undergo phase changes at the pressures expected to be generated, and build up to complex composite or alloyed materials from there. **Figure 3.1** depicts the Pressure vs. Temperature phase diagrams for both of these selected materials, and shows that as long as temperatures remain moderately low during experiments, which is expected, then the materials were not expected to exhibit any phase transitions.

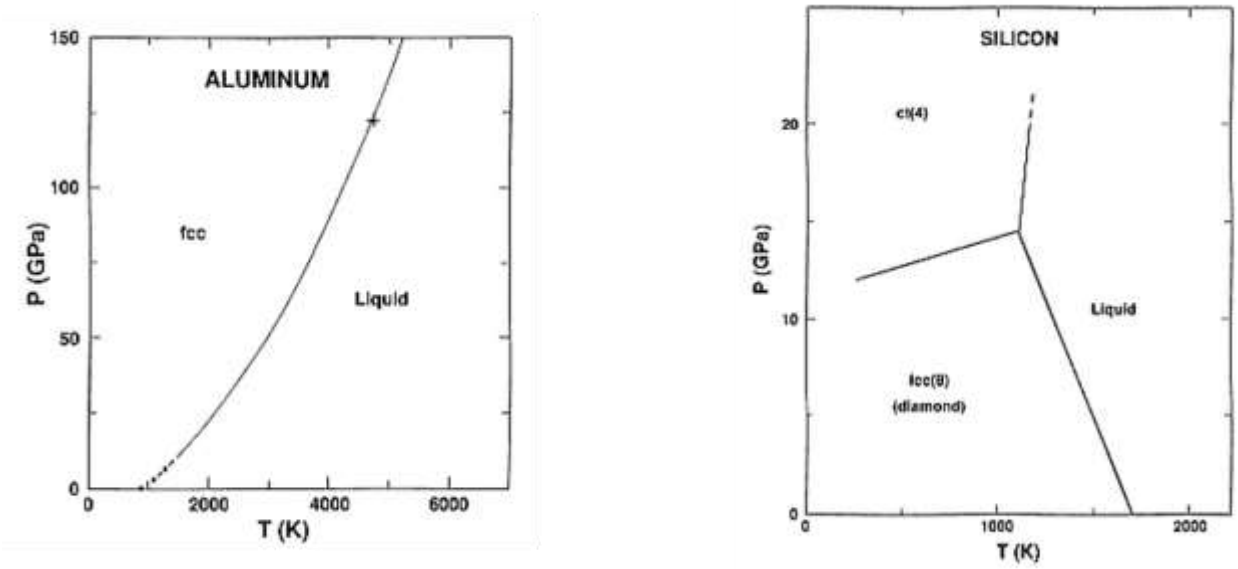

Figure 3.1: Pressure vs. Temperature Phase Diagrams, (Left) Aluminum, (Right) Silicon [1]

3.3. Experimental Methods

The following sections provide detailed descriptions of the procedures used to fabricate both deposited and bonded targets.

3.3.1. Deposited Targets

DC magnetron sputtering was selected for this work due to its ability to deposit highly dense and uniform films on multiple substrates.

All sputtered targets in this work utilized a Denton 18 Discovery (Denton Vacuum, USA) sputter system in UCSD's Nano3 cleanroom facilities. This equipment was set up for confocal sputtering and had three cathodes, two DC cathodes, and one RF cathode. All of the sputtering for this work was conducted using the two DC cathodes, and the stage RF Bias/Etch process was

utilized for additional substrate preparation prior to sputtering. Substrates were attached to the center of a 6 inch steel platen using kapton tape to maintain consistent placement of substrates run to run, and provided a location to measure film thickness. The sample platen was rotated at approximately 13 RPM for the duration of every run. Substrate heating was only utilized on hygroscopic substrates.

The substrates sputtered onto as part of this work were all dual side polished (DSP) and include 180 μm thick amorphous soda-lime glass, (Amscope, USA), 500 μm thick single crystal sapphire, c-cut (MTI Corporation, USA), 200 μm thick single crystal quartz, z-cut (University Wafer, USA), and 1000 μm thick single crystal lithium fluoride (LIF), (100) orientation (Asphera, USA). Of these substrates, the LiF substrates provided an additional challenge in depositing films due to its hygroscopic nature. Substrates were diced into 5 mm x 5 mm or 10 mm x 10 mm squares with the exception of the soda-lime glass which was 22 mm x 22 mm.

The sputter target materials deposited onto these substrates as part of this work include titanium, 99.995% pure (Kurt J. Lesker, USA), aluminum, 99.9995% pure (Kurt J. Lesker, USA), and chromium, 99.95% pure (Kurt J. Lesker, USA). All sputter targets were 3 inches in diameter, and approximately 0.25 inches thick when new.

Substrate cleanliness is crucial to the successful deposition of thicker films to ensure a good initial bond and prevent delamination of film from the substrate. It was quickly discovered that some classes of substrates required additional care, and others were quite tolerant of the initial surface conditions. **Table 3.1** quickly summarized the cleaning processes and which solvents and fluids were used to produce consistent deposited films.

Table 3.1: Substrate Cleaning Process for Sputtered Films

	Cleaning Processes		
Substrate	Process 1	Process 2	Process 3
Inert (Sapphire, Quartz, Soda-Lime Glass)	Acetone	Isopropyl Alcohol	UHP Water
Hygroscopic (LiF)	Acetone	Methanol	Isopropyl Alcohol

For more inert or stable substrates, such as the sapphire, quartz, and soda-lime glass, the cleaning process began by rinsing the entire substrate with acetone, and wiping the surfaces with a lint free cloth. The substrate was then rinsed entirely with isopropyl alcohol, and wiped again with a lint free cloth. Last the substrate was rinsed with ultra-high purity (UHP) water and wiped dry with a lint free cloth. Once cleaned the substrate was wrapped in a clean room cloth, placed in a sample bag, and stored in a container to take into the cleanroom.

For hygroscopic substrates, such as LiF, it was quickly determined that UHP water needed to be excluded from the process, but initial cleanings with just acetone and isopropyl alcohol saw failures in adhesion of thinner deposited layers. For LiF substrates, the first step was to rinse entirely with acetone, and wiped with a lint free cloth. The newly inserted step was to rinse the substrate entirely with methanol and wiped with a lint free cloth. Last, the substrate was rinsed with isopropyl alcohol, and wiped dry with a lint free cloth. Once cleaned, similar to less sensitive substrates, the substrate was wrapped in a clean room cloth and placed in a sample bag to be taken to the clean room.

In addition to the cleaning steps detailed above, all substrates were further cleaned using the RF Bias/Etch capability of the equipment. This process allows a bias to be applied across

they system, essentially turning the sample plate into a deposition target, also known as a glow plate. RF Bias/Etch was performed on all substrates only once the system reached a process vacuum level of $4.5x10^{-6}$ Torr, and argon was used as the sputter gas. 100 W of RF power, at a sputter pressure of 8 mTorr, was applied for 2 minutes to clean the surfaces prior to metal deposition.

For depositing metals, all sputtering used argon as the sputter gas, and between each step the system was allowed to reach a process vacuum level of $4.5x10^{-6}$ Torr or less before moving on to subsequent steps.

A thin titanium adhesion layer was employed to improve experimental target transport and handling. The titanium target was pre-sputtered at 200 W, at 2.5 mTorr, for 2 minutes with the shutter closed in order to clean the sputter target surface prior to deposition on the substrate. Titanium was then sputtered at 200 W, at 2.5 mTorr, for 90 seconds which produced an adhesion layer measured between 5 nm and 10 nm thick.

Aluminum was deposited immediately following the titanium adhesion layer. First, the aluminum sputter target was pre-sputtered at 200 W, at 2.5 mTorr, for 2 minutes with the shutter closed to clean the aluminum target prior to deposition. Aluminum was then sputtered ate 200 W, at 2.5 mTorr, for the necessary time to achieve the desired thickness. This time typically ranged from 45 minutes to 100 minutes. Note that during any sputter run longer than 15 minutes there was a need to adjust the flow rate of argon to maintain a consistent sputter pressure. The system used mass flow control, and was adjusted in 0.25 standard cubic centimeters per minute (sccm) increments anytime the readout of sputter pressure flickered between 2.5 mTorr and 2.4 mTorr. These minor adjustments throughout the longer sputter runs resulted in very repeatable film thicknesses sputtered on different days and on different substrates.

After the aluminum deposition was completed and the sputter target shutter closed, the substrate remained rotating and was held for five minutes with the argon flowing and a 4 mTorr sputter pressure. This process was employed to help the chamber equilibrate in temperature and pressure prior to venting.

Figure 3.2 is a simplified diagram showing the deposition process. Step 1, the substrate is cleaned using the RF Bias/Etch feature. Step 2 is the deposition of the adhesion layer (red). Step 3 is the deposition of the desired material (yellow) and Step 4 is the argon hold to stabilize the chamber.

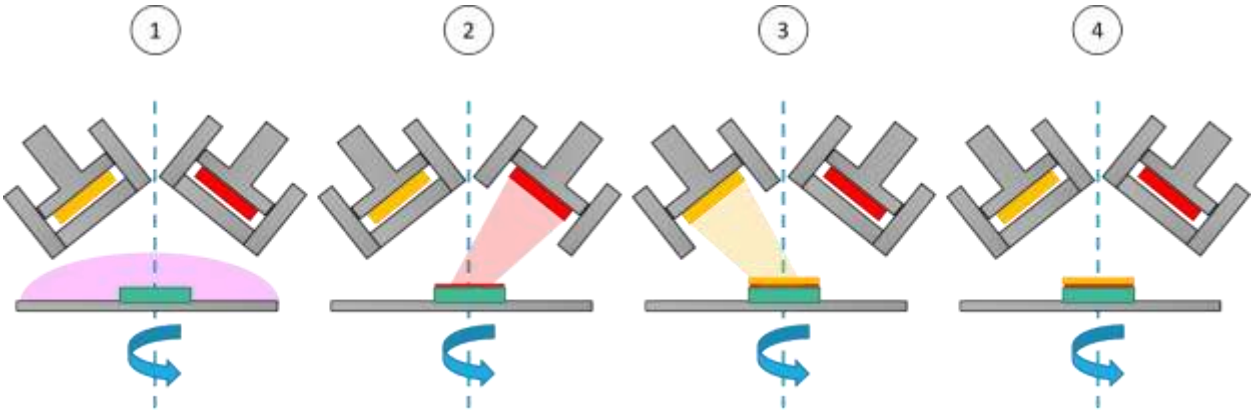

Figure 3.2: Simplified Deposition Process Diagram

LiF substrates specifically required one additional process prior to the RF Bias/Etch and deposition steps due to their hygroscopic nature. This step was implemented to both clean the surfaces of any residual moisture, and to lower the thermal energy imparted into the substrate by the sputtering process. Once the chamber reached a process vacuum level of 4.5×10^{-6} Torr, the stage heating was enabled. The sample plate temperature was raised in increments of 10°C, allowing for any overshooting to slow prior to sequential increases. The stage was heated to 198°C which was stable control point that would command the heat lamps when it cooled to

197°C and not overshoot to more than 204°C. Once at this hold temperature, the chamber was allowed to bake for a minimum of 20 minutes to allow the vacuum to stabilize. Every time the lamps were powered turned on, the vacuum level noticeably spiked, causing the system to no longer have an appropriate process vacuum level. Waiting the 20 minutes allowed for the entire system to stabilize, and once the process vacuum remained below $4.5x10^{-6}$ Torr even with the lamps on, the next steps could be carried out. Once able to sustain the process vacuum with the heating lamps on, the substrate heating was allowed to ramp one more time, was turned off, and the RF Bias/Etch process started. Immediately after that, the deposition of titanium and aluminum followed. By the end of a 45 minute and 100 minute sputter run, the sample stage had a reported temperature of approximately 110°C and 85°C respectively. If the system was above 100°C at the end of the run, the system was allowed to cool to with argon flowing until the temperature reached below 100°C, at which point the system was vented and the platen removed.

Thicknesses of deposited materials were measured using a DektakXT stylus profilometer (Bruker, USA) in a separate bay of the cleanroom. Every sample was measured in a minimum of three separate locations where the kapton tape was removed from the substrate to record an average thickness. This provided a bare surface of the substrate to start the measurement, and then dragged the stylus up an over the deposited metal step in the three or more positions to get the average thickness estimate.

3.3.2. Bonded Targets

The layers or substrates utilized for bonded targets included 200 μm and 500 μm thick single crystal quartz, z-cut (University Wafer, USA), 25 μm thick copper foil, 99.99% pure (Alfa Aesar, USA), and 50 μm thick single crystal silicon, (100) orientation (University Wafer, USA).

The adhesives used as part of this work include cyanoacrylate adhesive (Krazy Glue, USA), which is a readily available adhesive and only requires a 60 second cure at room temperature, Loctite EA E-30CL (Henkel, USA), which is a low viscosity industrial adhesive and requires a 24 hour cure at room temperature, and Masterbond U15LV (Masterbond, USA), which is a single part low viscosity ultraviolet (UV) light curable adhesive and requires a 15-30 second cure cycle when exposed to 320-365 nm light.

Cyanoacrylate adhesives benefit from their accessibility, low cost, and fast curing times. Loctite is a useful adhesive when the materials are not transparent to a curing source (wavelength dependent curing), but do have a significantly longer curing time than the other two. Loctite is significantly more viscous than the other adhesives used, and Masterbond has a similar viscosity to that of cyanoacrylate adhesives. Masterbond is cost prohibitive when compared to other adhesives, requires careful handling to limit exposure to UV light sources, but is quick to cure and enables making batches of targets in relatively short timespans.

Bonding targets was broken into two methodologies. The first methodology is fully wetting the interface between two substrates and allowing squeeze out. This process ensures that the majority of the interface is contaminate free, and that no bubbles are formed within the adhesive layer. Fully wetting processes require low viscosity adhesives to be successful, fast curing times are preferred, and thicknesses are able to be measured by comparing masses before and after bonding with an accurate enough scale. The second methodology is to apply the bare minimum amount of adhesive to begin with, and spread that small amount of material across the interface. This method is less dependent on the viscosity of the adhesive because so little adhesive is applied initially, but is significantly more susceptible to contamination and

unevenness due to the increased time required to manually spread the adhesive across the base substrate (between 5 and 10 minutes per layer).

Flowing these two methodologies for bonding into target fabrication, two target fabrication techniques were employed. First is the fully wetted bond between two substrates, illustrated in **Figure 3.3**, and second is the minimum adhesive bond between two substrates, illustrated in **Figure 3.4**.

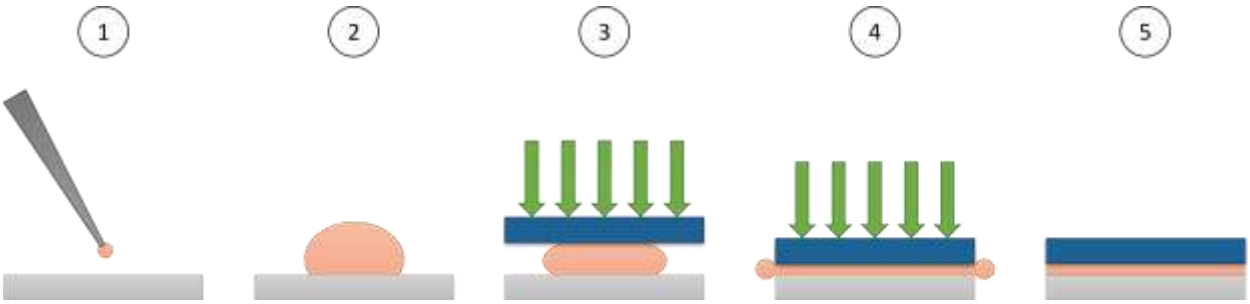

Figure 3.3: Substrate Bonding Process Diagram, Fully Wetted Interface between Two Surfaces Method

Figure 3.3 depicts the process of a fully wetted interface bond between two substrates, which typically uses a fast curing adhesive. Step 1 is applying the adhesive to a clean base substrate. Step 2 is applying enough adhesive to ensure squeeze out. Step 3 is applying a pressure to the glue using the second substrate to move the adhesive. Step 4 is applying continuous pressure to the second substrate while the adhesive cures. Notice the squeeze out on the sides of the substrate in the diagram in step 4. Step 5 is cleaning the outer edges of the multilayered target mechanically with a blade, or with a solvent that is applicable to the adhesive. It is critical to remove excess adhesive from the edges to ensure accurate estimates of the adhesive thickness.

Thicknesses of fully wetted interface bonded targets were estimated by weighing each substrate or layer, and weighing the final cleaned target. Using the density of the adhesive, and a coverage factor to be conservative (>90% to account for edge losses from cleaning), adhesive layer thicknesses were estimated. Using this bonding method, adhesive layers were found to be between 8 μm and 14 μm with limited applied pressures and short curing times.

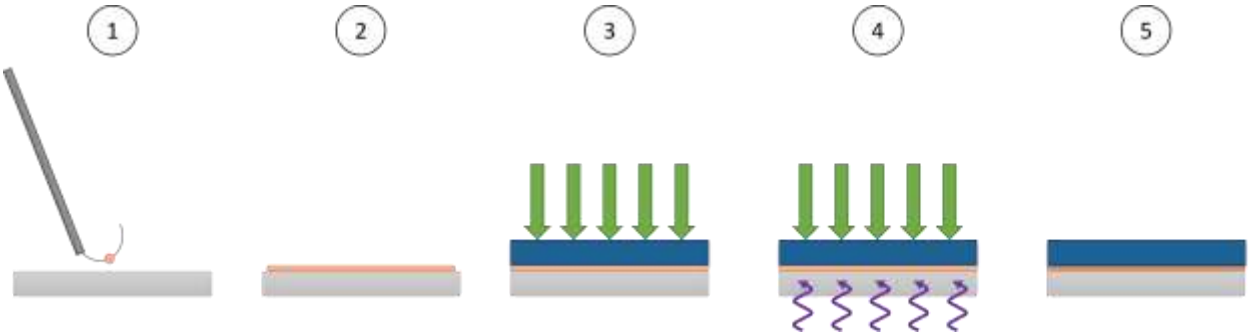

Figure 3.4: Substrate Bonding Process Diagram, Minimum Adhesive between Two Surfaces Method

Figure 3.4 depicts the process of a minimum adhesive bond between two substrates, which can use multiple types of adhesives. Step 1 is collecting the smallest amount of adhesive on the end of a thin wire or hair/whisker attached to a rod or handle. Step 2 is manually spreading the adhesive over the surface of the base substrate, as evenly as possible. Step 3 is applying a pressure to the second substrate uniformly. Step 4 is a continued pressure applicator for time-based cures, or applying UV light/heat (shown in purple) to cure wavelength dependent or heat curing adhesives. Step 5 is any minimal cleanup of the multilayered target with solvents, paying careful attention to the edges where adhesive can be quickly removed if excess amounts of solvents are used.

Thickness of the minimum adhesive bonded targets were measured using a Heidenhain CERTO length gauge (Heidenhain, Germany). Each substrate layer was measured prior to

bonding, and the final assembled target was measured in multiple locations. The CERTO had a 0.5 μm resolution, so when subtracting the initial thickness from the final thickness value, the thickness was rounded up as a conservative estimate. Using this method, adhesive layers were regularly reproduced between 1 μm and 3 μm.

3.4. Results and Discussion

3.4.1. Aluminum Targets

Inspired by previous work in tamped ablation of aluminum [2], a complimentary study of aluminum on different tamper materials was conducted. The goal was to study the impact of the tamper material on the generation of pressures within the aluminum films. Sapphire and LiF were selected as substrates for this work, and soda-lime glass was also studied. **Figure 3.5** is a schematic of the sapphire and LiF targets.

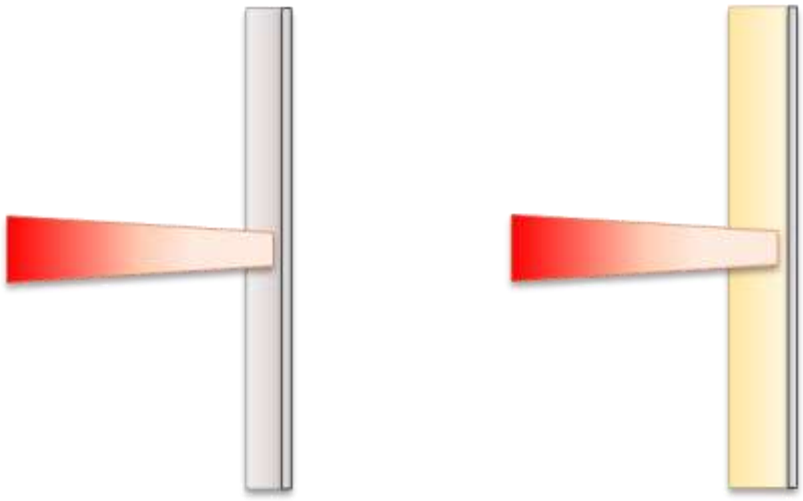

Figure 3.5: Schematic of Deposited Aluminum Targets for Tamped Ablation Studies, (Left) Sapphire Tamper, (Right) LiF Tamper

Aluminum films were deposited on sapphire, LiF, and soda-lime glass substrates following the procedures listed in **Section 3.3.1**. All targets had a 5 nm to 10 nm titanium adhesion layer to improve handling and transportation. Multiple aluminum thicknesses were deposited for experiments ranging from 300 nm – 1200 nm. Examples of the films after deposition are shown in **Figure 3.6**.

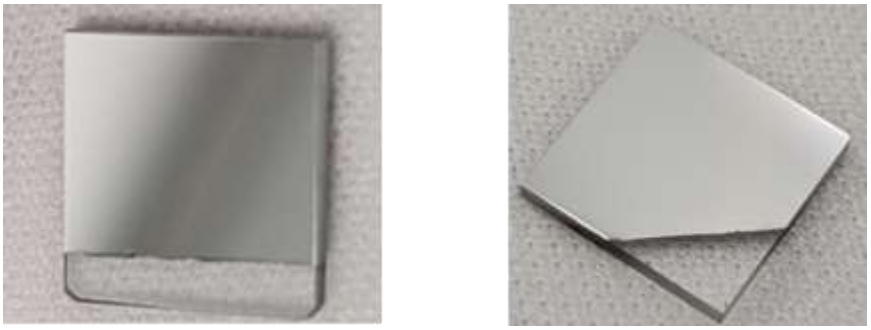

Figure 3.6: Deposited Aluminum Targets for Tamped Ablation Studies, (Left) Sapphire Tamper, (Right) LiF Tamper

Unfortunately no data was able to be measured with the LiF samples due to challenges with equipment. Aluminum targets on soda-lime glass and sapphire were successfully shot and pressures measured. Pressures generated in the sapphire tamped targets were higher for the same intensities shots than pressures generated in the soda-lime glass tamped targets [3].

In the development of the process for depositing aluminum on various substrates, careful attention was taken to quantify film thicknesses using soda-lime glass slides. These slides were sputtered along with the substrates in order to better characterize deposition rates.

Figure 3.7 presents average thickness measurements of aluminum layers deposited on both soda-lime glass slides, and sapphire substrates. Note all of these measurements included the titanium adhesion layer. These values are the average of a minimum of three measurements

across the layer step using the DektakXT (Bruker, USA). For these measurements, the glass substrates were 1000 μm thick and the sapphire substrates were 500 μm thick. It is clear to see that the average thickness of films is greater on the glass than on the sapphire substrates. To briefly look into the trends of the two, liner fits to the data are presented in **Figure 3.8**.

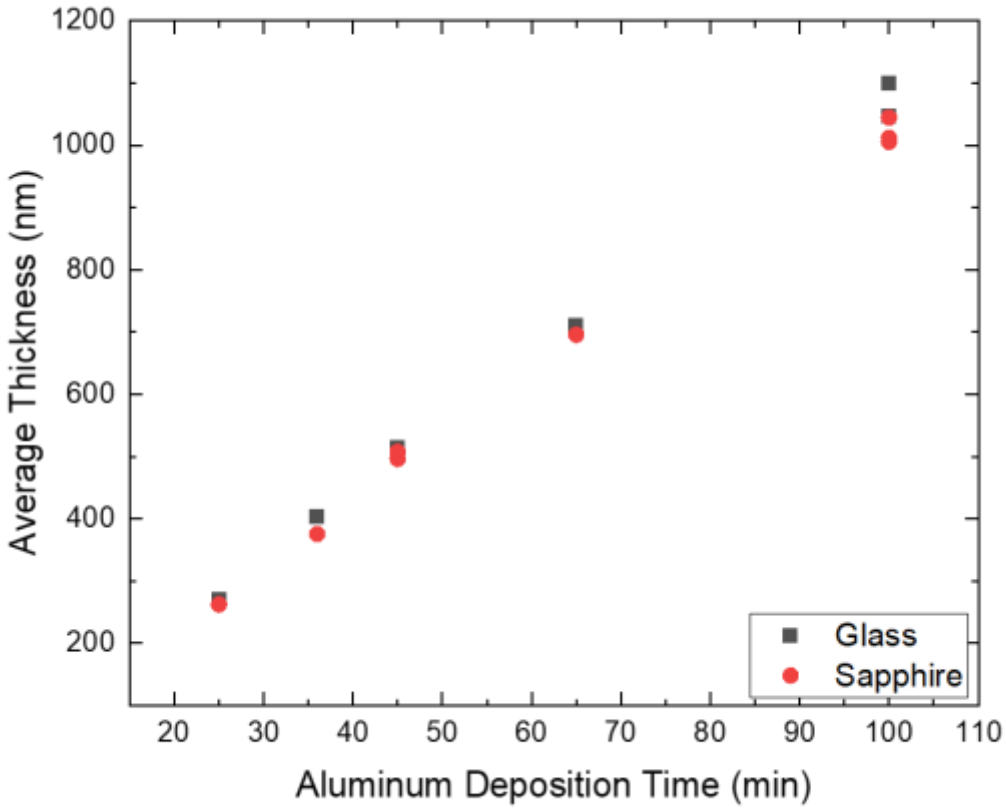

Figure 3.7: Average Thickness vs. Aluminum Deposition Time for Glass Slide and Sapphire Substrates

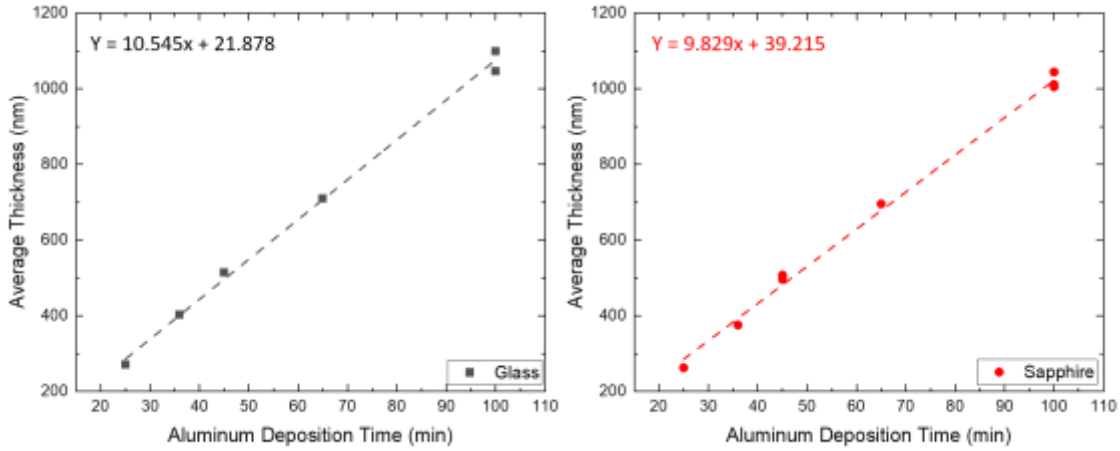

Figure 3.8: Average Thickness vs. Aluminum Deposition Time with Linear Fits, (Left) Glass Slide, (Right) Sapphire

The approximate sputter rates based off of the slope of each line for the 500 μm thick sapphire substrates was 9.8 nm/min and the approximate sputter rate for the 1000 μm glass slide reference was 10.5 nm/min. This makes sense intuitively in that the thicker substrates are closer to sputter target, and see a slight increase in material deposited based solely on their thickness. This difference in sputter rate may seem negligible, but over the course of 100 minute deposition runs or longer, can result in deposited films that are above or below the desired thickness based on the thickness of substrate.

3.4.2. Silicon Targets

To support high intensity studies of silicon ablation, a three layer target was designed and is presented in **Figure 3.9**. These three layer targets included a 50 μm thick single crystal silicon, (100) orientation (University Wafer, USA), 25 μm thick copper foil, 99.99% pure (Alfa Aesar, USA), 500 μm thick single crystal quartz, z-cut (University Wafer, USA). These targets

were bonded using cyanoacrylate adhesive (Krazy Glue, USA). Each layer was bonded using the full wetting method, and the glue layer thicknesses were estimated using the mass differences during bonding as described in **Section 3.3.2**.

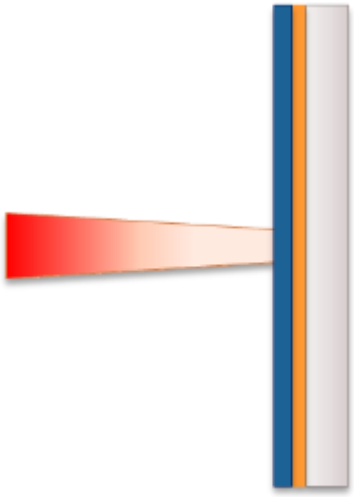

Figure 3.9: Schematic of OMEGA EP Experiments Targets for Untamped Ablation Studies

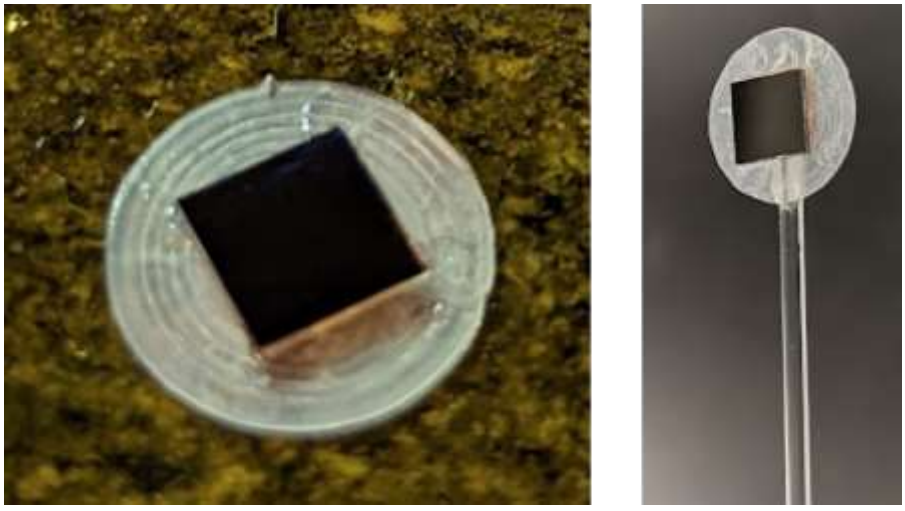

Figure 3.10: Photographs of Target Development for OMEGA EP Experiments, (Left) 2022 Campaign Sample Prior to Mounting on the Glass Stalk, (Right) 2021 Bonding Test with Thicker Silicon

The experiments at OMEGA EP primarily aimed to understand the time-resolved evolution of plasma from the laser drive surface, the silicon layer, as a function of laser pulse duration at constant intensity, ~ $4x10^{14}$ W/cm^2. Note that the laser wavelength used for these experiments was 351 nm. Specific details of the experiments, the diagnostics, and the results can be found in the recently submitted paper by Hanh et al. [4] where the target fabrication techniques and target development shown in this work were applied. It is important to note that these targets are completely destroyed after a single shot, leaving very little to be studied in post. This is generally fine for the plasma physics approach to the study, but does not allow for much in terms of materials characterization during the shot, or a post shot analysis of phase changes, and the fundamental laser material interaction mechanisms at play in a given material.

Another facility that targets were designed and fabricated for was the Optical Sciences Laser (OSL) at Lawrence Livermore National Laboratory (LLNL). These targets aimed to continue the study of silicon from the OMEGA EP experiments, at lower intensities, ~$1x10^{12}$ W/cm^2, and with the wavelength of 532 nm. For these studies the diagnostics were limited to a Photon Doppler Velocimetry (PDV) system, which measures the movement of a reflective surface with high temporal resolution. Due to this being the single diagnostic in the experimental design, the ability to reflect a beam near the silicon surface was critical. This led to the development of two target designs, one that only had the silicon bonded to a transparent substrate, and one with a metal inter-layer to ensure reflectivity.

OSL experiment targets utilized the same 50 μm thick single crystal silicon, (100) orientation (University Wafer, USA), and used 200 μm thick single crystal quartz, z-cut (University Wafer, USA). For the targets with a metal inter-layer, they utilized a deposited

~100nm thick, chromium layer, 99.95% pure (Kurt J. Lesker, USA) on the quartz substrate. Both of these target designs are illustrated in **Figure 3.11**.

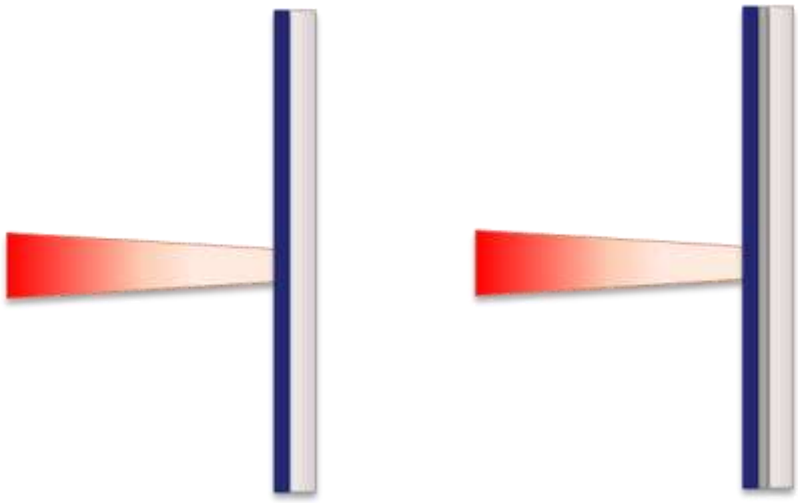

Figure 3.11: Schematic of Silicon/Quartz Bonded Targets, (Left) Direct Bond, (Right) Chromium Deposited on Quartz and Bonded

Targets for these experiments were fabricated using the minimum adhesive bond technique described in **Section 3.3.2**. The silicon/quartz targets were bonded using Masterbond U15LV (Masterbond, USA), due to the quartz being transparent to the UV wavelengths necessary to cure, while the chromium coated quartz substrates were bonded to the silicon using Loctite EA E-30CL (Henkel, USA) which required a 24 hour cure time. These targets were fabricated over the course of many months, in direct collaboration with LLNL scientists and students, but unfortunately the experiments were not able to be conducted prior to the submission of this dissertation.

3.5. Conclusions and Future Work

In this chapter multiple techniques for the fabrication of targets for Laser Material Interaction (LMI) studies were presented and explored. Specific examples of target designs and fabrication techniques were presented, and soon to be published papers exploring the physics being studied with these targets were shared where possible.

Follow on work to these types of targets would include three layer targets that utilize no adhesives, but instead leverage diffusion bonding of metal layers that are deposited onto substrates. A system like CAPAD [5] as explained in previous chapters, allows for specific control of the temperature and pressure applied in a vacuum environment, allowing for the bonding of two substrates sputtered with the same metal. Initial work was conducted for these types of targets, primarily focused on studying the mechanical impedance of different materials. An example of a target to study would be a sapphire tamper, sputtered with aluminum, and a LiF substrate also sputtered with aluminum. The two targets would be diffusion bonded between the two aluminum layers, and a drive laser would induce a tamped pressure at the sapphire/aluminum interface. From there the shock would travel through the bonded aluminum layer, and travel across the aluminum/LiF interface unperturbed due to aluminum and LiF having similar mechanical impedances.

In addition to new target fabrication techniques, another interesting method to understand the material behavior would be to study the depth or volumetric dependence of the material. The thicker the substrate that is studied, the more likely the study could capture some more detailed material behaviors of the substrate that are not specifically related to the plasma formation when laser energy is deposited into the substrate. Here studies could be conducted both in the thickness of a direct driven material like the silicon targets, and could also study the deposited

material thicknesses and how tamped and untamed ablation impact the energy coupling into the materials.

3.6. References

[1] Young, David A. *Phase diagrams of the elements*. Univ of California Press, 1991.

[2] Crowhurst, J.C., Armstrong, M.R., Knight, K.B., Zaug, J.M. and Behymer, E.M. "Invariance of the dissipative action at ultrahigh strain rates above the strong shock threshold." *Physical review letters* 107.14 (2011): 144302.

[3] Parsons, S. E., Armstrong, M. R., Turner, R. E., Radousky, H. B., Radousky, Garay, J. E., Beg, F.N. "Laser material interactions in tamped materials on picosecond timescales in Aluminum" *Applied Physics Letters* – In Prep

[4] Hanh, E. N., Bailly-Grandvaux, M., Cordova, T., Turner, R. E., Joshi, T.R., Spielman, R.B., Wicks, J. K., Garay, J. E., Beg, F. N. "Laser pulse-length dependent ablation and shock generation in silicon at $4x10^{14}$ W/cm^2 intensities." *Physical Review Research* – in Review

[5] Garay, J. E. "Current-activated, pressure-assisted densification of materials." *Annual review of materials research* 40 (2010): 445-468.

3.7. Acknowledgements

The project or effort depicted was or is sponsored by the Department of the Defense, Defense Threat Reduction Agency under award HDTRA1-20-2-0001. The content of the information does not necessarily reflect the position or the policy of the federal government, and no official endorsement should be inferred.

Chapter 3, in part is currently being prepared for submission for publication of the material. Sophie E. Parsons, Alison K. Ackerman, Michael R. Armstrong, Harry B. Radousky,

Farhat N. Beg, and Javier E. Garay are co-authors for this work. The dissertation author was the primary researcher and author of this material.

CHAPTER 4. LAB SCALE LASER ABLATION STUDIES

4.1. Introduction to Chapter 4

This chapter contains additional lab scale studies of silicon damage as a function of laser intensity, with a focus on the mechanical response and material behavior. The studies aim to bridge the physics and materials studies by providing post shot material characterization and analysis that is not typically available when conducting facility scale experiments, such as the OMEGA EP work and OSL target development shared in **Chapter 3**.

A well-developed model to estimate crater breadth and depth was developed and validated with single pulse experiments [1]. Looking back to **Figure 1.13** which presented two decades of silicon damages studies, it is important to note that very few groups studied single pulse damage, let alone at the intensities seen at a facility like OMEGA. **Figure 4.1** is an updated version of this figure, showing only single shot experiments from the work shared in **Figure 1.13**. Again it is important to note that for work that stated the use of undoped or intrinsic silicon and did not provide a free carrier density, $1x10^{10}$ cm^{-3} was used for **Figure 4.1** [2].

What is interesting is that when looking at single shot experiments exclusively is that the work by Leyder et al. stands out as being the only work in this list to vary free carrier density or doping concentration in silicon. N-type silicon was shown to have a significant decrease in in-line transmission at a threshold free carrier density near 10^{18} cm^{-3} [4]. This inspired further study into silicon ablation characteristics as a function of both free carrier density and laser intensity.

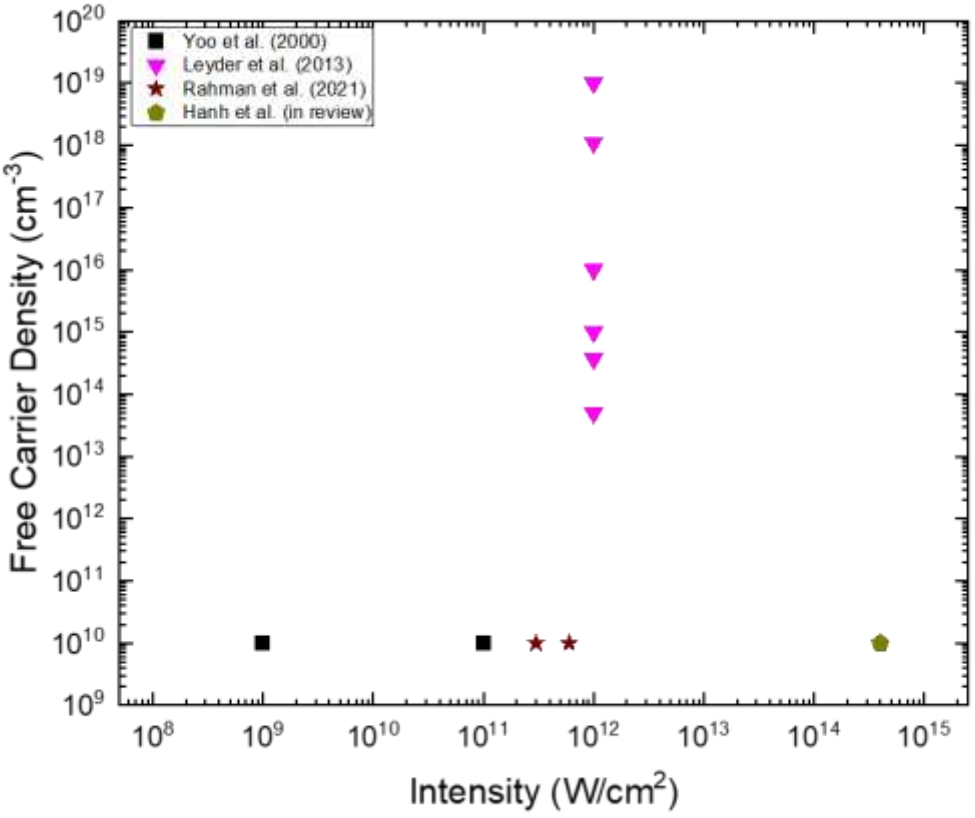

Figure 4.1: Literature Comparison of Single Shot Experiments of Silicon Free Carrier Density (Doping Concentration) vs. Intensity, Log Scale [3-6]

It is surprising that silicon, as ubiquitous as it is, is not as well understood at least in open literature. Studying silicon has primarily focused on the ablation of the surface material and limited post single shot analysis has been presented in open literature leading to the following work being presented.

4.1. Experimental Methods

Phosphorous doped, n-type single crystal silicon substrates (University Wafer, USA) were procured in different doping concentrations. For the purposes of this work, three different doping concentrations were selected based on the work presented by Leyder et al. [4]. To quickly tabulate the selected substrates, **Table 4.1** is presented below.

Table 4.1: Silicon Substrates of Varying Free Carrier Densities for Ablation Experiments

	Thickness (μm)	**Polish**	**Orientation**	**Dopant**	**Resistivity (Ωcm)**	**Free Carrier Density (cm^{-3})**
Undoped	~510	DSP	(100)	n/Ph	>20,000 (undoped)	$\sim 10^{10}$
Medium Doped	~500	DSP	(100)	n/Ph	1-10	$\sim 10^{14}$
Highly Doped	~500	SSP	(100)	n/Ph	0.25-0.75	$\sim 10^{16}$

In order to conduct ablation studies, an experimental setup was required. For the preliminary work, a nanosecond laser setup was constructed which could ablate the silicon, and image the beam to assist in quantifying the intensities driving the ablation. Note that per pulse energy was measured prior to the mechanical iris, meaning that the calculated intensities are slightly over estimated, but directly proportional to the optics and path lengths used. A schematic of the ablation experimental setup is shown in **Figure 4.2**.

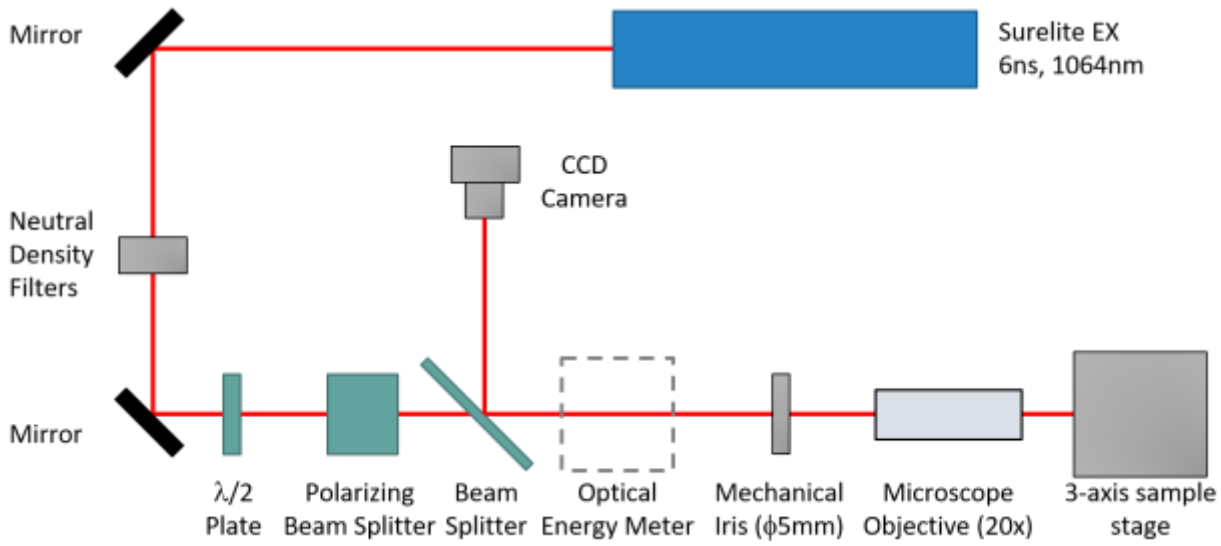

Figure 4.2: Schematic of Benchtop Laser Ablation Experiments

Using this equipment setup, the beam spot size on the target was measured using the reflected beam through the CCD camera, and was determined to be approximately 4μm (when approximated with a Gaussian beam profile) in diameter as shown in **Figure 4.3**.

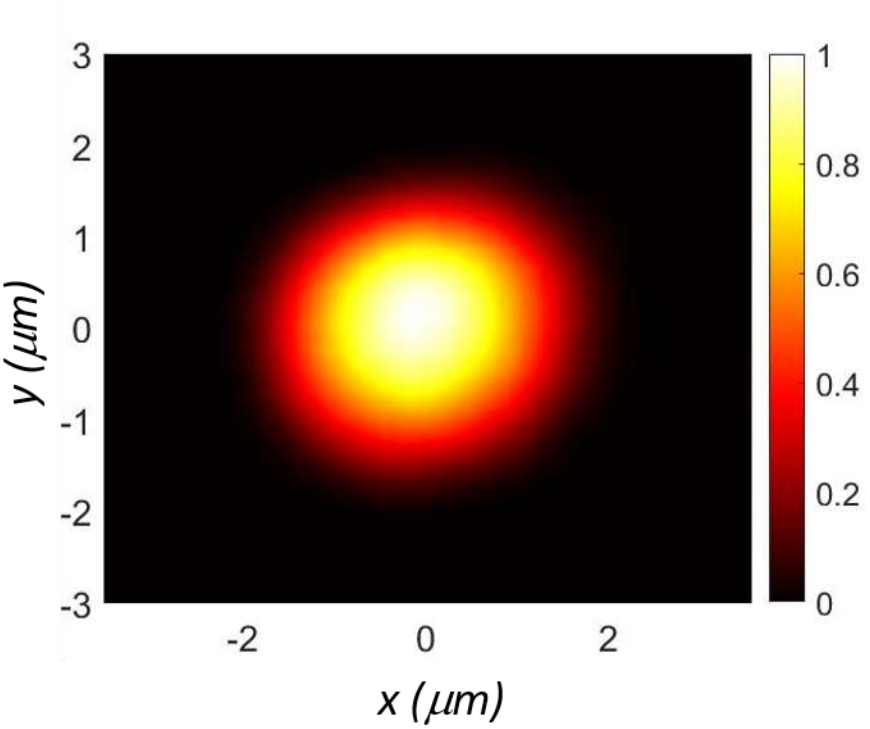

Figure 4.3: Processed CCD Camera Image of Focused Beam, Color Bar Represents Normalized Intensity

Post shot optical characterization was conducted using a Zeis Sigma 500 Scanning Electron Microscope (Zeiss, Germany), and SEM micrographs were processed using ImageJ. This allowed for the characterization of both the diameter of the crater formed, and the overall mechanical appearance of the damage.

In-line transmission measurements were conducted using an Agilent Cary 5000 (Agilent Technologies, USA) UV-Vis-NIR spectrophotometer. **Figure 4.4** is measured in-line transmission data for the three separate silicon samples. The vertical lines represent 532 nm and 1064 nm wavelengths to highlight that the difference in transmission between the samples is negligible at 532 nm, but specifically for the highly doped at 1064 nm there is a significant different in transmission.

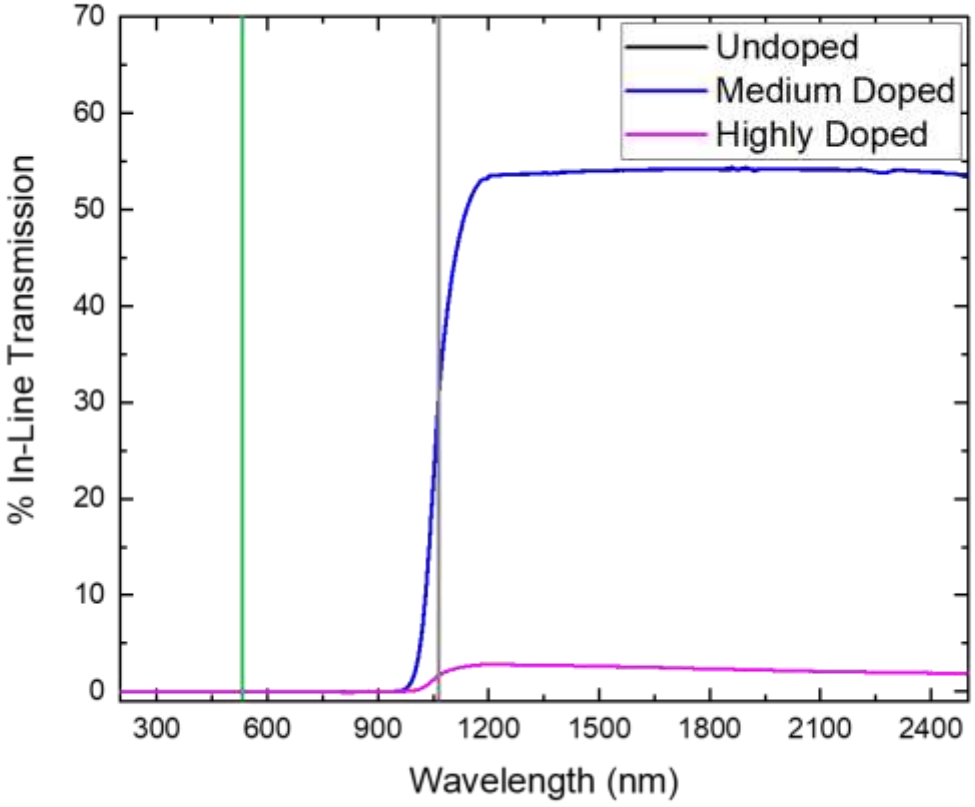

Figure 4.4: % In-Line Transmission vs. Wavelength of Silicon with Varying Free Carrier Densities, Vertical Lines Represent Laser Wavelengths for Study, (Green) 532 nm, (Grey) 1064 nm

4.5. Results and Discussion

Two ranges of intensities were studied at 1064 nm. Low intensity studies ranged from $1x10^{11}$ W/cm^2 and $3x10^{12}$ W/cm^2, while high intensity studies ranged from $1x10^{11}$ W/cm^2 and $3x10^{13}$ W/cm^2. There were a few shots of overlap between the two studies, but the high intensity study had a larger sept size in intensity between shots. Intensity was controlled by attenuating the beam and measuring the energy of a sing pulse immediately before shooting the target. Targets were translated approximately 0.3 mm between shots to avoid shot-to-shot interactions.

For the low intensity studies, the damage diameter for each shot was measured in ImageJ and plotted in **Figure 4.5**.

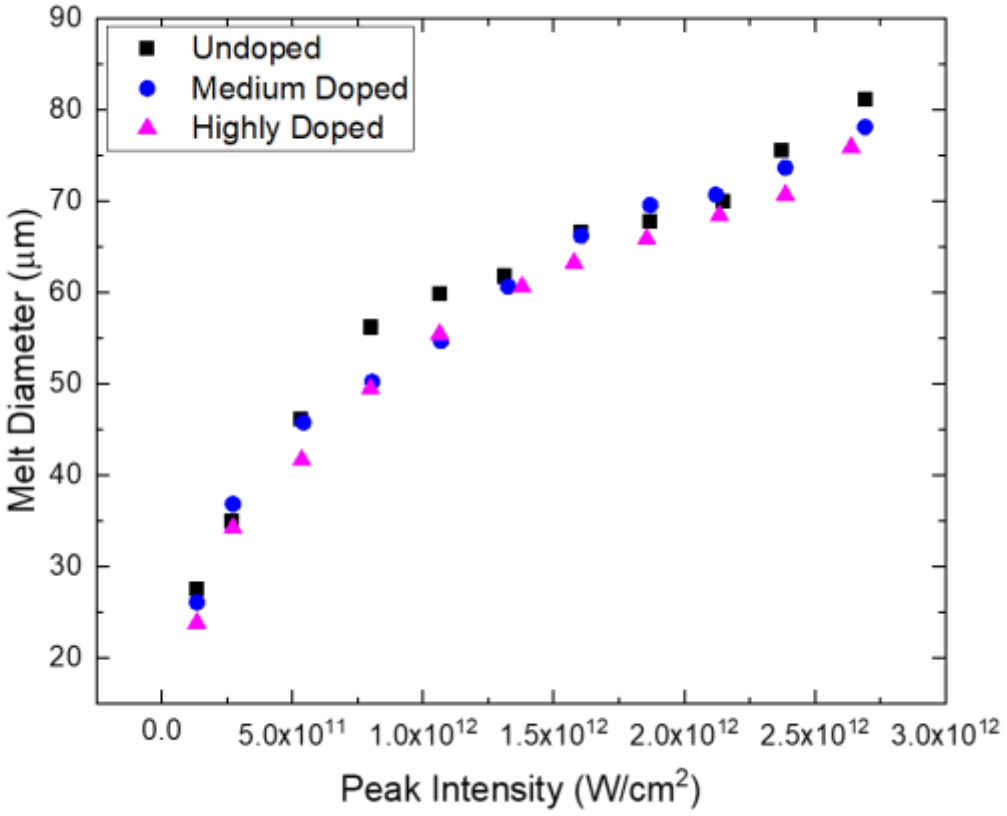

Figure 4.5: Silicon Melt Diameter vs. Peak Intensity, Low Intensity Shots

For the high intensity studies, more variability was observed near $5x10^{12}$ W/cm^2 intensities. This difference in behavior can be seen in **Figure 4.6** where there is a noticeable difference in the damage behavior of the surface of the material as a function of intensity. Primarily there is a change in behavior of the melt from a circular shape to what seems to be

triangular. It is interesting to note that the behavior of the material ablation to form a triangular shape on the surface is consistent across all doping concentrations.

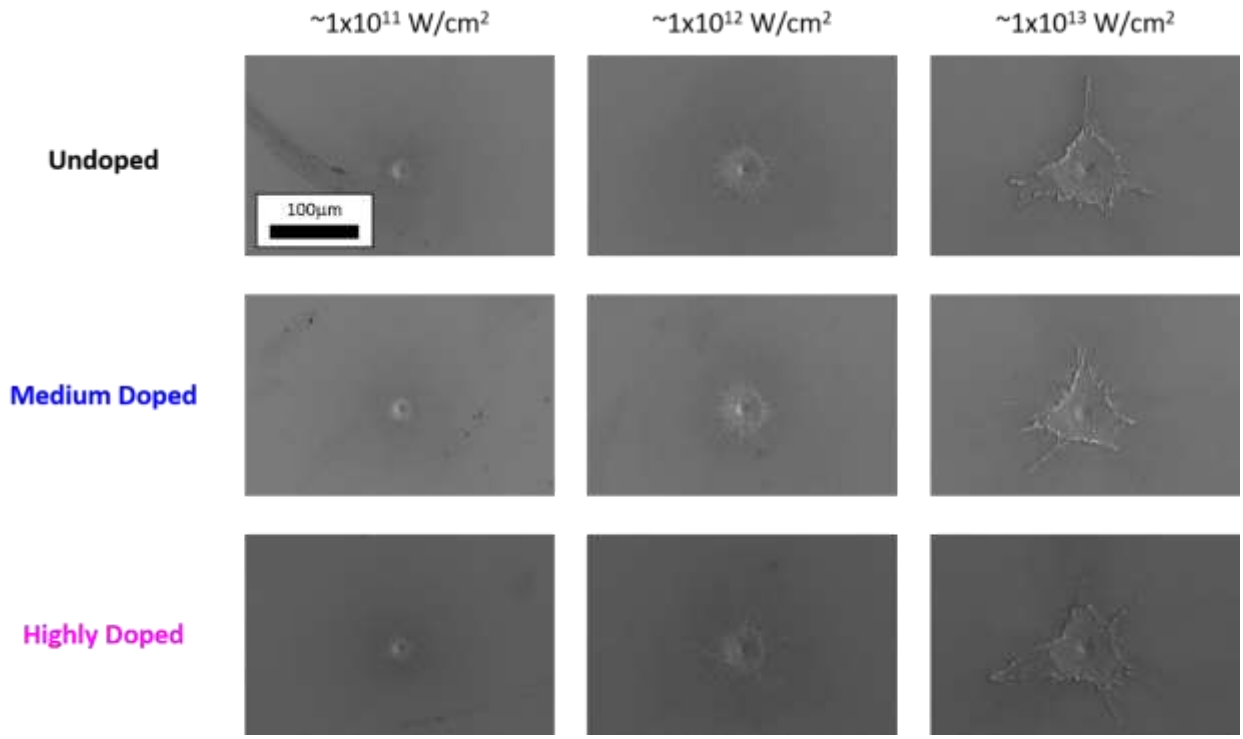

Figure 4.6: SEM Micrographs of Silicon Damage, Vertical Axis is Doping Concentration, Horizontal Axis is Peak Laser Intensity

It is important to note that once the triangular ablation characteristics occur, near the $5x10^{12}$ W/cm^2 intensities, that the diameters of the ablation must be broken into two forms. One is the inner diameter (ID) where at least two points are coincident with the interior of ablated material, and the other is the outer diameter (OD) where at least two points intersect with the exterior of ablated material in the exterior triangular shape. These method for estimating the diameters of both the inner and outer with respect to the triangle were estimated using ImageJ and are clearly depicted in **Figure 4.7**.

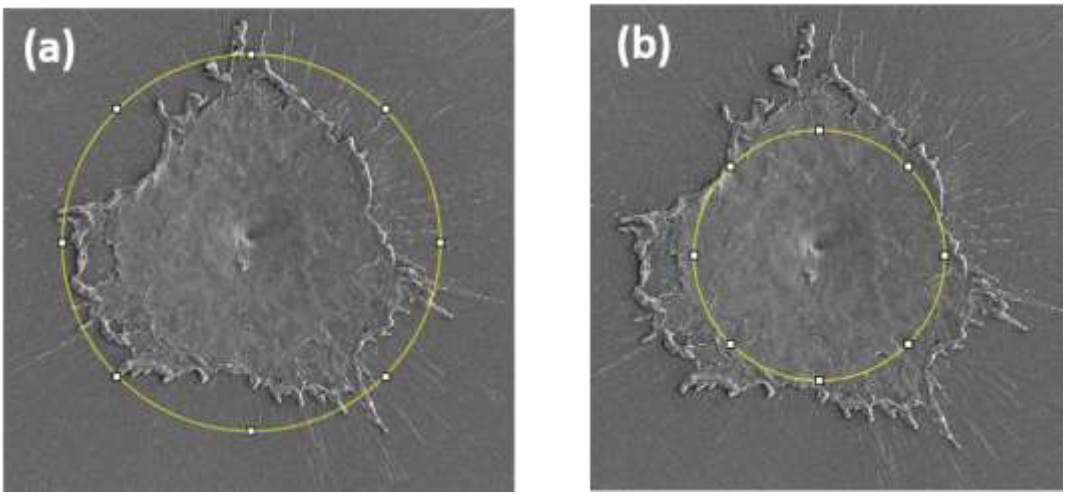

Figure 4.7: Silicon Damage at ~$8x10^{12}$ W/cm^2 with ImageJ Measurement Method Shown, (a) Outer Diameter, (b) Inner Diameter

Using the diameters, including the inner and outer diameters after the specified threshold, the damage as a function of intensity is plotted in **Figure 4.8** where the ID appears to be fairly consistent, and the OD slightly increasing with respect to intensity.

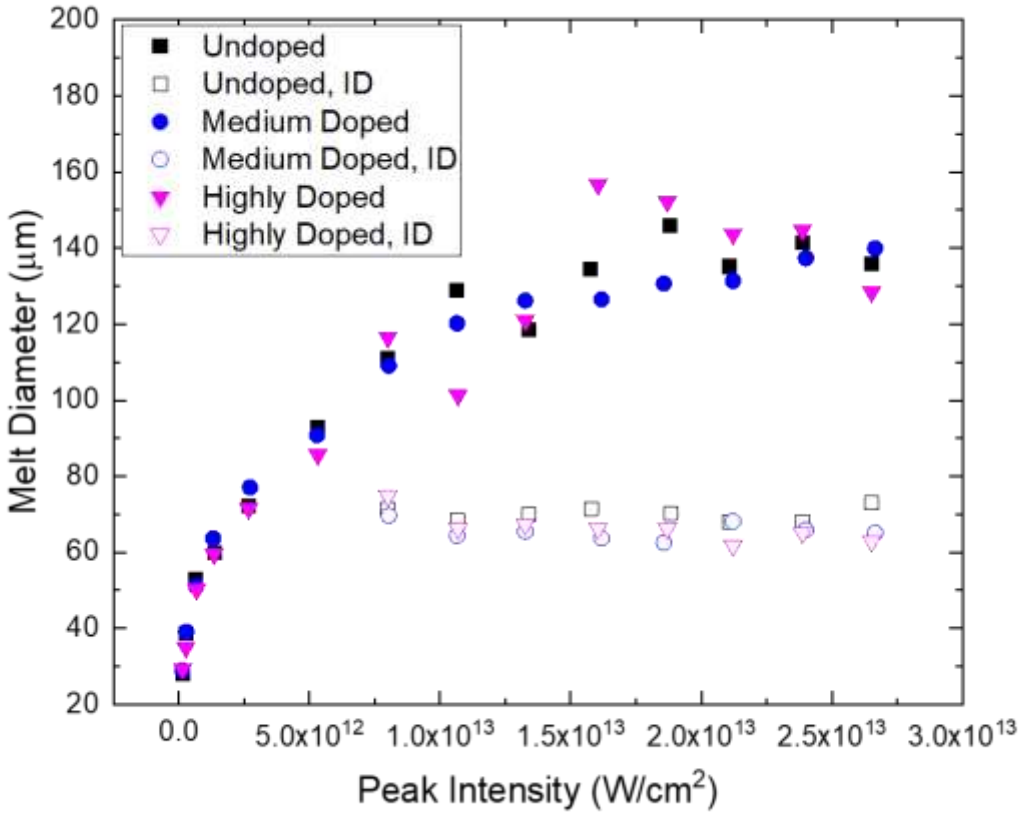

Figure 4.8: Silicon Melt Diameter vs. Peak Intensity, High Intensity Shots, Open Symbols Represent Inner Diameter Measurements

Investigating further, and in comparison to what other work has been done in Werner et al. [7], the melt diameter was plotted against intensity with the diameter squared in **Figure 4.9** and with the diameter cubed in **Figure 4.10**.

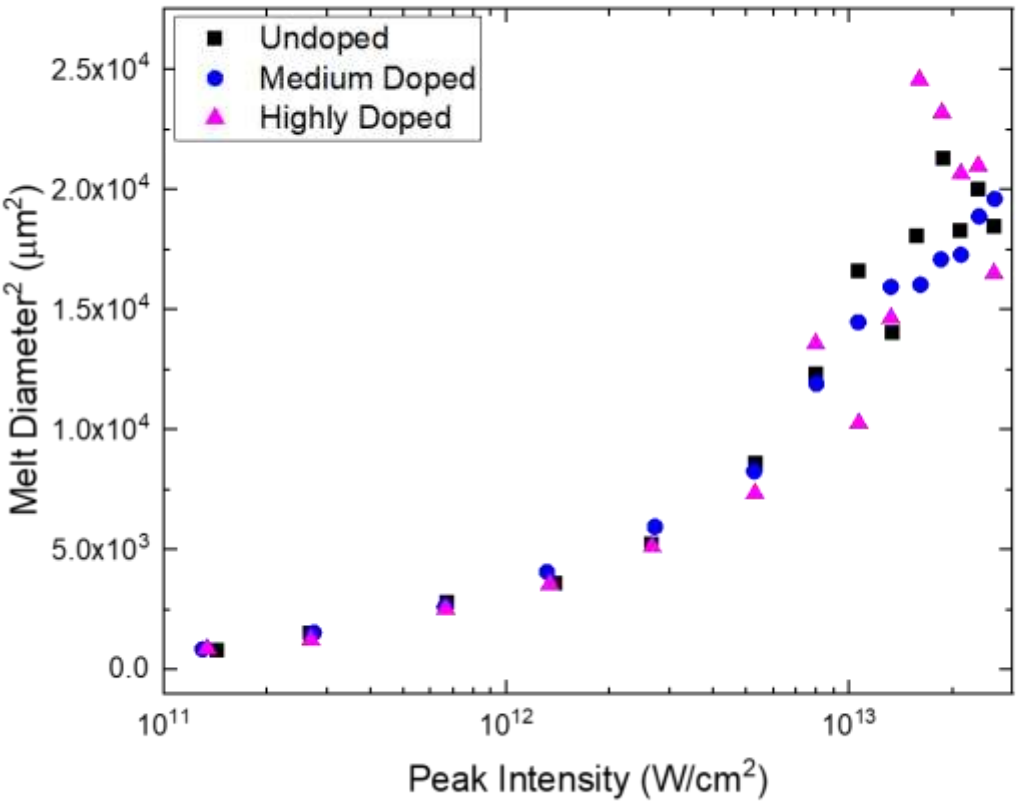

Figure 4.9: Melt Diameter^2 vs. Peak Intensity, Log Scale, for Silicon Outer Diameter Damage

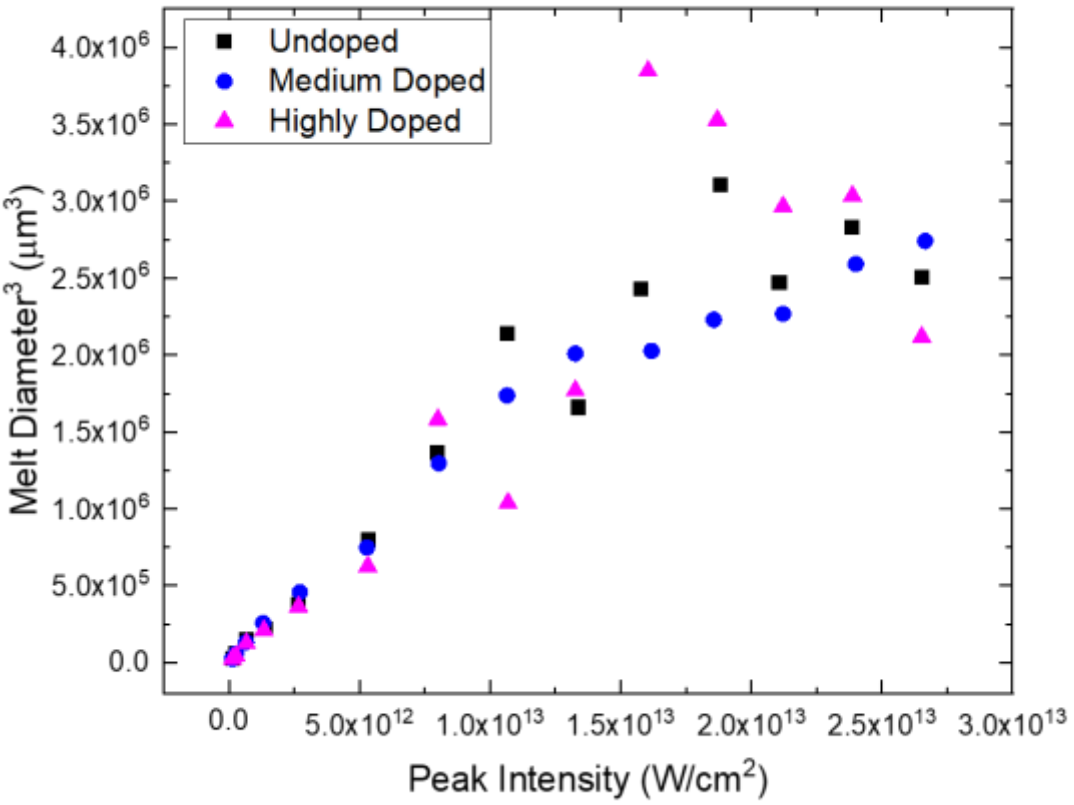

Figure 4.10: Melt Diameter^3 vs. Peak Intensity of Silicon Outer Diameter Damage

It is clear to see that melt diameter squared (**Figure 4.9**) a low intensities is fairly linear, while at higher intensities (**Figure 4.10**) it is more linear with respect to melt diameter cubed. This suggests that there is mechanism shift in which the damage moves from pure melting, to a form of ordered damage at higher intensities. Werner et al. shows good agreement with damage diameter squared with respect to fluence [7]. Further studies are required to fully characterize this laser induced damage behavior, and fully quantify how much of the material is damaged vs. ablated in the process of irradiation.

4.6. Conclusions and Future Work

Surprisingly crystalline silicon of differing doping concentration exhibits damage primarily as melting at intensities up to 10^{13} W/cm^2. This is not fully characterized in the regimes studies in this work, but a discrepancy between less than $5x10^{12}$ W/cm^2 and great than the value is noted. The characteristic melt diameter behavior appears to plateau with respect to the inner diameter, but appears to grow with respect to the outer diameter.

Additional investigation into the damage mechanisms of silicon at ~10^{13} W/cm^2 intensities is necessary to fully quantify and understand the behavior of silicon over $5x10^{12}$ W/cm^2 intensities. Follow on work would need to study the impact of moving the focus of the beam into the material, also known as a z-scan, and fully characterizing the damage with post irradiation techniques such as XRD and Raman spectroscopy. Studying these two together will improve the understanding of the damage of silicon as a function of laser intensity.

4.7. References

[1] Schwarz-Selinger, T., Cahill, D.G., Chen, S.C., Moon, S.J. and Grigoropoulos, C.P. "Micron-scale modifications of Si surface morphology by pulsed-laser texturing." *Physical Review B* 64.15 (2001): 155323.

[2] Sproul, A. B., and M. A. Green. "Improved value for the silicon intrinsic carrier concentration from 275 to 375 K." *Journal of applied physics* 70.2 (1991): 846-854.

[3] Yoo, J. H., Jeong, S. H., Greif, R., & Russo, R. E. "Explosive change in crater properties during high power nanosecond laser ablation of silicon." *Journal of Applied physics* 88.3 (2000): 1638-1649.

[4] Leyder, S., Grojo, D., Delaporte, P., Marine, W., Sentis, M., & Utéza, O. "Non-linear absorption of focused femtosecond laser pulses at 1.3 μm inside silicon: Independence on doping concentration." *Applied Surface Science* 278 (2013): 13-18.

[5] Rahman, T.U., Khan, R.A.A., Qayyum, H., Amin, U., Ullah, S., Dogar, A.H., Mahmood, A., Rafique, M. and Qayyum, A. "Characterization of microcraters fabricated on the silicon surface

by single and multi-pulse laser ablation at various laser intensities." *Nuclear Instruments and Methods in Physics Research Section B: Beam Interactions with Materials and Atoms* 487 (2021): 45-51.

[6] Hanh, E. N., Bailly-Grandvaux, M., Cordova, T., Turner, R. E., Joshi, T.R., Spielman, R.B., Wicks, J. K., Garay, J. E., Beg, F. N. "Laser pulse-length dependent ablation and shock generation in silicon at $4x10^{14}$ W/cm^2 intensities." *Physical Review Research* – in Review

[7] Werner, K., Gruzdev, V., Talisa, N., Kafka, K., Austin, D., Liebig, C.M. and Chowdhury, E. "Single-shot multi-stage damage and ablation of silicon by femtosecond mid-infrared laser pulses." *Scientific reports* 9.1 (2019): 19993.

4.5. Acknowledgements

The project or effort depicted was or is sponsored by the Department of the Defense, Defense Threat Reduction Agency under award HDTRA1-20-2-0001. The content of the information does not necessarily reflect the position or the policy of the federal government, and no official endorsement should be inferred.

Chapter 4, in part is currently being prepared for submission for publication of the material. Gabriel R. Castillo, Colin G. Meisner, and Javier E. Garay are co-authors for this work. The dissertation author was the primary researcher and author of this material.

CHAPTER 5. HIGH-ENERGY LASER POLICIES

5.1. Introduction to chapter 5

The following brief chapter highlights additional work conducted as part of a fellowship awarded by the School of Global Policy and Strategy at UCSD. This fellowship focused on understanding downstream policy implications of scientific research conducted at the university, as part of dissertation research.

5.2. Motivations

The drive toward higher powered lasers is not something only researchers and corporate entities need to concern themselves with. As laser power has increased, and continues to increase, the packaging of these lasers has continually decreased. This has created a situation where more powerful lasers more accessible to the average consumer than ever before. This not only poses a safety risk to the end user of the laser, but also the regulation and identification of lasers was set based solely on eye safety, and not on personal or property safety. In conducting this dissertation research there was a unique opportunity to investigate potential ways to improve these challenges and educate policy makers on the changes necessary to prevent harm to others, with a focus on portability concerns of lasers.

5.3. Findings and Recommendations

There has been some discussion over the years with respect to the laser classification system used both domestically and internationally. Jamie King, the Laser Safety Officer (LSO)

of Lawrence Livermore National Lab (LLNL), posed the question of a new class of laser in 2013 to account for the dangers of new laser systems [1]. This question was driven by the increased chance of instantaneous harm from higher powered lasers, and the proposed Class 5 laser would be different than the Current Class 4 laser in that Class 5 lasers pose immediate risk of harm or even death [1]. This change was not implemented by any of the international standards over the last decade, but the LSO again shared concerns with current Class 4 laser safety policies [2]. In this work, it was highlighted that across the Class 4 system, the only differentiation between a lower powered laser, and the most dangerous lasers available, was the laser safety sign used on doors and equipment, which could read "caution", or "warning", or "danger" based on the output power of the laser [2]. Despite all of the laser safety training end users go through prior to authorization of Class 4 lasers, these signs can easily be overlooked or misinterpreted because they only have a word different.

An initial dive into local laws and regulations with respect to laser safety, and use of lasers as a weapon uncovered no specific guidance. Looking a level above to California State guidance, only two penal codes are listed that discuss the use of lasers to cause harm. Note this investigation specifically omitted medical laser regulation since that is managed through the Federal Drug Administration (FDA). California State Penal Code § 247.5 is related the use of a laser in a threatening manner, such that a person feels as though they will be harmed [3]. This would include a laser sight on a rifle or pistol, and does not consider the laser as the source of the harm. California State Penal Code § 417.25 is related to the pointing of a laser at an aircraft, also known as dazzling [4]. Together, these codes do not cover much in terms of the handling, use and misuse of lasers, nor what happens if a person uses a laser deliberately to harm a person or

property. As portability of these higher powered lasers becomes common, new rules and regulations must address this gap in policy.

Following on the work proposed by Jamie King, not only is there a need for a better delineation between warning and danger with respect to Class 4 lasers, but a new subcategories of Class 3 and Class 4 lasers should be considered. Class 3P and Class 4P are suggested to be added to the current international standards for portable lasers that pose risks to harm people and property. Portable in this context is small enough to be handled by a single person, in a way that could quickly cause harm (i.e. laser pointer, flash light, etc.). Class 3P is for lasers that pose a risk to eye safety, and can ignite material if focused or allowed to deposit energy for a significant amount of time. Class 4P is for lasers that pose an immediate risk to danger to a person or property, including but not limited to instantaneous burning of skin, clothes, or damage of a structure. The portable subcategory would significantly improve the way newer small packaged, but high powered lasers are viewed in research, and assist in education the general public on the hazards associated with higher powered lasers.

If implemented, significant energy will be required to update safety documentation, training, and shift the mindset of existing laser operators to understand the differences in risks associated with the new subcategories and classes of lasers. Additionally, improved regulation of the updated labels found on lasers would need to be implemented to ensure that a Class 4P laser is not marked as a Class 3P laser. This may require new or updated testing standards to inspect and qualify products bought and sold across the globe.

5.4. References

[1] King, Jamie J. "Is it time for a class 5 laser?" *International Laser Safety Conference*. Vol. 2013. No. 1. Laser Institute of America, 2013.

[2] King, Jamie J. "Beyond class 4, laser safety controls for very high-power lasers." *International Laser Safety Conference*. Vol. 2019. No. 1. Laser Institute of America, 2019.

[3] Assault and Battery, California State Penal Code § 247.5.

[4] Of Crimes Against the Public Peace, California State Penal Code § 417.25.

5.5. Acknowledgements

Funding of this work by the School of Global Policy and Strategy (GPS) at UC San Diego as part of the Science Policy Fellowship is most gratefully acknowledged.